Approaches to Structure and Dynamics of Biological Systems by Electron-Paramagnetic-Resonance Spectroscopy

PROEFSCHRIFT

ter verkrijging van
de graad van Doctor aan de Universiteit Leiden,
op gezag van de Rector Magnificus Prof. mr. P. F. van Heijden,
volgens besluit van het College voor Promoties
te verdedigen op woensdag 28 oktober 2009
klokke 13:45 uur

door

Francesco Scarpelli
geboren te Cosenza, Italië
in 1976

Promotiecommissie:

Promoter: Prof. dr. Edgar Groenen
Copromoter: Dr. Martina Huber
Overige leden: Prof. dr. Antoinette Killian (Utrecht University)
Prof. dr. Jan van Ruitenbeek
Prof. dr. Jan Schmidt
Prof. dr. Thomas Schmidt
Dr. Marcellus Ubbink

The present work was supported with financial aid by The Netherlands Organization for Scientific Research (NWO), Department Chemical Sciences (CW).

Casimir PhD Series, Delft-Leiden, 2009-06
ISBN/EAN: 978-90-8593-054-9

ai miei genitori, a mio fratello
to my parents, to my brother

Table of Contents

Chapter 1. Introduction

The study of the structure and dynamics of proteins and enzymes is crucial in the understanding of the function of such biological systems. Structure first refers to the geometrical structure, as a result of backbone folding and local arrangement of amino-acid side chains. Secondly, structure refers to electron structure, in particular at the active sites of proteins and enzymes where the transformations take place. Dynamics refers to structural changes as a response to changes in the environment of the system and to relative rearrangement of different parts of its molecules, for example during complex formation and substrate binding.

Electron paramagnetic resonance (EPR), the technique central to all the experiments reported in this thesis, is well suited to study protein structure and dynamics. By its nature, the EPR signal represents the fingerprint of the electronic wave function of a paramagnetic site. Moreover, the interactions of the electron spin with nearby nuclear spins may show up and provide information about the delocalized nature of the electronic wave function. In case more electron spins are present, their dipolar interaction contains information about the distance and the mutual orientation of the electron spins. In order to obtain this structural and dynamic knowledge from EPR experiments, both continuous-wave (cw) and pulsed microwave excitation have been applied, and samples as diverse as single crystals, solution and membranes were studied.

The EPR spectroscopy detects unpaired electrons. In proteins, these may be present naturally as radicals or paramagnetic transition metal ions. Proteins that do not have unpaired electrons can also be studied, but they require extrinsic paramagnetic probes called spin labels. Spin labels are nitroxide derivatives with a stable unpaired electron and a functional group that allows its site-specific attachment to a protein. The most popular amino-acid residues used to attach spin labels are cysteine residues, which, if necessary, can be introduced into the protein structure using molecular biology techniques. In the research described in this thesis both transition metal ions, such as Cu(II) and Fe(III), and nitroxide spin labels have been used.

The work described in this thesis comprised both methodological developments and the application of EPR to specific research questions.

In the next section, I first briefly describe the basic theory of EPR, and subsequently shortly introduce the research reported in Chapters 2 to 5.

1.1 Background of EPR

In EPR experiments, the electron (and nuclear) spins interact with an external magnetic field (static field, oscillatory radiofrequency or microwave field) and with other spins, i.e., other magnetic dipoles within the sample. The interactions of spins with their environment concern the interactions of magnetic dipoles with each other and with external magnetic fields. In magnetic resonance, the external magnetic field defines a unique direction in the laboratory frame. Generally the interactions of spins are anisotropic and they depend on the orientation of the molecule with respect to the laboratory frame (external magnetic field). The EPR spectra of systems in the solid state, such as crystals (ordered arrays of molecules) and frozen solutions (disordered arrays of molecules), reveal anisotropic interactions

.

1.1.1 Spin Hamiltonian

The interaction between the electron spin (S) and the external magnetic field is called electron Zeeman (H_{EZ}) interaction and the interaction between the electron spin and the nuclear spin (I) is called hyperfine interaction (H_{HF}). The spin Hamiltonian for an S=1/2 system can be written as

$$H = H_{EZ} + H_{HF} = \beta_e \vec{B}_0 \vec{\vec{g}} \vec{S} + \vec{S} \vec{\vec{A}} \vec{I} \quad . \qquad (1)$$

Here β_e is the electron Bohr magneton, $\vec{B}_0$ is the external magnetic field, $\vec{\vec{g}}$ is the g-tensor and $\vec{\vec{A}}$ is the hyperfine tensor. The hyperfine term can be written as the sum of the Fermi contact interaction and the dipole-dipole coupling between the electron spin and the nuclear spin [1]. In the following equation, the first term describes the Fermi contact interaction and the second one the dipole-dipole coupling between the electron spin and the nuclear spin.

$$H_{HF} = a_{iso}\vec{S}\vec{I} + \frac{\mu_0}{4\pi} g\beta_e g_n \beta_n \left[\frac{3(\vec{S}\vec{r})(\vec{I}\vec{r})}{r^5} - \frac{\vec{S}\vec{I}}{r^3} \right] \quad , \tag{2}$$

where a_{iso} is the isotropic hyperfine constant, μ_0 is the permeability of vacuum, g and g_n are respectively the electron and the nuclear g factors, β_n is the nuclear Bohr magneton and $\vec{r}$ is the vector that joins the electron spin and the nuclear spin and r its magnitude.

If the system has two unpaired electrons, the dipole-dipole coupling between the two electron spins (S_1 and S_2) has to be taken into account. It is similar to the electron-nuclear-dipole interaction in Eq. 2, and for the magnetic field parallel to z-axis can be written as

$$H_{DD} = \frac{\mu_0}{4\pi} \frac{g_1 g_2 \beta_e^2}{r_{12}^3} \left(1 - 3\cos^2\theta\right) \left(S_{1z}S_{2z} - \frac{1}{2} S_{1x}S_{2x} - \frac{1}{2} S_{1y}S_{2y} \right), \tag{3}$$

where g_1 and g_2 are the g factors of the two electrons, r_{12} is the magnitude of the vector that joins the two electrons and θ is the angle between the static magnetic field and the vector that joins the two electrons (Fig. 1).

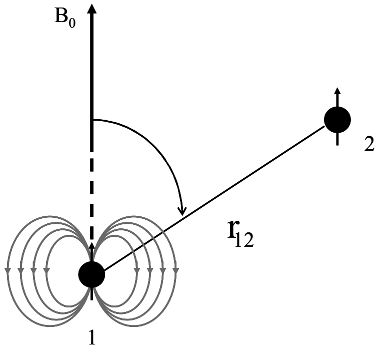

Fig. 1: Schematic representation of the electron-electron dipolar interaction. The two black circles represent the electrons.

1.2 The anisotropy of the g-tensor of a metal center in a protein: single crystal EPR

The Zeeman interaction in Eq. 1 describes the interaction between the spin of an unpaired electron and the external magnetic field. For such an electron in a transition-metal ion, g is anisotropic and is described by the tensor $\vec{\vec{g}}$. The principal axes of g (x, y and z) have a well-defined orientation with respect to the ligands that are bound to the transition-metal ion (Fig. 2). The directions of the principal axes contain information about the electronic structure of the center and they can be determined by single crystal EPR [2].

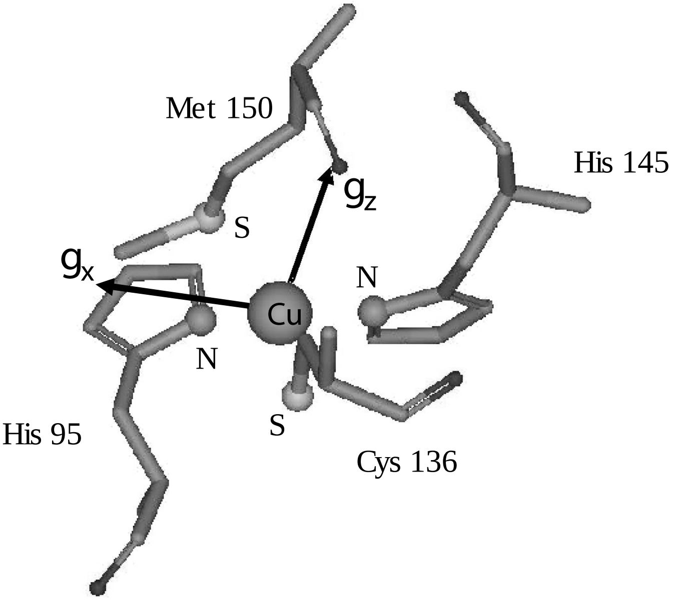

Fig. 2: The directions of the x and z principal axes of the g-tensor of the type-1 copper site of an azurin protein. The histidines (His) and the cysteine (Cys) ligands are approximately in one plane. The g_z axis is approximately perpendicular to the N-Cu-N plane [2].

The Fig. 3a shows the orientation of the magnetic field $\vec{B}_0$ in the g-tensor principal axes system. The field of resonance changes as a function of the orientation of $\vec{B}_0$ and if the field is oriented along one of the principal directions of g the resonance position is characterized by the corresponding g value. This is illustrated in Fig. 3b, where the resonance fields correspond to g_z and g_x for fields parallel to z and x. Measuring the resonance field for a single crystal as a function of the orientation of the magnetic field with respect to the crystal, the full tensor can be obtained.

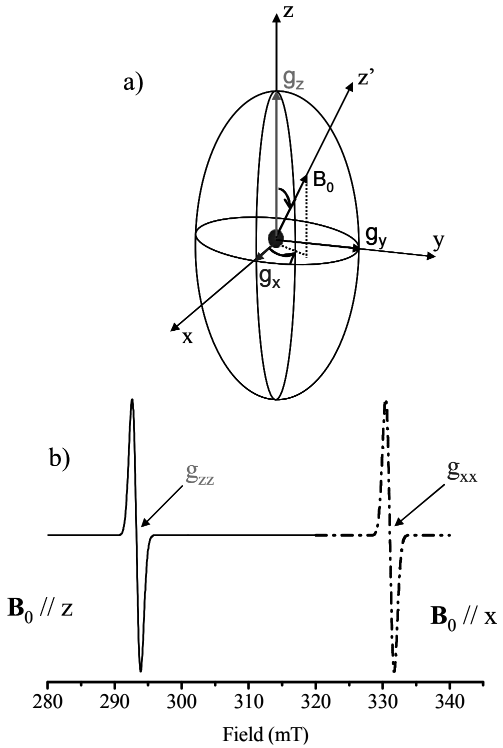

Fig. 3: A paramagnetic center and the principal axes of its g-tensor. (a) The molecular frame (xyz) of the paramagnetic center (dot) is defined by the direction of the principal axes of the g-tensor. Also shown is the direction of the z axis of the laboratory frame (z'). The **B_0** is shown parallel to z'. (b) The EPR spectrum for **B_0** parallel to z and parallel to x.

The research in Chapter 2 concerns the determination of $\vec{g}$ of the type-2 copper site (Cu(II), S=1/2) in the nitrite reductase protein. These experiments have been performed on a single crystal of the protein by EPR at 95 GHz. The analysis is complicated because of the presence of several paramagnetic sites in the crystal, which results in a multitude of overlapping bands [2]. The determination of the directions of the principal axes is described and the results are discussed in terms of the electronic structure of the copper center.

1.3 Averaging of the anisotropic spin interactions: spin-label mobility by EPR

While the anisotropy of the magnetic interaction yields information on the electronic structure, dynamics can be obtained from incomplete averaging of anisotropic interactions. Dynamics in proteins is often studied using spin labels. These are stable nitroxide radicals in which the unpaired electron is delocalized over the nitrogen and the oxygen (Fig. 4).

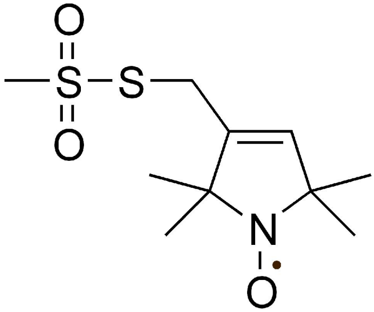

Fig. 4: Chemical structure of a nitroxide spin-label. The black dot represents the unpaired electron.

An isotropic EPR spectrum of such a spin label is shown in Fig. 5a. The three lines of this spectrum result from the hyperfine interaction between the electron spin $S = \frac{1}{2}$ and the nitrogen nuclear spin $I = 1$. This EPR spectrum one observes for a spin label freely tumbling in solution; the fast rotation of the molecules averages the anisotropy of the interaction between $\vec{S}$ and $\vec{B}_0$ and between $\vec{S}$ and $\vec{I}$, resulting in an isotropic spectrum. In this case, the separation between the EPR lines is a_{iso}, which comes from the Fermi contact term in the hyperfine Hamiltonian (Eq. 2).

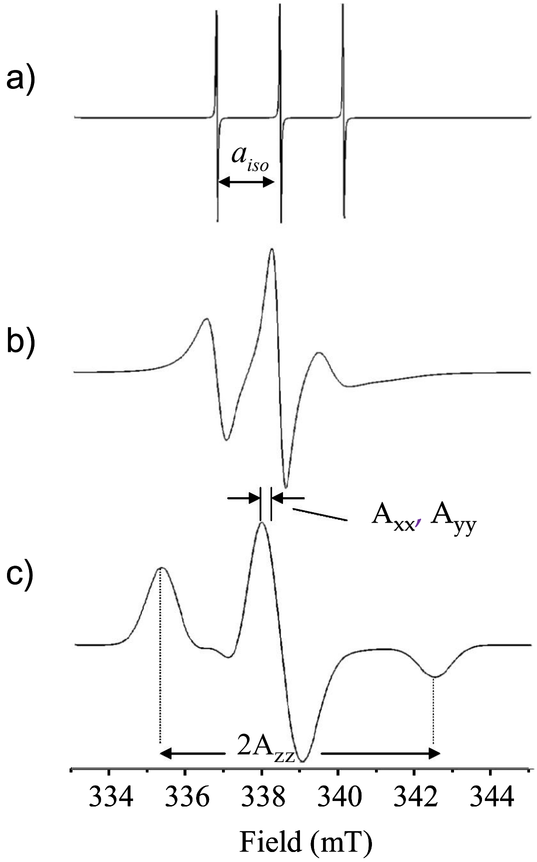

Fig. 5: Effect of the rotational-correlation time (τ_c) on the line shape of EPR spectra of a nitroxide spin-label. (a) The simulated EPR spectrum of a nitroxide spin label with τ_c = 10 ps (liquid solution). (b) The simulated EPR spectrum of a nitroxide spin label with τ_c = 3 ns (intermediate case). (c) The simulated EPR spectrum of an immobilized nitroxide spin label (frozen solution).

In Fig. 5c, the EPR spectrum of a spin label in frozen solution is shown. Here, the molecules are randomly oriented with respect to $\vec{B}_0$ and immobilized. The so-called powder spectrum results from the summation over all the possible orientations. The lines are shifted and broadened relative to the isotropic spectrum because of the anisotropic Zeeman and hyperfine interactions. Fig. 5b illustrates the EPR spectrum of a spin label in an intermediate situation, between the liquid and the frozen state. In this case, the rotation of the molecules is not fast enough to fully average the anisotropy of the spin interactions and the EPR spectrum shows a broadening with respect to the spectrum in Fig. 5a. From the amount of broadening, the rotation-correlation time can be obtained. Therefore, the line shape analysis of such EPR spectra reveals information about the mobility of the spin label and about the local dynamics and possibly local structure elements of the part of the protein to which the spin label is attached [3].

Chapter 3 deals with the mobility of spin labels attached to ten surface positions of a cytochrome c peroxidase in solution. Results are being discussed in the context of the secondary structure of the protein and of the rotation-correlation time of the spin labels.

1.4 Electron dipole-dipole interaction: distance measurements for structure determination

The EPR spectroscopy can be used to measure distances which serve to determine the structure of biological systems. It makes use of the dipolar interaction between spins (Eq. 3 and Fig. 1) to measure distances in the range between 0.8 nm and 10 nm [4] (Fig. 6). Continuous wave (cw) EPR is well suited for the distance range between 0.8 nm and 2.5 nm [4] (Fig. 6). Larger distances, up to 10 nm (Fig. 6), have been measured by pulse techniques, which separate the dipole-dipole interaction of the electron spins from other interactions [5].

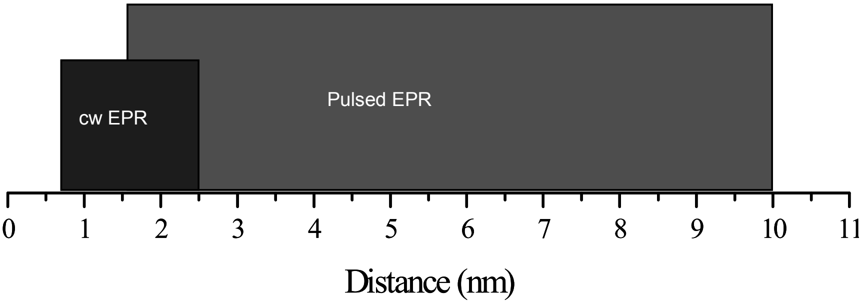

Fig. 6: Distance range covered by EPR spectroscopy. From 0.8 nm and 2.5 nm, the range covered by cw EPR. From 1.8 nm to 10 nm, the range covered by pulsed EPR.

1.4.1 Structure of a disordered system by cw EPR

The research described in Chapter 4 concerns the study of aggregation of peptides in membranes (lipid bilayers). Such systems are intrinsically disordered, and structural information can be obtained from cw EPR. If spin-labeled peptides aggregate in the membrane, the short distance between the spin labels (Fig. 7a) causes a broadening of the EPR spectra, which serves as an observable for aggregation. In Fig. 7c, the spectral effect of aggregation (broadening Δ) is shown. The broadening Δ is derived from the difference between a spectrum where the electron spins of the spin-labeled peptides interact (Fig. 7a) and the reference spectrum where the electron spins of the spin-labeled peptides are too far from each other to interact (Fig. 7b).

Whether aggregation occurs depends on the balance between peptide-peptide, lipid-peptide or lipid-lipid interactions. Therefore, it is interesting to study the aggregation of peptides at different conditions and phases of the lipids. Although broadening is an indication of aggregation, it is not sufficient in itself to prove aggregation and to describe the size and the geometry of the aggregate. The broadening for a pair of interacting electron spins is well established [6], but when spin-labeled peptides aggregate many the electron spins interact with each other and the broadening will be the result of their mutual interactions.

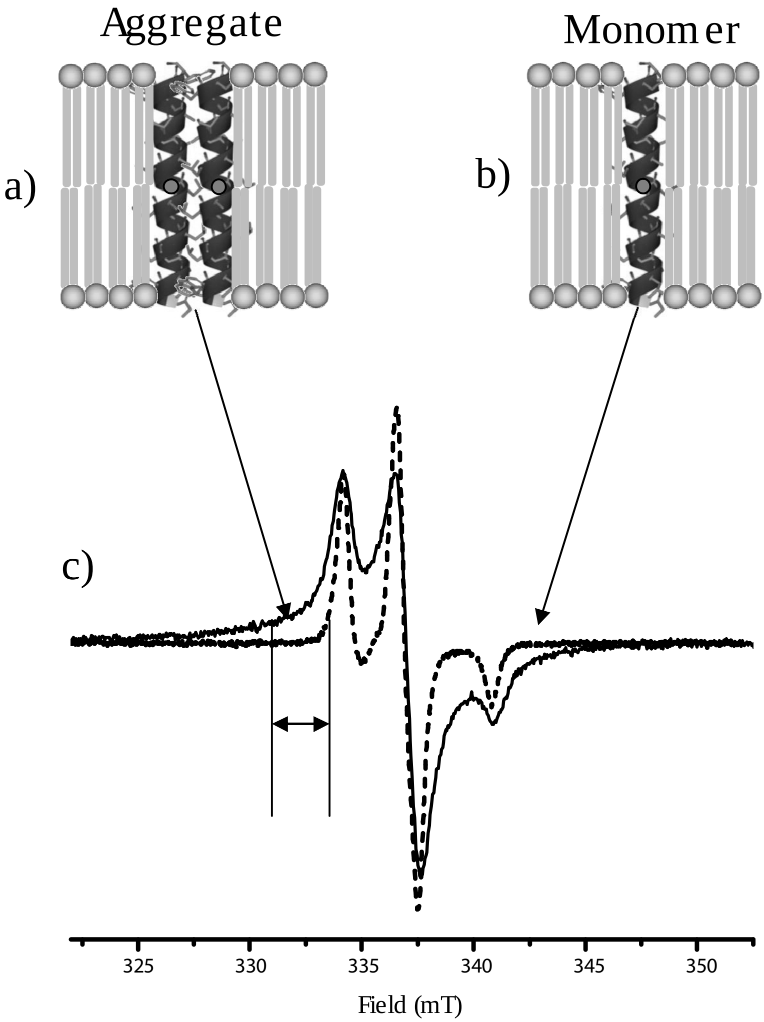

Fig. 7: Aggregation of peptides in membranes. (a) Side view of a peptide aggregate in a membrane. (b) Side view of a monomer of a peptide in a membrane. The gray circles in picture a) and b) indicate the position of the spin labels in the peptides. (c) The resulting EPR spectra of the aggregate (solid line) and of the monomeric spin-labeled peptides (dotted line). The Δ symbol indicates the broadening.

For a linear trimer aggregate (see Fig. 8b), for example, the spin label of the first peptide will interact not only with the spin label at a distance R (neighbour peptide), but it will interact also with the spin label at a distance of 2 R (third peptide). At the same time, the spin label of the second peptide will interact with the spin labels of both neighbouring peptides at a distance R. Therefore, a model that relates the broadening of the EPR spectra to the arrangement of the peptides in the lipids has been developed.

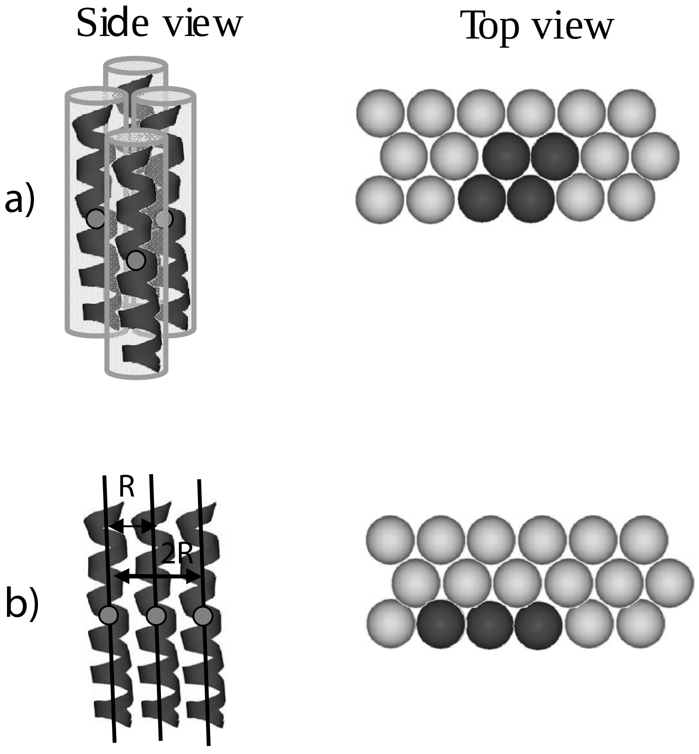

Fig. 8: Cluster and linear aggregates of peptides in membranes. (a) Side and top view of a cluster aggregate of spin-labeled peptides. (b) Side and top view of a linear aggregate of spin-labeled peptides. The gray circles in the side-view pictures indicate the position of the spin labels in the peptides. R indicates the distance between two neighbor peptides.

This model not only characterizes the dipolar broadening, but it relates the broadening to the size and the geometry of the aggregates. Comparing these under different lipid conditions reveals which of these conditions promotes the peptide-peptide interaction. In Fig. 8, examples of aggregates with different geometry and size are shown.

1.4.2 Distance measurement by pulsed EPR

Several pulsed EPR methods, such as the 2+1 sequence, the double electron-electron resonance (DEER) and the double-quantum coherence (DQC) [7-9], have been used in the last decade to measure distances and to determine the structure of chemical and biological systems by detecting the dipolar interaction between electron spins. These techniques are optimized for systems with low spectral anisotropy, such as nitroxide spin labels and organic radicals, and require that the pulses excite a large part of the spectrum. Transition-metal ions have a larger spectral width (anisotropy) than nitroxides and complete spectral excitation is not possible. In Fig. 9, the EPR spectra of a nitroxide and a transition-metal ion, an iron center, are superimposed. Whereas the nitroxide spectrum has a width of 10 mT, the spectrum of the metal center is 300 mT wide. The common pulsed methods have an excitation bandwidth of a few mT, e.g. a pulse length of 24 ns results in a bandwidth of 1.5 mT. For a system that involves a transition-metal ion, the resulting fractional excitation of the spectrum either severely limits the sensitivity or makes the application of these methods impossible. Therefore, to measure the distance between a nitroxide spin label and a transition-metal ion, different methods are needed. Such a method is the relaxation induced dipolar modulation (RIDME). Fig. 10b illustrates the three-pulse RIDME sequence. During the evolution time T, spontaneous flips of the spins of the transition-metal ion (B-spins), due to their longitudinal relaxation, occur. This causes modulation of the echo intensity of the spins of the nitroxide (A-spins), resulting in the dipolar trace (Fig. 10b). Therefore, there is no need to flip the B-spin by a pump pulse, avoiding the problem of the limited excitation bandwidth. Even though the three-pulse RIDME experiment is not affected by the limitation of the bandwidth, it suffers from a dead-time problem. For systems with large spectral anisotropy, most of the information about the dipolar interaction lays in the initial part of the recorded dipolar-modulation time trace.

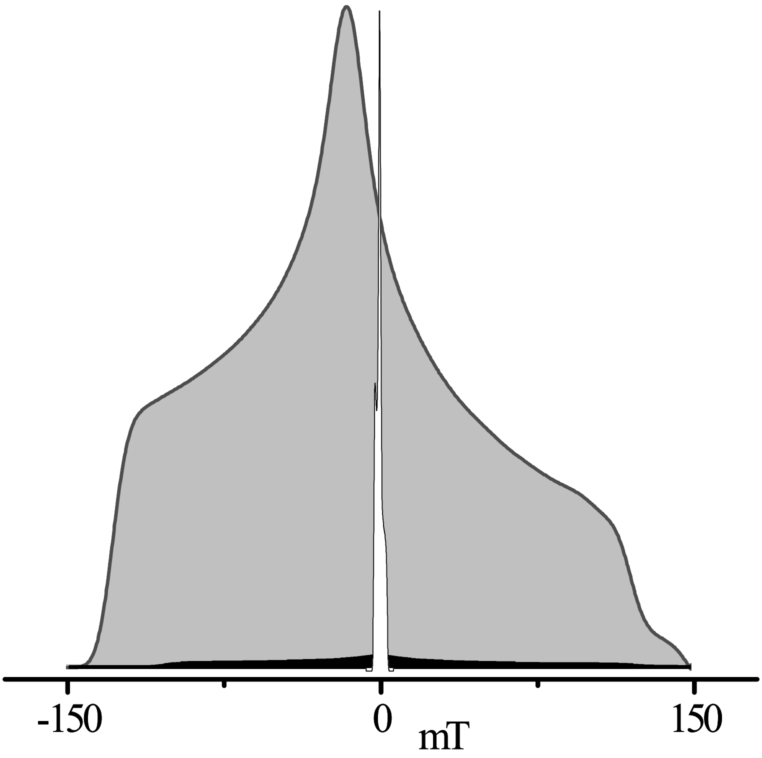

Fig. 9: The comparison between the EPR spectral width of a nitroxide spin-label and an iron(III) center (S=1/2). White-filled: the EPR spectrum (absorption mode) of the nitroxide. Black-filled: the EPR spectrum (absorption mode) of the iron center. Gray-filled: intensity of the black-filled spectrum multiplied by 30.

To detect the initial part of the trace, the inter-pulse separation τ has to be very short (see sequence in Fig. 10b). The problem is that τ can not be zero because the first and the second pulse should not overlap. Therefore, to avoid the dead-time problem, a new 5-pulse RIDME sequence has been developed.

In Chapter 5, this new sequence is introduced and its application to determine the distance between the low-spin iron(III) center and a nitroxide spin label (Fig. 10a) in spin-labeled cytochrome *f* is described.

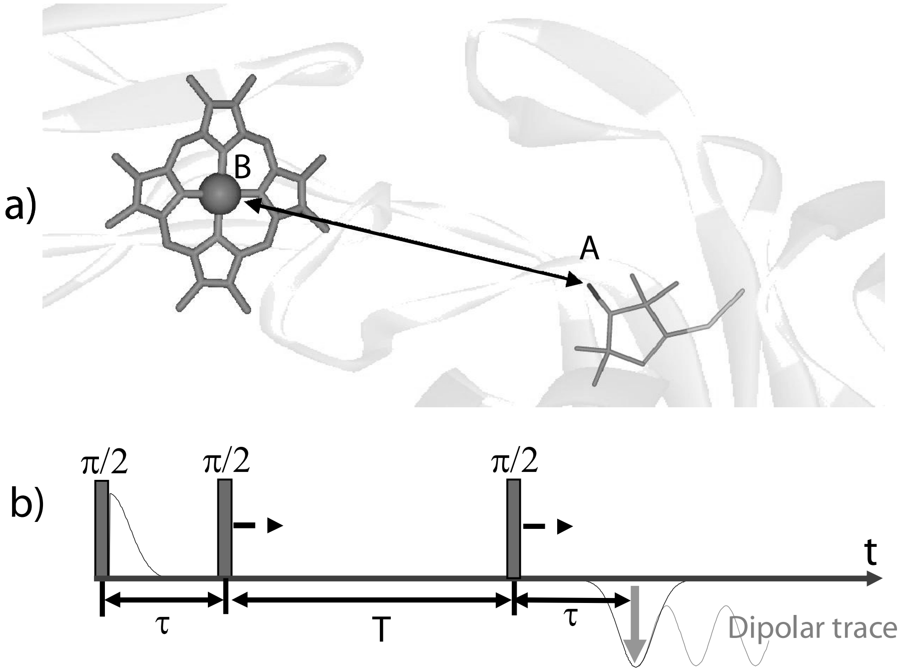

Fig. 10: (a) A schematic representation of iron center and of a nitroxide spin-label in a cytochrome *f* protein. The electron spins of the iron and of the nitroxide are indicated respectively by B and A. (b) The three-pulse RIDME sequence.

Reference list

1. Atherton, N. M. *Principles of Electron Spin Resonance;* Hellis Horwood Limited: Chichester, 1993.
2. Coremans, J. W. A.; Poluektov, O. G.; Groenen, E. J. J.; Canters, G. W.; Nar, H.; Messerschmidt, A. *Journal of the American Chemical Society* **1994,** *116* (7), 3097-3101.
3. Steinhoff, H. J.; Hubbell, W. L. *Biophysical Journal* **1996,** *71* (4), 2201-2212.
4. Berliner, L. J.; Eaton, S. S.; Eaton, G. R. *Biological Magnetic Resonance: Distance measurement in biological systems by EPR;* Kluwer Academic, New York: 2000.
5. Schweiger, A.; Jeschke, G. *Principles of Pulse Electron Paramagnetic Resonance;* Oxford University Press: 2001.
6. Steinhoff, H. J. *Frontiers in Bioscience* **2002,** *7*, C97-C110.
7. Kurshev, V. V.; Raitsimring, A. M.; Tsvetkov, Y. D. *Journal of Magnetic Resonance* **1989,** *81* (3), 441-454.
8. Milov, A. D.; Ponomarev, A. B.; Tsvetkov, Y. D. *Chemical Physics Letters* **1984,** *110* (1), 67-72.
9. Saxena, S.; Freed, J. H. *Chemical Physics Letters* **1996,** *251* (1-2), 102-110.

Chapter 2. A single-crystal study at 95 GHz of the type-2 copper site of the M150E mutant of the nitrite reductase of *Alcaligens faecalis*

2.1 Introduction

Copper centers play an important role in proteins, where they act as electron-transfer or catalytically active sites. To deepen our knowledge concerning the activity and function of copper sites, information about their electronic structure is needed. Type-1 copper sites are involved in electron transfer and have been extensively studied. The correlation between variations in the metal coordination and the electronic structure of such sites has been elucidated [1-3]. High-field EPR studies on single crystals have provided detailed information on the type-1 sites of azurin [4] and nitrite reductase (NiR) [5]. As yet, less is known about the electronic structure of type-2 copper sites, in particular about those that catalyse biochemical transformations in enzymes.

The NiR protein is a 110 kDa homotrimer in which each monomer contains a type-1 (blue) copper site and a type-2 (non blue) copper site [6,7] that catalyses the reduction of nitrite to nitric oxide. In the catalytic cycle of the protein, the type-2 site (Fig. 1), in which the copper is ligated to three histidines (His100, His135, and His306) and a water molecule, binds nitrite at the expense of water. Subsequently, the nitrite is reduced to nitric oxide by an electron transferred from the type-1 copper site. Here we consider the type-2 copper site of NiR from *Alcaligenes faecalis* strain *S-6*.

Earlier EPR studies of the type-2 site of NiR concern the investigation of the hyperfine interaction of the histidine nitrogens [8,9] and the effect of substrate binding [8]. Here, the complete g-tensor is targeted, because the orientation of the principal axes of the g-tensor is a sensitive probe of the electronic structure [5,10].

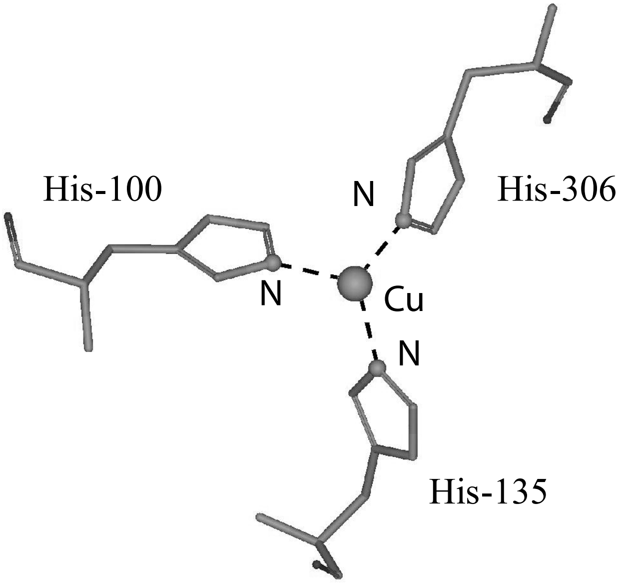

Fig. 1: The type 2 copper site of *A. faecalis* nitrite reductase [16].

The presence of two copper sites is essential for the function of the enzyme. It is a nuisance, however, for the EPR investigation because the superposition of two types of EPR signals is difficult to disentangle. Therefore, the M150E mutant, in which the methionine 150 is replaced by a glutamic acid, was used in which the type-1 copper site is EPR silent. It contains a copper that is in the reduced Cu(I) state [11-13].

In this chapter, we report the results of an electron-spin-echo (ESE) detected EPR study at 95 GHz of a single crystal of the NiR mutant M150E. The complete g-tensor has been determined. The unpaired electron is proposed to reside in a d_{xy} type orbital providing good overlap with the nitrogen lone-pair orbital of the histidines 135 and 306.

2.2 Materials and Methods

2.2.1 Sample preparation

The expression, purification and crystallization procedures for *A. faecalis* nitrite reductase have been described [13]. Crystallization of the M150E NiR was performed using a reservoir solution of 16.4 % polyethylene glycol 4000, 0.08 M sodium acetate at pH 4.2. Crystals were obtained using the hanging drop method at room temperature. Protein solutions were concentrated to about 10 mg/mL, and the buffer was exchanged with 10 mM MES, pH 6.0.

The crystals have typical dimensions of 0.1 x 0.1 x 0.1 mm^3.

2.2.2 EPR experiments

The EPR experiments were performed at a temperature of 2.1 K on a home-built electron-spin-echo (ESE) spectrometer at 95 GHz. The spectrometer was described previously [14], except for several upgrades. A NiR crystal was mounted in a capillary tube with an inner and outer diameter of 0.60 and 0.84 mm. The capillary tube was closed with sealing wax. The electron-spin echoes are generated by a two-pulse microwave sequence with a pulse length of 160 ns for both pulses, and a pulse separation of 320 ns. The EPR spectrum for each orientation of the magnetic field with respect to the crystal is recorded by monitoring the height of the echo while scanning the strength of the magnetic field. Because the spectrometer allows a rotation of the direction of the magnetic field in a plane that contains the capillary tube and a rotation of the capillary about its own axis, all orientations of the magnetic field with respect to the crystal could be selected without remounting the crystal.

2.2.3 Calculation of the field of resonance

The resonance position of the EPR lines depends on the orientation of the crystal with respect to the magnetic field ($\mathbf{B}_0$). For a particular orientation of $\mathbf{B}_0$ relative to the crystal, the field of resonance is calculated according to [10]

$$B_{res} = \frac{h\nu}{\mu_{\beta}\sqrt{\sum_{i}\left(g_{ii}\cos\Phi_{i}\right)^{2}}} \quad , \qquad (1)$$

where i = x, y, z, h is Planck's constant, ν is the microwave frequency, μ_β is the Bohr magneton and Φ_i is the angle between $\mathbf{B}_0$ and the principal *i* axis of a g-tensor.

2.2.4 Simulation

The first derivative of the 95 GHz ESE-detected EPR spectrum of the frozen solution of the M150E NiR protein has been simulated using *EasySpin 2.6.0* [15]. For the simulation the following tensors were used: G = [g_{zz} g_{yy} g_{xx}] = [2.312 2.0765 2.0489], which best fits the experimental spectrum, and A = [A_z A_y A_x] = [390 20 20] MHz, which was obtained from the EPR spectrum of the frozen solution measured at X-band.

2.3 Results

Fig. 2 shows 95 GHz ESE-detected EPR spectra of a single crystal of the nitrite reductase mutant M150E. The Fig. reveals the dependence of the spectra on the orientation of the external magnetic field, $\mathbf{B}_0$, with respect to the crystal. For each orientation the spectrum consists of several overlapping bands.

The single crystal of NiR belongs to the space group $P2_12_12_1$ with four asymmetric units per unit cell [16]. Each asymmetric unit contains one NiR molecule, a trimer that consists of three identical monomeric subunits connected by a three-fold (C_3) rotation axis. Four monomers, one in each asymmetric unit, are related by the crystallographic axes (a, b and c). These axes are two-fold (C_2) screw axes. Each monomer contains one type-2 copper site and one type-1 copper site, the latter being EPR silent for the NiR mutant M150E. With 12 type-2 copper sites in the unit cell, the EPR spectrum comprises of 12 resonances for an arbitrary orientation of $\mathbf{B}_0$ with respect to the crystal. One of the fields of resonance becomes stationary when the magnetic field is aligned along a principal x (z) axes of a g-tensor, corresponding to the smallest (largest) g value, respectively. From the symmetry of the crystal, 12 x axes (z axes) from three groups of four are expected, for which the spectra within each group are identical. The directions of the principal x axes of the g-tensors are found by looking for the direction of $\mathbf{B}_0$ for which a resonance occurs at the extreme high-field side of the spectrum, i.e., a direction for which this resonance shifts to lower field for any change in the direction of $\mathbf{B}_0$. Similarly, the directions of the principal z axes are determined by looking for directions of $\mathbf{B}_0$ for which the EPR spectrum contains a resonance at the extreme low-field side of the spectrum. When the magnetic field is aligned with a crystallographic axis, the four symmetry related monomers become magnetically equivalent and three bands are expected. All spectra for which $\mathbf{B}_0$ is parallel to an x axis contain a resonance at 3.303 T ($g_{xx} = 2.052$). All spectra for which $\mathbf{B}_0$ is parallel to a z axis contain a resonance at 2.910 T ($g_{zz} = 2.330$). We have been able to find the orientations of all four x axes of one group and of two x axes of another group. From the directions of the principal x axes of the g tensors of the first group, the directions of the C_2 axes were determined. The spectra with $\mathbf{B}_0$ parallel to two of these C_2 axes are shown in Fig. 2. Unexpectedly, the EPR spectra recorded along these C_2 axes (Fig. 2 g and h) show more than three bands. The extra bands must be due to additional copper sites. These bands shift with a change in the orientation of the crystal, showing that the copper sites are intrinsic to the protein. The extra signals in the EPR spectra of the crystal are the reason that we were not able to experimentally determine the directions of all 12 x and 12 z axes of the g tensors. To obtain all the directions, we start from the symmetry of the crystal and the known directions of the six principal x axes. The system is defined by 8 parameters. Three angles (α, β, γ) describe the crystallographic a, b, and c axes in the laboratory frame, three angles (δ, ε, ζ) define a g tensor of a monomer in the abc frame, two angles (θ, φ) define a C_3 axis in the abc frame. This set of 8 parameters defines a unique arrangement of the 12 g tensors in the laboratory frame. From the directions of the three C_2 axes and the six x axes the starting values of α, β, γ, δ and ε were obtained. Subsequently, the resonance positions in the experimental spectra for eight orientations of $\mathbf{B}_0$ were used in a fit procedure to determine the full parameter set. In the optimization of this set, the experimental spectra of other 12 orientations of $\mathbf{B}_0$ were taken into account as well.

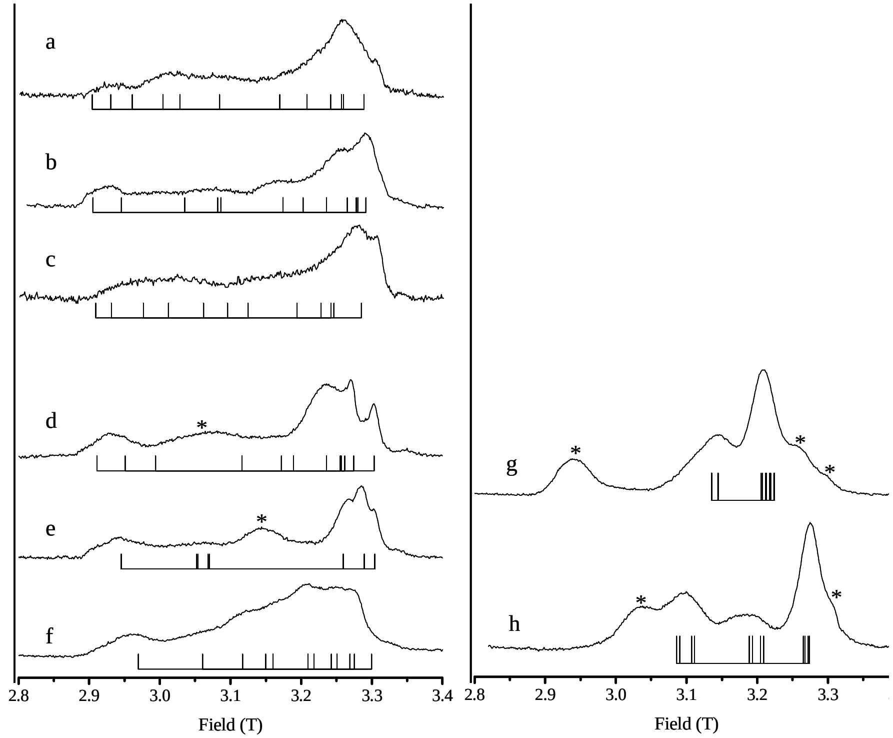

Fig. 2: The ESE-detected EPR spectra of a single crystal of *A. faecalis* nitrite reductase mutant for different orientations of the magnetic field with respect to the crystal. The sticks, underneath the experimental spectra, indicate the calculated fields of resonance of the 12 molecules in the unit cell according to the interpretation of the spectra described in the text. The spectra in panels (a), (b) and (c) correspond to orientations of the magnetic field approximately parallel to the z principal directions of the three monomers in the same asymmetric unit, those in panels (d), (e) and (f) to the x principal directions. The spectra in panels (g) and (h) correspond to the orientations of the magnetic field approximately parallel to the *a* and *b* crystallographic axes. The bands indicated by an asterisk in the panels (d), (e), (g) and (h) do not belong to the copper under study.

For the orientations of $\mathbf{B}_0$ corresponding to the spectra in Fig. 2, the resonance fields calculated with the final parameter set are shown as sticks underneath the experimental spectra. The orientations of the C_3 axes corresponding to the best fit differ by 2° from the ones derived from the X-ray diffraction study (pdb entry 1SJM [16]). A summary of the directions of all x and z axes and the C_3 axes with respect to the crystallographic axes a, b and c is shown in the Wulffnet projection [5,10] in Fig. 3.

The principal axes of the three g tensors that are related by one of the C_3 axes stem from the trimer in the asymmetric unit specified in the pdb file entry 1SJM [16]. These axes are denoted by xyz, $x^{'}y^{'}z^{'}$, $x^{''}y^{''}z^{''}$ and their orientation with respect to the a, b, and c axes is given in Tab. 1. Three assignments are possible such that the orientation of the g-tensor axes with respect to the type-2 copper site is the same for each monomer.

Table 1: Refined directions (xyz, x'y'z', x"y"z") of the principal axes of the g-tensor of the type-2 copper site of the M150E mutant of A. faecalis nitrite reductase. The directions of the g axes are specified in the crystallographic axes system (abc). The three g-tensors correspond to the three type-2 copper centers of the trimer

	a	b	c		a	b	c		a	b	c
x	-0.5341	-0.5492	0.6428	$x^{'}$	-0.2932	-0.4215	-0.8581	$x^{''}$	-0.5661	0.8241	-0.0207
y	0.2638	0.6141	0.7439	$y^{'}$	0.5018	-0.8318	0.2371	$y^{''}$	0.5456	0.3557	-0.7588
z	0.8032	-0.5669	0.1830	$z^{'}$	0.8138	0.3611	-0.4554	$z^{''}$	0.6179	0.4408	0.6510

2.4 Discussion

The type-2 copper site of NiR has been investigated by single-crystal EPR at 95 GHz. The analysis of the single-crystal data was complicated by the presence of additional copper signals. Examples of the bands of the additional copper signals are indicated by asterisks in the spectra d, e, g and h in Fig. 2.

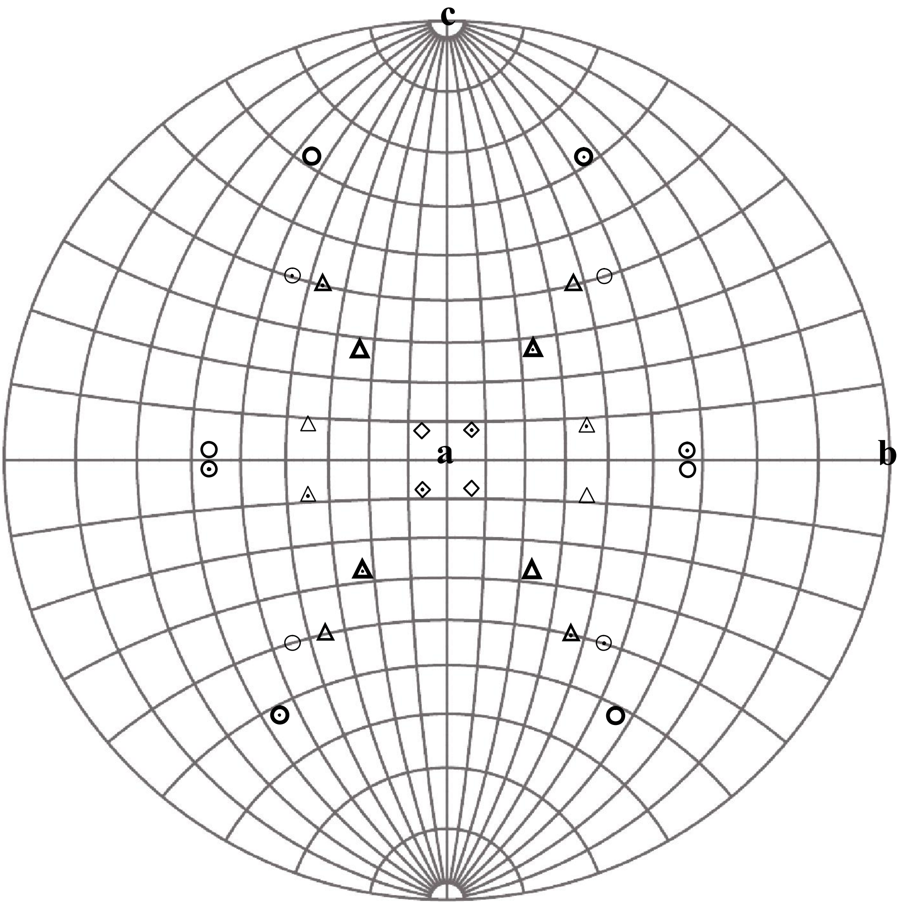

Fig. 3: Wulff stereoprojection of the principal x and z directions of the g-tensor of the 12 molecules in the unit cell. The crystallographic axes (C_2), indicated by a, b and c, are used as reference. The circles correspond to x directions, the triangles to z directions and the diamonds indicate the direction of the C_3 axes. A dot in the symbol indicates that the direction points towards the back of the sphere. The principal axes of the monomers that are related by the two-fold rotations around C_2 axes are indicated by symbols of the same thickness.

Extra signals are also observed in the EPR spectrum of the solution of the protein used for crystallization and are due to copper within the protein. The first derivative of the 95 GHz ESE-detected EPR spectrum of the frozen solution of the M150E NiR protein and its simulation are shown in Fig. 4. The fact that the spectrum obtained from the simulation of a single-copper component does not fit all the features of the experimental spectrum is a further indication that more than one type of copper contributes to the frozen solution spectrum. Whether this concerns copper bound somewhere to the protein or a different ligand conformation at the type-2 site cannot be decided at present.

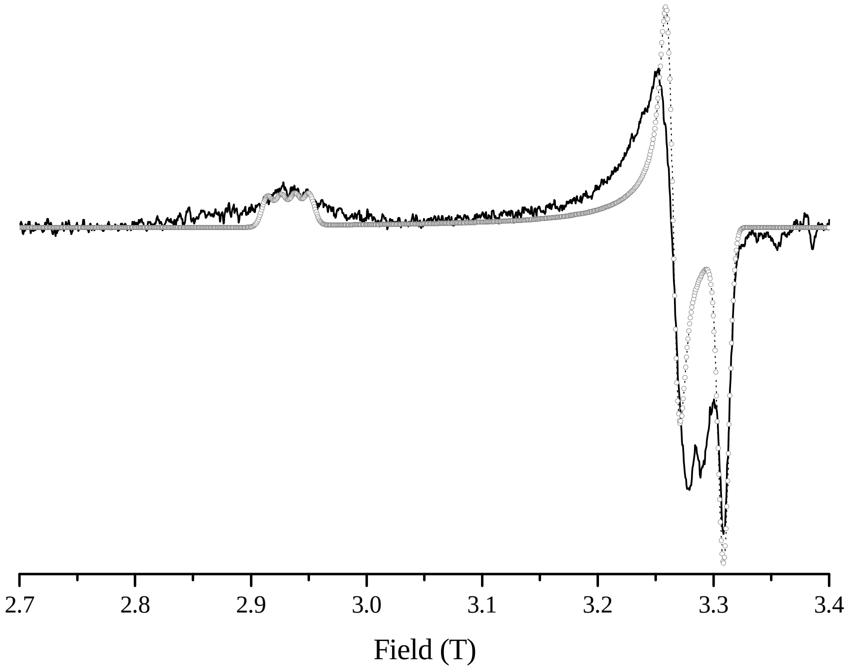

Fig. 4: The first derivative of the 95 GHz ESE-detected EPR spectrum of the frozen solution of the M150E NiR protein. The gray circled spectrum is the simulation.

Analysis of the single-crystal EPR data results in three possible orientations of the g tensor with respect to the copper site. In order to try and find the most probable assignment, we consider the orientation of the g-tensor in the copper site that results for each assignment. In Table 2, the angles between the principal axes xyz, $x'y'z'$, $x''y''z''$ of the g-tensors and the bond directions from copper to its ligands in monomer 1 (nomenclature according to the pdb entry 1SJM [16]) are given. Furthermore, the angles between the z, z' and z'' axes and the normal of the planes spanned by copper and the nitrogen atoms of two of the histidines ($\mathrm{N_{His}}$-Cu-$\mathrm{N_{His}}$) are given.

Table 2: Angles between the directions of the principal axes of the g-tensor and the Cu-N bond directions of the three histidines His306, His100, and His 135 for the type-2 copper site of the monomer 1 (from the pdb entry 1SJM[16]). Also included are the angles between z, z' and z'' axes and the normal to the planes spanned by copper and the nitrogen atoms of two of the histidines.

Bond	x	y	z	x'	y'	z'	x''	y''	z''
Cu-$\mathrm{N_{(His306)}}$	154	73	109	95	131	42	57	38	73
Cu-$\mathrm{N_{(His100)}}$	81	141	127	34	110	116	75	93	164
Cu-$\mathrm{N_{(His135)}}$	92	112	22	77	24	70	168	78	90
Plane			**z-n**			**z'-n**			**z''-n**
$\mathrm{N_{(His306)}}$-Cu-$\mathrm{N_{(His100)}}$			132			126			76
$\mathrm{N_{(His306)}}$-Cu-$\mathrm{N_{(His135)}}$			112			94			161
$\mathrm{N_{(His100)}}$-Cu-$\mathrm{N_{(His135)}}$			85			150			90

The type-2 site consists of copper ligated to three histidines with comparable Cu-N bond lengths and a water molecule (Tab. 3). The coordination is approximately tetrahedral. For the type-2 copper site the unpaired electron is expected to be in a d_{xy} type orbital, which is oriented such that it makes a good σ overlap with the lone-pair orbitals of the nitrogens of two of the histidines. For such an orbital, the z axis of the g-tensor is orthogonal to the plane of the d orbital. For the proper assignment, we expect the z axis of the g-tensor to be (close to) normal to one of the N_{His}-Cu-N_{His} planes. The smallest angle with the normal makes z'' (19°, N_{His306}-Cu-N_{His135}), which we therefore consider to be the most likely assignment. This couples the g tensor $x''y''z''$ with monomer 1. A stereo representation of the z'' and x'' axes of the g tensor in the copper site of monomer 1 is shown in Fig. 5. The orientation of the g-tensor suggests that the unpaired electron is in a molecular orbital that contains a copper d_{xy} type orbital in a σ-antibonding overlap with the lone-pair orbital of the nitrogens of His135 and His306.

Table 3: Copper-nitrogen distances and nitrogen-copper-nitrogen angles for the three histidines His306, His100, and His135 of the type-2 copper site of the monomer 1 (pdb entry 1SJM [16]). Also included is the distance between copper and the oxygen of the water ligand.

Bond	Distance (Å)
Cu-$N_{(His306)}$	2.03
Cu-$N_{(His100)}$	2.05
Cu-$N_{(His135)}$	2.05
Cu-$O_{(water)}$	2.08
	Angle
$N_{(His306)}$-Cu-$N_{(His100)}$	100
$N_{(His306)}$-Cu-$N_{(His135)}$	114
$N_{(His100)}$-Cu-$N_{(His135)}$	106

The interpretation that the unpaired electron resides in an orbital that has a strong overlap with two histidines is supported by the nitrogen hyperfine interaction of this site [8,9]. Two histidine nitrogens were found with a large hyperfine coupling, 36.7 MHz and 30.5 MHz [9]. The magnitude of these couplings suggested that the coordinated nitrogens of two histidines carry appreciable spin density, as expected for σ–overlap. The nitrogen of the third histidine was found to have a smaller hyperfine coupling, 18.8 MHz [9], showing that the third histidine is not as strongly involved in the orbital containing the unpaired electron. The present study suggests that the strongly coupled nitrogens are those of His135 and 306.

To interpret the rhombicity and the orientation of the g-tensor with respect to the site further, we used the model proposed by van Gastel et al. [3]. This model describes how the spin-orbit contribution of the copper atom relates to the g tensor by considering which d-orbitals are involved in the molecular orbital (MO) containing the unpaired electron.

As indicated before, z'' is approximately orthogonal to the N_{His306}-Cu-N_{His135} plane, revealing that the major contribution to the MO containing the unpaired electron is a d_{xy} type orbital. The 19° tilt of z'' away from the normal to the N_{His306}-Cu-N_{His135} plane suggests that the d_{xy} orbital is not the only one contributing to the MO. To facilitate the discussion, we consider a coordinate system in which **X** bisects the Cu-N_{His135} and the Cu-N_{His306} direction, and **Z** is orthogonal to the N_{His306}-Cu-N_{His135} plane. The X-ray structure of the site reveals that the plane containing His100 and the fourth ligand is almost orthogonal to the N_{His306}-Cu-N_{His135} plane, making an angle of 91°. Consequently these ligands are in the **XZ** plane. Therefore, mixing d_{xz} orbital-character into the MO containing the unpaired electron would provide overlap with the third histidine and also with the fourth ligand. According to the model, admixture of d_{xz} would rotate z'' away from **Z** as observed. For an MO that is a linear combination of d_{xy} and d_{xz}, the direction of the z axis of the g tensor should remain in the **YZ**-plane. We observe a slight tilt (25°) of z'' with respect to this plane, which underscores the limitation of this simple model.

In contrast to the effect of mixing in of the d_{z^2} orbital, admixture of orbitals such as d_{xz} does not lead to appreciable rhombicity of the site. Therefore, the rhombicity of the site (i.e., g_{yy} - g_{xx}), which amounts to 0.024, must stem from effects not included in the model, most probably the spin-orbit coupling from the oxygen of the water molecule. The rhombicity increases when NO_2^- is bound, suggesting that the nature of the fourth ligand is relevant, indeed.

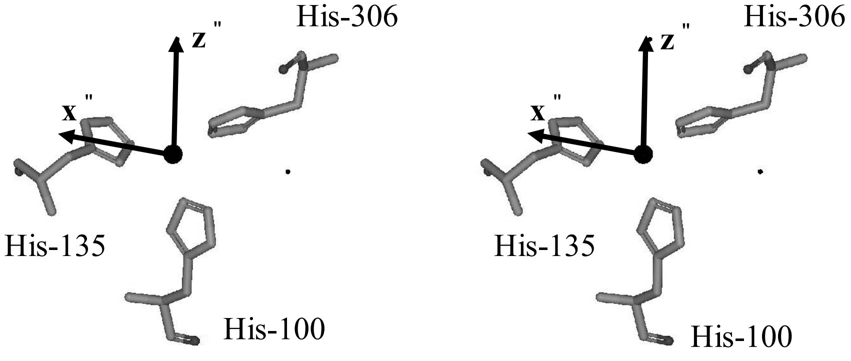

Fig. 5: Stereo representation of the z'' and x'' axes of the g-tensor in the copper site of the monomer 1.

2.4.1 Functional implications

During the reaction of the enzyme, the copper at the type-2 site receives an electron from the copper type-1 site, 12 Å away. This electron is transferred into the singly occupied molecular orbital (SOMO) of the type-2 site. Electron transfer is triggered by the binding of the substrate NO_2^- to the site, and after electron transfer NO_2^- will be converted to NO.

An intriguing conclusion from the EPR study concerns the fact that the d-orbital at the type-2 site that is the target for the electron transfer is oriented such as to overlap with His135, a residue that is adjacent to Cys136, a ligand of copper in the type-1 site. This makes the residues 136 and 135 likely candidates for the pathway of electron transfer.

Nitrite reduction requires overlap of the electron-accepting orbital of the copper with the substrate bound in the fourth position. Admixture of d_{xz} character provides the necessary overlap. Both ingredients make the type-2 site well suited to perform the nitrite reduction in this enzyme.

Acknowledgments

I would like to acknowledge the following people: Prof. Michael Murphy and Angele Arrieta prepared the NiR proteins and crystals. Dr. Sergey Milikisyants developed the fitting procedure to determine the tensor axes and Dr. Peter Gast helped with the EPR measurements.

Reference list

1. Solomon, E. I.; Baldwin, M. J.; Lowery, M. D. *Chemical Reviews* **1992,** *92* (4), 521-542.
2. Coremans, J. W. A.; Poluektov, O. G.; Groenen, E. J. J.; Warmerdam, G. C. M.; Canters, G. W.; Nar, H.; Messerschmidt, A. *Journal of Physical Chemistry* **1996,** *100* (50), 19706-19713.
3. van Gastel, M.; Canters, G. W.; Krupka, H.; Messerschmidt, A.; de Waal, E. C.; Warmerdam, G. C. M.; Groenen, E. J. J. *Journal of the American Chemical Society* **2000,** *122* (10), 2322-2328.
4. Coremans, J. W. A.; Poluektov, O. G.; Groenen, E. J. J.; Canters, G. W.; Nar, H.; Messerschmidt, A. *Journal of the American Chemical Society* **1996,** *118* (48), 12141-12153.
5. van Gastel, M.; Boulanger, M. J.; Canters, G. W.; Huber, M.; Murphy, M. E. P.; Verbeet, M. P.; Groenen, E. J. J. *Journal of Physical Chemistry B* **2001,** *105* (11), 2236-2243.
6. Godden, J. W.; Turley, S.; Teller, D. C.; Adman, E. T.; Liu, M. Y.; Payne, W. J.; Legall, J. *Science* **1991,** *253* (5018), 438-442.
7. Zumft, W. G. *Microbiology and Molecular Biology Reviews* **1997,** *61* (4), 533-540.
8. Fittipaldi, M.; Wijma, H. J.; Verbeet, M. P.; Canters, G. W.; Groenen, E. J. J.; Huber, M. *Biochemistry* **2005,** *44* (46), 15193-15202.
9. Veselov, A.; Olesen, K.; Sienkiewicz, A.; Shapleigh, J. P.; Scholes, C. P. *Biochemistry* **1998,** *37* (17), 6095-6105.
10. Coremans, J. W. A.; Poluektov, O. G.; Groenen, E. J. J.; Canters, G. W.; Nar, H.; Messerschmidt, A. *Journal of the American Chemical Society* **1994,** *116* (7), 3097-3101.
11. Prudencio, M.; Eady, R. R.; Sawers, G. *Biochemical Journal* **2001,** *353*, 259-266.
12. Wijma, H. J.; Boulanger, M. J.; Molon, A.; Fittipaldi, M.; Huber, M.; Murphy, M. E. P.; Verbeet, M. P.; Canters, G. W. *Biochemistry* **2003,** *42* (14), 4075-4083.
13. Murphy, M. E. P.; Turley, S.; Kukimoto, M.; Nishiyama, M.; Horinouchi, S.; Sasaki, H.; Tanokura, M.; Adman, E. T. *Biochemistry* **1995,** *34* (38), 12107-12117.

14. Disselhorst, J. A. J. M.; Vandermeer, H.; Poluektov, O. G.; Schmidt, J. *Journal of Magnetic Resonance Series A* **1995,** *115* (2), 183-188.
15. Stoll, S.; Schweiger, A. *Journal of Magnetic Resonance* **2006,** *178* (1), 42-55.
16. Tocheva, E. I.; Rosell, F. I.; Mauk, A. G.; Murphy, M. E. P. *Science* **2004,** *304* (5672), 867-870.

Chapter 3. Dynamics of surface spin labels in cytochrome c peroxidase studied by EPR

3.1 Introduction

Site-directed spin labeling (SDSL) has become a powerful tool for studying dynamics and conformational changes of proteins [1-3]. The basic procedure of SDSL consists in the substitution of a selected amino acid for a cysteine, followed by the modification of the reactive SH group with a selective nitroxide agent [1]. One of the most used nitroxides is the methanethiosulfonate spin label (MTSL), see Fig. 1. When studied by electron paramagnetic resonance (EPR), the analysis of the line shape of the spectra provides information about the dynamics of the nitroxide. This information is relevant because the nitroxide mobility reflects the dynamics of its binding site, such as backbone and side chains, and, in certain cases, of the whole protein.

Previous studies addressed the mobility of spin labels at sites ranging from buried to surface exposed. Here we investigate spin labels at the surface of a protein. Surface residues have the advantage that the spin labeling is easier, because the cysteine is easily accessible. Spin labels at the surface do not perturb the protein structure. They can give information about the protein surface [4] and about the interaction of the protein with its partners [5,6]. Information about which residues to target when searching for surface sites can come from the X-ray structure of the protein using solvent accessibility data [7]. Modeling the possible conformations of the spin label [8-10] is another approach.

Several methods to determine mobility from EPR spectra have been applied in the past [9,11-13]. Recently, the EasySpin-simulation program [14] has become wide spread, but it was not applied systematically to investigate mobility differences of protein spin labels. The simulations yield the rotation-correlation time (τ_c) of the spin labels.

In the present account we compare the simulation approach with the method of line-shape analysis proposed by the Hubbell group [15]. To investigate how well methods using the X-ray structure of a protein can predict mobile, exposed surface sites, we compare the mobility results to the prediction of solvent accessibility [7] and conformational freedom [16].

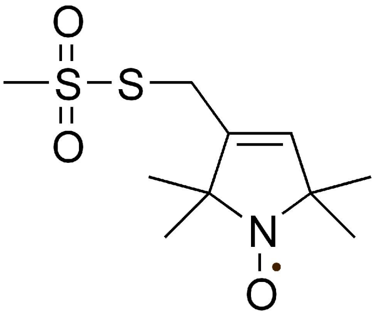

Fig. 4: Chemical structure of a nitroxide spin-label. The black dot represents the unpaired electron.

This is performed for ten spin-labeled surface sites of the cytochrome c peroxidase (CcP) protein. The mobility is measured by continuous-wave (cw) EPR in solution. We find that for surface residues with small mobility differences, the τ_c values give a better differentiation than the Hubbell model and that the conformational model [6,17] works well to predict mobilities.

3.2 Materials and Methods

3.2.1 Sample preparation

In order to prepare single-cysteine CcP variants, site-directed mutagenesis was carried out using the Quik Change^{TM} polymerase chain reaction protocol (Stratagene, La Jolla, CA) with the plasmid CCP(MKT) as a template [18]. All constructs were verified by DNA sequencing. The CcP variants were expressed in E. coli and purified following the published procedures [18-20]. Concentrations of five-coordinated high-spin ferric CcP, used in this work, were determined from the optical absorbance at 410 nm (ε = 106.1 mM^{-1} cm^{-1}) [21] and at 408 nm (ε = 98 mM^{-1} cm^{-1}) [22], respectively.

Purified single-cysteine CcP variants were incubated with 10 mM DTT in 0.1 M Tris-HCl (pH 8.0), with 0.1 M NaCl for 2 hours at room temperature, in order to reduce intermolecular disulfide bonds. The DTT was removed by passing the CcP solution through a PD-10 column (Amersham Pharmacia, Uppsala, Sweden). The resulting monomeric protein was reacted with a 7 to 10-fold excess of MTSL and incubated overnight at room temperature.

The label MTSL [(1-oxyl-2,2,5,5-tetramethyl-3-pyrroline-3-methyl)-methanethiosulfonate] was purchased from Toronto Research Chemicals (North York, ON, Canada) and used without further purification. Upon completion of the reaction, the protein solution was passed through a PD-10 column to remove any unreacted label, followed by exchange into 20 mM NaPi and 0.1 M NaCl (pH 6.0), and concentrated by ultracentrifugation using Amicon Ultra concentrators (Millipore, Billerica, MA).

3.2.2 EPR experiments

The X-band cw EPR measurements have been performed at room temperature using an ELEXSYS E 680 spectrometer (Bruker Biospin, Rheinstetten, Germany) equipped with a rectangular cavity. All measurements were performed in solution and capillaries of 1.3 mm inner diameter were used. The sample concentrations varied from 0.2 to 0.5 mM. All spectra were acquired using a modulation frequency of 100 kHz, a modulation amplitude of 0.1 mT and a microwave attenuation of at least 25 dB. The time to acquire each spectrum was up to 30 minutes. All spectra were baseline corrected by subtraction of a polynomial of first order, using the Xepr software (Bruker Biospin, Rheinstetten, Germany).

The proteins with a spin label at positions 38, 137, 200 and 288 have been measured previously, by Alex Volkov, on a Bruker ELEXSYS E 680 (Bruker Biospin, Rheinstetten, Germany) with the following parameters: modulation frequency 100 KHz, modulation amplitude 0.15 mT, microwave attenuation at least 25 dB and 5 to 25 scans [17].

3.2.3 Simulation of the EPR spectra

The EPR spectra have been simulated using *EasySpin 2.7.1* [14]. For all simulations the following tensor values were used: G = [g_{xx} g_{yy} g_{zz}] = [2.00906 2.00687 2.003] [23]; A = [A_{xx} A_{yy} A_{zz}] = [13 13 109] MHz. The line width used in the simulation of the model spectra is: 0.1 mT for the spectra simulated with τ_c values that vary from 1.00 ns to 1.55 ns; 0.4 mT for τ_c values from 2 to 3.6 ns; 1 mT for τ_c values from 4 ns to 15 ns.

3.2.4 Second-moment analysis

The line width of the EPR spectra depends amongst other factors on the dynamics. The second moment of the spectrum used to quantify this, was calculated according to the following equation

$$< \Delta \mathrm{B}^2 > = \frac{\int (B - B_F)^2 S(B) dB}{\int S(B) dB}, \tag{1}$$

where *S(B)* is the absorption spectrum, B_F and B are the first moment and the magnetic field, respectively. The absorption EPR spectra were baseline corrected using the Xepr software (Bruker Biospin, Rheinstetten, Germany) and the first and second moments were calculated numerically using MatLab (MathWorks, MA, USA). The calculated $<\Delta B^2>$ value is affected by the baseline correction and the signal-to-noise ratio of the EPR spectrum of each sample. Therefore, the value of the second moment has an error that varies between 6 % and 9 %.

3.2.5 Width of the central line

The width of the central line (ΔB) has been measured by taking the separation between the two peaks of the central line of the first-derivative EPR spectra. The presence of free spin labels affects the central line, making it sharper. This results in a smaller separation between the two peaks of the central line. Each sample has a different amount of free spin label. To minimize the error in ΔB, we have subtracted a spectrum of a free spin label from the experimental spectrum. The error in ΔB that results from this procedure varies between 9 % and 16 %.

3.2.6 Conformational model

To characterize the mobility of the nitroxide spin label attached to the surface of the CcP, all the possible orientations of the MTSL have been considered [6]. To generate these, the attached MTSL was systematically rotated around the five single bonds that join its ring to the C_α atom of the cysteine and only the sterically allowed conformers were retained for each mutant [17].

3.2.7 Solvent-accessible surface

The solvent-accessible surface has been calculated as the fractional solvent accessibility (f_{SA}). It consists of the ratio of the solvent-accessibility surface of a free residue and the solvent-accessibility surface of the same residue attached to the protein structure. The fractional solvent accessibility (f_{SA}) for native residues in CcP was computed from the crystal structure, taken from the PDB entry 2PCC [24], using the program MolMol [25] and a probe radius of 1.4 Å.

3.2.8 Protein rotation-correlation time

The rotation-correlation time of the CcP protein has been calculated from the Einstein-Stokes equation [26]

$$\tau_c = \frac{4\pi\eta_s r_h^3}{3k_B T}, \tag{2}$$

where η_s is the viscosity of the solution in centipoises, k_B the Boltzmann constant, T the temperature, and r_h the hydrodynamic radius of the protein, which was estimated according to [26]

$$r_h = \sqrt[3]{\frac{3\bar{V}M_r}{4\pi N_A}} + r_w, \tag{3}$$

where $\overline{V}$ is the specific volume of the protein, M_r is the molecular weight of the protein, N_A is the Avogadro number and r_w is the hydration radius. Assuming $\overline{V}$ = 0.73 cm^3/g, r_w = 1.6 Å and M_r = 34.2 KDa, Eq. 3 results in r_h = 5 Å. Substituting this radius into Eq. 2 and assuming η_s = η_s (0.1 M NaCl) = 1.013 centipoises [26] yields a τ_c of 12 ns.

3.3 Results

The EPR spectra of ten CcP's spin labeled at different sites (Fig. 2) have been measured at room temperature. All EPR spectra were simulated using *EasySpin* (see materials and methods). The τ_c values obtained from the simulations are given in Tab. 1.

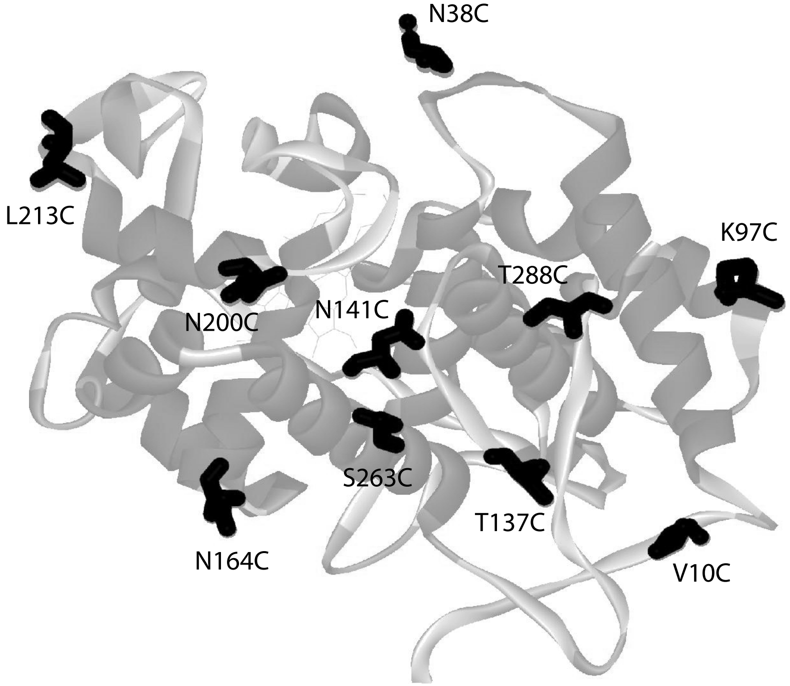

Fig. 2: Ribbon representation of the cytochrome *c* peroxidase (PDB entry 2PCC). The named residues indicate the mutated sites.

Table 1

Parameters form the simulation (τ_c), line shape analysis ($<\Delta B^2>$, ΔB), number of conformations, solvent- accessible surface and structures of ten different spin labeled sites of the Cytochrome *c* peroxidase protein.

Sample	**τ_{cs} (ns)** [*#]	**τ_{cl} (ns)** [*#]	**Second moment $<\Delta B^2>$ (T^2)**[¶]	**Line width ΔB (T)**[†]	**Number of conformations**	**Fractional solvent accessibility**
K97C	1.1 (99%)	--	$2.3*10^{-6}$	$2.3*10^{-4}$	1897	0.48
N164C	1.3 (99%)	--	$2.3*10^{-6}$	$2.8*10^{-4}$	1071	0.33
N38C	1.1 (78%)	12.0 (20%)	$2.3*10^{-6}$	$2.2*10^{-4}$	1760	0.53
T137C	1.2 (72%)	12.0 (26%)	$2.4*10^{-6}$	$2.2*10^{-4}$	655	0.24
N141C	1.1 (65%)	12.0 (28%)	$2.4*10^{-6}$	$2.1*10^{-4}$	633	0.29
V10C	1.1 (66%)	12.0 (30%)	$2.4*10^{-6}$	$2.1*10^{-4}$	567	0.23
L213C	1.3 (66%)	12.0 (32%)	$2.7*10^{-6}$	$2.6*10^{-4}$	382	0.27
S263C	1.3 (66%)	12.0 (33%)	$2.7*10^{-6}$	$2.5*10^{-4}$	344	0.10
N200C	1.2 (59%)	12.0 (40%)	$2.6*10^{-6}$	$2.4*10^{-4}$	183	0.08
T288C	1.5 (9%)	12.0 (90%)	$2.9*10^{-6}$	$3.1*10^{-4}$	29	0.07

[*] The rotation correlation time (τ_c) error is ± 0.1 ns

[†] The central line- width (ΔB) error varies between 9 % and 16 %

[¶] The second moment $<\Delta B_i^2>$ error varies between 6 % and 9 %

The weight error is ± 0.6% (± 3% for the position 137)

For two spin-labeled sites, N164C and K97C, the EPR spectra could be simulated using a single τ_c of about 10^{-9} s. All the other spectra have a multi-component line shape. Each spectrum can be described as the sum of two spectra, each simulated with a single τ_c value. The best agreement with the experimental spectrum is obtained using different weights of the two spectra (Tab. 1). The simulations of the multi-component spectra do not have a unique solution. Adequate simulations are possible using different combinations of the weights and the τ_c values. We have chosen to fix one τ_c at 12 ns (Tab. 1) for all the multi-component spectra, a value that corresponds to the predicted rotation-correlation time of the protein. Examples of experimental and simulated EPR spectra are shown in Fig. 3, where the spectra *a* and *c* concern the K97C and T288C mutants, which carry respectively the most mobile and the least mobile spin label.

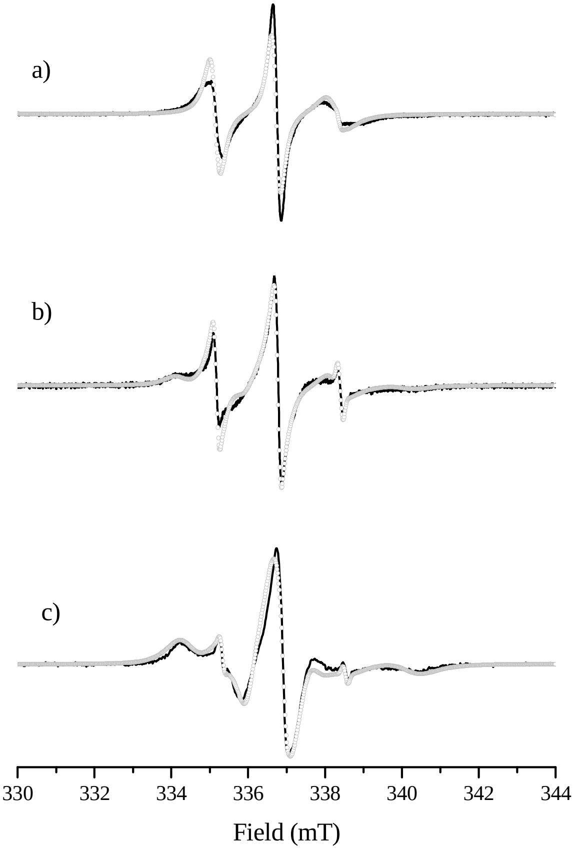

Fig. 3: The cw EPR spectra of cytochrome *c* peroxidase spin labeled at three different positions (black lines) and their simulations (gray circles). a) spin label at position 97; b) spin label at position 213; c) spin label at position 288.

Additionally, a fast component with a τ_c of about 10^{-11} s is required in the simulations. This is attributed to a small fraction of free MTSL, which varies between 1 % and 8 %.

Another approach to classify the mobility of spin labels has been proposed by Hubbell and coworkers [7,15]. It combines the peak-to-peak width of the central line in the first derivative EPR spectra (ΔB) and the second moment ($<\Delta B^2>$) (see materials and methods). At X-band frequency, ΔB and $<\Delta B^2>$ values are determined mostly by the degree of averaging of the *g* and *A* tensors. As the rotation of the nitroxide spin label slows down, the value of $<\Delta B^2>$ and ΔB increases. Thus, these parameters can be used as a measure of the mobility of the nitroxide [7,15,27]. Hubbell and coworkers plot the reciprocal of $<\Delta B^2>$ as a function of the reciprocal of ΔB to characterize the motion of the spin label attached at different sites of a protein [7,15]. The ΔB and $<\Delta B^2>$ values obtained from the EPR spectra of all the spin-labeled mutants measured in this study are summarized in Tab. 1.

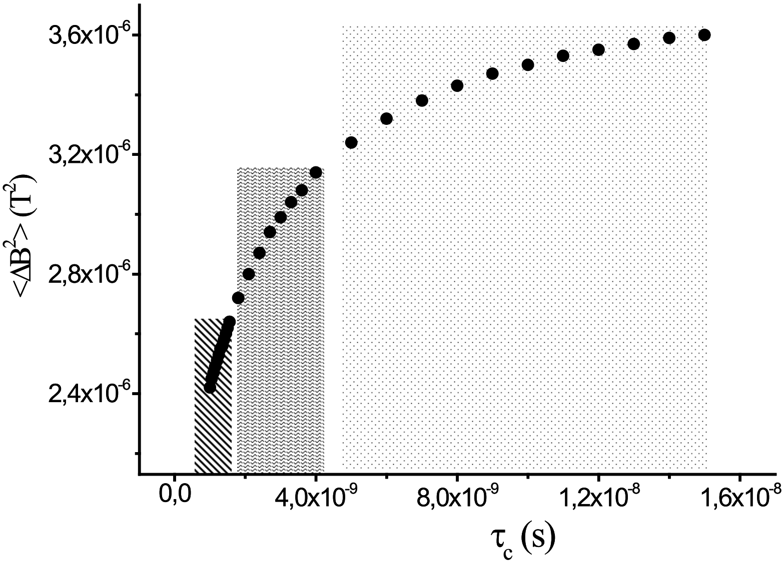

Fig. 4: The second moment ($<\Delta B^2>$) calculated from the model spectra as a function of τ_c. The regions filled with different patterns indicate, from left to right, respectively the short, intermediate and long τ_c used to simulate the model spectra.

To find a link between the ΔB and <ΔB^2> values and τ_c, EPR spectra of nitroxide spin labels have been simulated for τ_c values between 1 ns and 15 ns. From these simulated spectra, ΔB and <ΔB^2> were calculated, and graphs of <ΔB^2> and ΔB as a function of τ_c are shown in Fig. 4 and 5. Regions corresponding to large, intermediate and small values of τ_c are indicated. The width of the central line increases significantly for fast and intermediate τ_c and remains almost constant for τ_c between 4 and 15 ns. This means that ΔB can not add any further information about the spin label mobility for τ_c values bigger than 4 ns. The graph of <ΔB^2> as a function of τ_c shows that also the second moment increases significantly for short and intermediate τ_c, but continues to increase for τ_c longer than 4 ns, although to a lesser extent. The reciprocal <ΔB^2> as a function of the reciprocal ΔB calculated from the experimental EPR spectra and from the model spectra are summarized in Fig. 6.

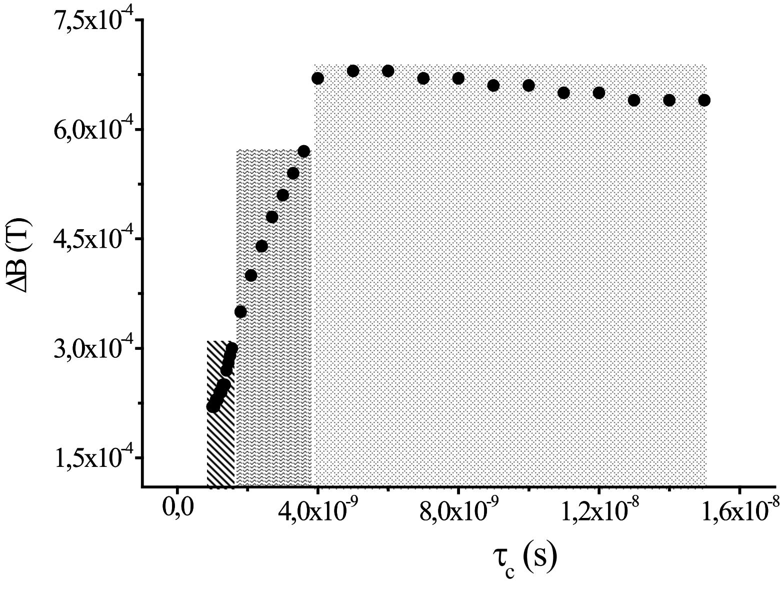

Fig. 5: The width of the central line (ΔB) of the model spectra as a function of τ_c. The regions filled with different patterns indicate, from left to right, respectively the short, intermediate and long τ_c used to simulate the model spectra.

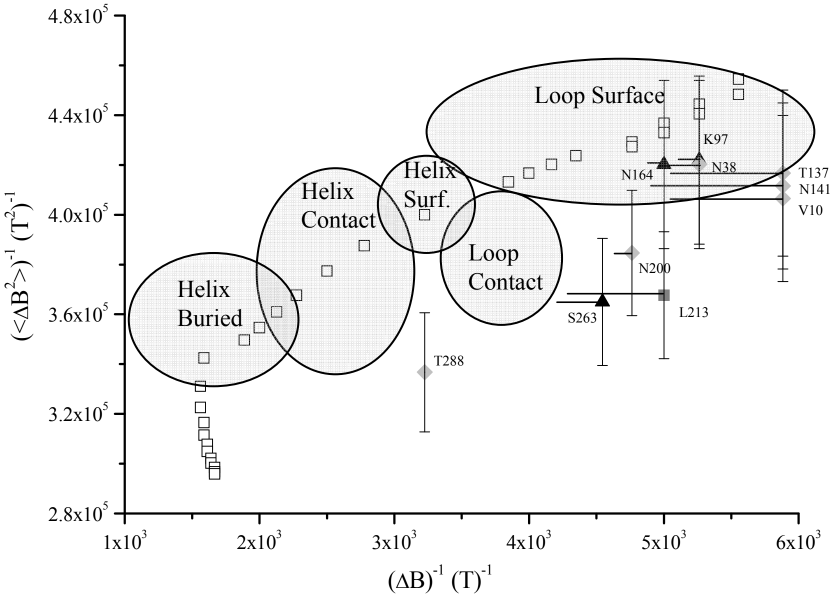

Fig. 6: The reciprocal of $<\Delta B^2>$ as a function of the reciprocal of ΔB from the experimental EPR spectra (symbols with the mutant labels) and from the model spectra (black empty squares). The triangles represent the values calculated from the spectra of the spin labels attached to a helical region, the diamonds of the spin labels attached to a loop region and the black square of the spin label attached to a β-sheet. The gray regions represent secondary structure regions in the Hubbell mobility map [7]. The source of the errors is discussed in Materials and Methods.

The buriedness of a protein residue can be quantified through the solvent accessibility, calculated as the fractional solvent accessibility (f_{SA}, see materials and methods). Hubbell and coworkers used the f_{SA} values to classify the location of the residues in the protein structure [7]. They established that residues with an $f_{SA} \leq 0.05$ can be considered as “buried”, those with an f_{SA} between 0.05 and 0.25 as “partially solvent-accessible” and those with an $f_{SA} > 0.25$ as “solvent-accessible”. The f_{SA} value for each native residue, which will be replaced by the cysteine to which the spin label binds, is reported in Tab. 1.

In Fig. 7, the solvent accessible surface area for the residues at position 97, 213 and 288 is shown.

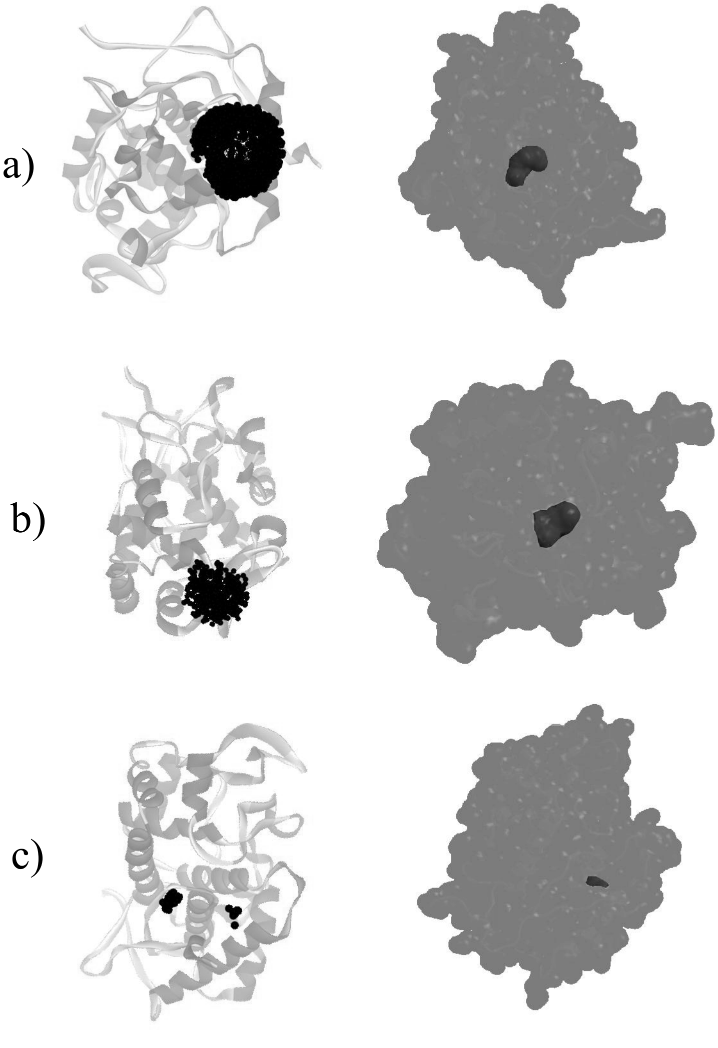

Fig. 7: Left: allowed conformations of the nitroxide spin label shown as black dots at the position of the nitroxide oxygen atom for a spin label at position (a) 97, (b) 213, and (c) 288. Right: solvent accessible surface for these residues.

In order to better understand and interpret the mobility of the nitroxide we make use of the results of the model by Volkov et al [6,17]. This model takes into account the rotational degrees of freedom of the single bonds linking the spin label to the protein backbone. It yields an ensemble of conformations which are represented by the positions of the oxygen atom of the MTSL (see Fig. 7). For our interpretation we use the number of conformations derived from the model (Tab. 1). The number of possible conformations of the spin label varies from 29 for the mutant T288C to 1897 for K97C mutant, see Tab. 1 and Fig. 7.

3.4 Discussion

The goal of this study was to use EPR to investigate the mobility of spin labels attached to ten different sites on the surface of the CcP protein.
From the τ_c values in Tab. 1, the mutants can be divided into two groups: the mutants K97C and N164C that are characterized by a single τ_c value (τ_{cs}), and the other eight mutants which, in addition to τ_{cs}, have a long τ_c (τ_{cl}).
For the mutants with two τ_c values, there must be two populations of spin labels: one corresponding to τ_{cs}, where the spin label is almost freely rotating around the bonds linking it to the protein backbone, and one corresponding to τ_{cl}, in which the motion of the spin label is more restricted. If the rotation of the spin label around the bonds linking it to the protein backbone is longer than or equal to the τ_c of the protein, the τ_c observed will be that of the protein itself. Therefore a τ_c value of 12 ns has been chosen for the second component in the simulation, corresponding to the predicted rotational-correlation time of the CcP protein (materials and methods). With the exception of the T288C mutant, the dominant contribution to the spectra comes from the τ_{cs} component. The magnitude of τ_{cs}, between 1.1 and 1.5 ns agrees well with the τ_c values of the surface residues reported by White et al. [5].
In Tab. 1, the mutants are ordered according to the mobility. The single component spectra are ordered according to τ_{cs}. For the mutants with multi-component EPR spectra, which all have the same τ_{cl} of 12 ns, the

order has been chosen according to the weight of the spectral component with the τ_{c1}. This weight varies from 20 % for N38C mutant to 90 % for T288C. A unique order is established and only the pairs T137C/N141C and L213C/S263C have values too close to be distinguished.

An alternative approach to describe the mobility of spin labels has been put forward by Hubbell and coworkers. In their model, a graph of the reciprocal $<\Delta B^2>$ values as a function of the reciprocal ΔB [7,15] serves to classify residues according to mobility and to define the secondary structure of the protein at the site of the spin label. To do so, different regions in the mobility map were defined (gray areas in Fig. 6). For example, spin labels at loop/surface sites should have the biggest values of both $<\Delta B^2>^{-1}$ and ΔB^{-1} (upper-right region of the graph in Fig.6) which correspond to highest mobility. The helix/surface, the loop/contact and the helix/contact spin labeled sites have $<\Delta B^2>^{-1}$ and ΔB^{-1} values that suggest an intermediate mobility of the attached spin label (central region of the graph in Fig. 6). The helix/buried spin labeled sites have the smallest $<\Delta B^2>^{-1}$ and ΔB^{-1} values (lower-left region of the graph in Fig. 6), which correspond to the lowest mobility.

In order to assign which τ_c values correspond to which mobility region, data points from model spectra are compared to the Hubbell mobility map (Fig. 6). Overall, the data points, simulated with a range of τ_c values, follow the trend of the Hubbell mobility regions. The loop/surface region (upper-right part of the Hubbell graph) corresponds to τ_c values that vary between 1 ns and 1.5 ns, i.e., the most mobile spin labels. The helix/surface, the loop/ contact and the helix/contact of the Hubbell map (central part of the graph) correspond to τ_c values between 1.8 ns and 3.6 ns and represent the spin labels with intermediate mobility. The helix/buried region (lower-left part of the graph) corresponds to τ_c values between 4 ns and 15 ns and represents the least mobile spin labels. There is a good correspondence of the mobility criteria given for the Hubbell graph and the τ_c values, showing that, with respect to single component spectra, the two approaches are equivalent. The τ_c values assigned to the regions were obtained for single-component-model spectra. For multi-component spectra, where slow and fast mobility components are present, there will be cases that have a different combination of $<\Delta B^2>$ and ΔB values than those of single-component spectra. The ΔB value that is sensitive to the sharpness of the central line will be affected only by the fast τ_c value. On the other hand, $<\Delta B^2>$, which is sensitive to the broadness of the spectrum, will be dominated by the effect of the slow τ_c values [15]. This means that the data points obtained from multi-component spectra can be outside the narrow band defined by the single component spectra (empty squares in Fig. 6).

The experimental data points for the surface spin labels of CcP are shown in Fig. 6. The six most mobile spin labels (at position 164, 97, 38, 137, 141 and 10) cluster in the vicinity of the loop surface region. Given the experimental error, no mobility differences can be discerned within this group. Another group comprises the spin labels at position 200, 213 and 263. From the region occupied by these data points they are less mobile than the previous six. Finally, the data point that corresponds to the spin label at position 288 is the most immobilized according to the Hubbell plot (Fig. 6). The three groups can be interpreted as Hubbell regions. The first group overlaps the loop-region of the Hubbell plot (Fig. 6) of the protein annexin [7], but the remaining mutants are outside these regions. Such a variation in the position where the regions occur has been found before [7,27]. The spin-labeled residues that belong to secondary structure elements (PDB entry 2PCC [24]) classified as loop, helical and β-sheet sites occur in almost every region, showing that for surface spin labels the secondary structure of the site is not relevant for mobility. This is similar to the results found for the spin-labeled annexin [7], but different from those for the spin-labeled SNAP-25 [27].

In the following, the mobility as obtained from the τ_c values, will be interpreted in terms of the structure of the protein. The solvent accessibility of a residue, expressed in the f_{SA} value, reveals how much a given residue is exposed to the environment. A large solvent accessibility should correspond to high mobility. The f_{SA} values show that half of the residues investigated in this study are solvent accessible, the other half partially-solvent accessible. The ranking of the f_{SA} values deviates in several aspects from the one derived from the τ_c values, showing that the predictive value of the f_{SA} values is limited.

The number of conformations derived from the model by Volkov et al. [6,17] is related to the mobility of the spin labels. A larger number of conformations means a more flexible and mobile spin label. The spin label at position 97, the most mobile site in the experiment, has the largest number of conformations. The other extreme is the spin label at position 288, which has the lowest number of conformations. The pairs

T137C/N141C and L213C/S263C, which have similar τ_c characteristics also have a similar number of conformations (Tab. 1). Thus, qualitatively the number of conformations follows the trend of the τ_c values suggesting that the model is a proper indicator for mobility.

3.5 Summary and conclusions

The presently available methods to simulate spin-label spectra to obtain τ_c values directly provide a sound ranking of the mobility of surface residues.

Fractional solvent accessibility data are well suited to identify residues that are sufficiently exposed for surface labeling. They are less well suited to predict the ranking of mobility, owing to the absence of structural parameters defining the cysteine-spin-label conformations. Here the model of Volkov et al. [6,17] or molecular dynamics approaches [9,13] are more suitable, because they explicitly take the structure of the spin label and its environment into account. The ranking obtained from the Volkov model follows closely the trend in τ_c values, suggesting that this model already reflects the essence of the mobility of the spin labels.

For surface sites, the mobility plot introduced by the Hubbell group [15] does not add much to the τ_c analysis. This derives from the small mobility differences and the errors in the parameters. The mobility plot is better suited to differentiate between spin labels that span the entire range from buried to surface residue and therefore have a larger spread of mobility. The advantage of the plot - to characterize two-component spectra in a single parameter - is partly offset by the small range of those values for sites with close lying mobility.

The disadvantage of τ_c values as a means for mobility ranking is that τ_c and the amount of slow component are interdependent, making the results somewhat dependent on the choices made for the analysis. Also, there is an extensive body of literature using the approach of the Hubbell group to classify spin labels according to their EPR properties. Before a similar collection of τ_c values for different protein types has been established, the Hubbell approach will remain the standard.

Acknowledgments

I would like to acknowledge the following people: dr. Alex Volkov performed the EPR measurements on the mutants T137C, T288C, N200C and N38C and made the calculation for the conformational model. Qamar Bashir prepared the samples. I would like also to thank dr. Marcellus Ubbink for the useful discussions and suggestions.

Reference list

1. Hubbell, W. L.; Altenbach, C. *Current Opinion in Structural Biology* **1994,** *4* (4), 566-573.
2. Hubbell, W. L.; Mchaourab, H. S.; Altenbach, C.; Lietzow, M. A. *Structure* **1996,** *4* (7), 779-783.
3. Hubbell, W. L.; Gross, A.; Langen, R.; Lietzow, M. A. *Current Opinion in Structural Biology* **1998,** *8* (5), 649-656.
4. Finiguerra, M. G.; Blok, H.; Ubbink, M.; Huber, M. *Journal of Magnetic Resonance* **2006,** *180* (2), 197-202.
5. White, G. F.; Ottignon, L.; Georgiou, T.; Kleanthous, C.; Moore, G. R.; Thomson, A. J.; Oganesyan, V. S. *Journal of Magnetic Resonance* **2007,** *185* (2), 191-203.
6. Volkov, A. N.; Worrall, J. A. R.; Holtzmann, E.; Ubbink, M. *Proceedings of the National Academy of Sciences of the United States of America* **2006,** *103* (50), 18945-18950.
7. Isas, J. M.; Langen, R.; Haigler, H. T.; Hubbell, W. L. *Biochemistry* **2002,** *41* (5), 1464-1473.
8. Borbat, P. P.; Mchaourab, H. S.; Freed, J. H. *Journal of the American Chemical Society* **2002,** *124* (19), 5304-5314.
9. Steinhoff, H. J.; Muller, M.; Beier, C.; Pfeiffer, M. *Journal of Molecular Liquids* **2000,** *84* (1), 17-27.
10. Sale, K.; Sar, C.; Sharp, K. A.; Hideg, K.; Fajer, P. G. *Journal of Magnetic Resonance* **2002,** *156* (1), 104-112.
11. Budil, D. E.; Lee, S.; Saxena, S.; Freed, J. H. *Journal of Magnetic Resonance Series A* **1996,** *120* (2), 155-189.
12. Columbus, L.; Kalai, T.; Jeko, J.; Hideg, K.; Hubbell, W. L. *Biochemistry* **2001,** *40* (13), 3828-3846.
13. Steinhoff, H. J.; Hubbell, W. L. *Biophysical Journal* **1996,** *71* (4), 2201-2212.
14. Stoll, S.; Schweiger, A. *Journal of Magnetic Resonance* **2006,** *178* (1), 42-55.
15. Mchaourab, H. S.; Lietzow, M. A.; Hideg, K.; Hubbell, W. L. *Biochemistry* **1996,** *35* (24), 7692-7704.
16. Finiguerra, M. G.; Prudencio, M.; Ubbink, M.; Huber, M. *Magnetic Resonance in Chemistry* **2008,** *46* (12), 1096-1101.

17. Volkov A. Transient Complexes of Haem Proteins. Leiden University, Leiden, Feb 2007.
18. Goodin, D. B.; Davidson, M. G.; Roe, J. A.; Mauk, A. G.; Smith, M. *Biochemistry* **1991,** *30* (20), 4953-4962.
19. Pollock, W. B. R.; Rosell, F. I.; Twitchett, M. B.; Dumont, M. E.; Mauk, A. G. *Biochemistry* **1998,** *37* (17), 6124-6131.
20. Morar, A. S.; Kakouras, D.; Young, G. B.; Boyd, J.; Pielak, G. J. *Journal of Biological Inorganic Chemistry* **1999,** *4* (2), 220-222.
21. Margoliash, E.; Frohwirt, N. *Biochemical Journal* **1959,** *71*, 570-578.
22. Vitello, L. B.; Huang, M.; Erman, J. E. *Biochemistry* **1990,** *29* (18), 4283-4288.
23. Steigmiller, S.; Borsch, M.; Graber, P.; Huber, M. *Biochimica et Biophysica Acta-Bioenergetics* **2005,** *1708* (2), 143-153.
24. Pelletier, H.; Kraut, J. *Science* **1992,** *258* (5089), 1748-1755.
25. Koradi, R.; Billeter, M.; Wuthrich, K. *Journal of Molecular Graphics* **1996,** *14* (1), 51-&.
26. Cavanagh, J.; Fairbrother, W. J.; Palmer III, A. G.; Skelton, N. J. *Protein NMR Spectroscopy: Principles and Practice;* Academic Press: London, 1995.
27. Margittai, M.; Fasshauer, D.; Pabst, S.; Jahn, R.; Langen, R. *Journal of Biological Chemistry* **2001,** *276* (16), 13169-13177.

Chapter 4. Aggregation of transmembrane peptides studied by spin-label EPR

4.1 Introduction

The assembly and folding of membrane proteins, and the association of these proteins inside the membrane depend strongly on the balance between protein-protein and protein-lipid interactions. Peptides forming transmembrane (TM) α-helices and their interactions with phospholipid bilayers serve as models to define the elementary aspects of the protein-membrane interactions governing the properties of TM proteins (Fig. 1a). The WALP peptide (Acetyl-GWWL(AL)$_n$WWA-amide) is one of the paradigmatic TM peptides and its properties have been studied in various membrane environments. [2-6]

The response of peptides and ultimately membrane proteins to changes in membrane conditions depends on the balance of peptide-peptide, peptide-lipid and lipid-lipid interactions. Consequently, the type of lipid (saturated vs unsaturated) and the membrane phase (gel phase vs. liquid-crystalline phase) are important factors. One of the intriguing and potentially biologically relevant responses of the peptides to different membrane conditions is aggregation. Since membrane systems are intrinsically disordered and dynamic, many conventional methods for structure investigation cannot be employed to monitor peptide aggregation. Also, often these methods can only probe aggregation in certain lipids or phases of the membrane, for example, because the phase of interest occurs in an inaccessible temperature range. Thus, a combination of methods is needed to address the question of how the balance of forces in peptide-membrane interactions does influence peptide aggregation.

For WALP peptides it has been shown by atomic force microscopy (AFM) and fluorescence techniques, that they form linear aggregates in the gel-phase of a saturated lipid (DPPC).[1,7,8] In the liquid-crystalline phase of the same lipid, the AFM signatures of aggregation disappear and excimer fluorescence is strongly reduced.[1,8] Also, in the liquid-crystalline phase of an unsaturated lipid (DOPC) a low level of aggregation was detected by fluorescence.[9] However, aggregation in the gel phase of DOPC has not been investigated.

Here we present spin-label EPR to probe peptide-membrane interactions in relation to peptide aggregation. We show that it is applicable to different lipid systems over a wide temperature range, including low temperatures where also unsaturated lipids form a gel-phase. Spin-label EPR has been used in different ways to investigate membrane-peptide systems,[6,10,11] but the present approach is novel in that the peptide-peptide interaction is directly probed by spin-labeling the peptide in combination with diamagnetic dilution of the samples.

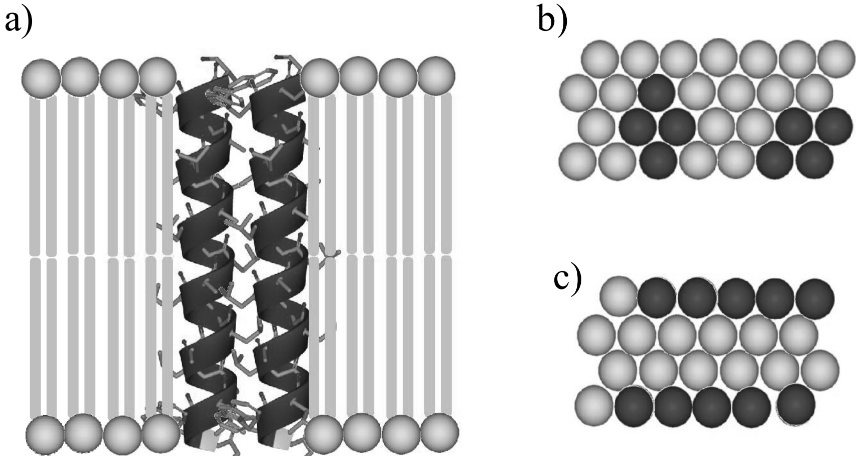

Fig. 1: Schematic representation of WALP peptides in a gel-phase lipid bilayer. (a) Lipid bilayer, lipid head groups (gray), lipid chains, WALP helices, side view. (b) Peptide cluster aggregates, top view. (c) Peptide linear aggregates, top view.

Diamagnetic dilution is an approach that has previously been used to avoid line broadening by spin-spin interactions.[12,13] Here we used it for the following reason. In aggregates, the short distances between the spin labels due to the close approach of the peptides cause characteristic changes in the EPR spectra that serve as an observable for aggregation under the membrane condition in question. Because different membrane conditions by themselves also can result in different spectral properties of the spin label, one needs to be able to distinguish these effects from the spin-spin interaction caused by aggregation. In diamagnetically diluted samples, the spin-labeled peptide is diluted by an excess of unlabelled peptide while all other parameters, i.e. the temperature, the type of lipid, and the total lipid-peptide ratio, are kept the same. Thus, aggregation can be detected simply as the spectral difference between samples containing labeled peptide only and diamagnetically diluted samples.

Here, the interaction of WALP23 (WALP), where 23 indicates the number of residues, with the liquid-crystalline phases and the gel phases of two lipids, DPPC and DOPC, is investigated. The spin label is introduced at a central position[14] of WALP that is within the membrane (SL-WALP) or close to the N- or C-terminal end of WALP (SL-N-WALP or SL-C-WALP). The sequences of these peptides are given in Table 1.

Table 1

Peptides and their amino acidic sequences

peptide	**amino acidic sequence**
WALP23	Ac-GWWLALALALALALALALWWA-NH_2
C(N)-WALP	Ac-CGWWLALALALALALALALWWA-NH_2
C(C)-WALP	Ac-GWWLALALALALALALALWWC-NH_2
C12-WALP	Ac-GWWLALALALACALALALALWWA-NH_2

Similar to previous studies,[1,7,8] we find that WALP aggregates in the gel-phase of the saturated lipid DPPC. At the measurement temperature of 120 K, cluster aggregates prevail, with no apparent preference for parallel or anti-parallel arrangement, whereas other studies, performed at higher temperature, indicated a preference for anti-parallel aggregates.[1,9,14] We hypothesize that at the lower temperature lipid-lipid interactions are stronger than at 297 K, causing the transition from antiparallel line aggregates to cluster aggregates. We also monitored WALP aggregation for the first time in the gel phase of DOPC and found that aggregation is less extensive than in DPPC. These studies allow us to discriminate between the contributions of specific membrane properties, like the phase of the lipids or the saturation of the lipid fatty acid chains, to peptide aggregation.

4.2 Materials and Methods

4.2.1 Sample preparation

The lipids DOPC (1,2-dioleoyl-*sn*-glycero-3-phosphocholine) and DPPC (1,2-dipalmitoyl-*sn*-glycero-3-phosphocholine) were purchased from Avanti Polar Lipids (Birmingham, AL) and used without further purification.

The spin label reagent, methanethiosulfonate-(1-oxyl-2,2,5,5-tetramethylpyrroline-Δ3-methyl) (MTSL), was purchased from Toronto research chemicals (North York, ON). The reagents used for the synthesis and labeling of the peptides were obtained from commercial sources.

The peptides WALP23, C(N)-WALP and C(C)-WALP (table 1) were synthesized as described previously.[1] The peptide C12-WALP (table 1) was synthesized manually, using the same synthesis protocol.

The MTSL label was attached to all three cysteine-containing peptides via a disulfide bridge. A typical labeling experiment proceeded as follows: A clear solution of 10 μmol (~25 mg) C(N)-, C(C)- or C12-WALP in 2.5 ml trifluoroethanol (TFE) was purged with N_2 for 5 min. While keeping the solution under N_2-atmosphere, 10 μl of triethylamine and a N_2-purged solution of 12.5 μmol (3.3 mg) MTSL in 1 ml TFE were added. The reaction mixture was stirred for 48 hr at 4°C and in the dark. The labeled peptides, SL-N-WALP, SL-C-WALP and SL-WALP, were precipitated in cold tert-butyl methyl ether/n-hexane (1:1) and lyophilized from tert-butanol/water (1:1) and obtained in yields of at least 72%.

The peptides were characterized by MALDI-ToF (Kratos Axima, ACTH (18-39) external standard, α-cyano-4-hydroxycinnamic acid matrix) and electro-spray ionization mass spectrometry (ESI-MS, Finnigan LCQ DecaXP Max mass spectrometer operating in positive-ionization mode). The relative intensities of the peaks were not influenced by increased ionization efficiency due to the label, as checked by comparison of mass spectra of (mixtures of) labeled and unlabeled peptides.

In all labeling experiments only the mass of the labeled WALP (Na^+-ionized form) was found: SL-C-WALP; calculated: $[M+H]^+_{ave}$ 2793.53, found: $[M+Na]^+_{ave}$ 2815.27. SL-N-WALP; calculated: $[M+H]^+_{ave}$ 2807.55, found: $[M+Na]^+_{ave}$ 2829.19. SL-WALP; calculated: $[M+H]^+_{ave}$ 2697.36, found: $[M+Na]^+_{ave}$ 2719.48, $[M+K]^+_{ave}$ 2735.46. Based on these results the labeling-efficiency was estimated to be at least 90%.

The samples preparation procedure is described in reference [10] and the lyophilized WALP was dissolved in TFE. The concentration of this stock solution was determined by the absorbance of the tryptophan (trp) at 280 nm using an extinction coefficient of 22400 M^{-1} cm^{-1}. The desired amount of WALP stock solution was transferred into a glass vial and the TFE was evaporated by a nitrogen gas stream. The resulting peptide film was re-dissolved in 50 μl of TFE. This step was repeated one more time. Finally, the peptide film was dissolved in 50 μl of TFE and the desired amount of lipids in chloroform was added. The lipid-peptide solution was dried using a nitrogen gas stream followed by vacuum drying overnight. The peptide-lipid film was hydrated in buffer: 50 mM of Tris at pH 7.5 and 100 mM of NaCl. The sample was then subjected to 10 freeze-thaw cycles, using liquid nitrogen and a water bath at 50° C, respectively. The resulting multilamellar vesicles were dispersed by vigorous vortexing before the measurement.

The peptide-lipid ratio (P/L) is given as the molar ratio. Unless otherwise stated the peptide/lipid ratio is 1/100. The concentration of labeled peptides was kept between 100 and 250μM for all measurements, for the measurements at 120 K 20% glycerol was added to obtain a frozen glass. The diamagnetically diluted samples (dd-SL-WALP) contain the same amount of SL-WALP, but additional unlabeled WALP to result in a fraction of 10% or 20% labeled peptides.

4.2.2 EPR experiments

The X-band cw EPR measurements were performed using an ELEXSYS E 680 spectrometer (Bruker, Rheinstetten, GE) equipped with a helium gas-flow cryostat and a rectangular cavity. For the measurements in frozen solution, 4 mm outer diameter quartz sample tubes were used and samples were frozen in liquid nitrogen before inserting them in the pre-cooled helium gas-flow cryostat. The EPR spectra were recorded using a modulation amplitude of 2 G and a microwave attenuation of at least 23 dB. Typical accumulation times have been 28 min.

For measurements in liquid solution, where capillaries of 1.3 mm inner diameter were used, the modulation amplitude was adjusted to avoid lineshape distortions, typical value was 0.4 G. To control the sample temperature during measurements above room temperature a nitrogen gas-flow cryostat was used. The EPR spectra were recorded using a microwave attenuation of 15 dB; the total measurement time was up to 70 minutes.

All spectra were acquired using a modulation frequency of 100 kHz. The spectra were baseline corrected and normalized to the same number of spins.

4.2.3 Simulation of the EPR spectra

The cw EPR solution spectra were simulated using *EasySpin 2.6.0.* [15] For all simulations the following tensor values were used: $G = [g_{xx}\ g_{yy}\ g_{zz}] = [2.00906\ 2.00687\ 2.00300]$; [16] $A = [A_{xx}\ A_{yy}\ A_{zz}] = [13\ 13\ 96]$ MHz.

A superposition of a mobile component in the fast motion regime and a less mobile component in the slow motion regime was used. The fraction of the mobile component was smaller than 1 %.

4.2.4 Second-moment analysis

Since the line width of the EPR spectra depends amongst other factors also on the spin-spin interaction, the spectral second moment was used to quantify this interaction. In all experiments, a sample of a monomer, with a spectrum $S_M(B)$ was compared to a sample in which the spin-spin interaction is present $S_D(B)$. The difference of spectral second moments $<\Delta B^2>$ was calculated according to the following equation: [17]

$$<\Delta\Delta B^2> = \frac{\int (B-B_{FD})^2 S_D(B)dB}{\int S_D(B)dB} - \frac{\int (B-B_{FM})^2 S_M(B)dB}{\int S_M(B)dB} \tag{1}$$

where $S_D(B)$ is the absorption spectrum broadened due to dipolar spin-spin interaction, $S_M(B)$ is the absorption spectrum without spin-spin-interaction, B_{FD}, B_{FM} and B are the first spectral moments and the magnetic field, respectively. Second moments are defined as $<\Delta B_M^2>$ for the non-interacting and $<\Delta B_D^2>$ for the interacting case.

The absorption EPR spectra were baseline corrected using Xepr software (Bruker Biospin, Rheinstetten, Germany) and the first and second moment were calculated numerically using MatLab (MathWorks, MA, USA).

4.3 Results

The EPR spectra of SL-WALP were measured at different temperatures in the presence of membranes (multi-lamellar vesicles) composed of DOPC or DPPC lipids.

Label efficiency. The labeling degree and basic characteristics of the WALP samples are best judged by room-temperature EPR. In these spectra, spin-labeled WALP has a characteristic line-shape that can be identified in the simulation as a broadened spectrum (Fig. 2: 308 K) and a rotation correlation time τ_R = 2.3 ns (Table 2). A quantitative comparison of the EPR signal intensity to a reference sample with known spin concentration revealed that more than 90% of the peptides are spin labeled, in agreement with the mass-spectrometry results (see Material and Methods).

Additionally, a fast motion component is required in the simulation, which is attributed to a fraction of free MTSL. In all cases, this fraction is below 1 %, showing that free MTSL is efficiently removed by the post-labeling purification procedure.

Table 2

Parameters from the simulation (τ_c, ΔB) and the second moment analysis ($<\Delta B^2>$, $<\Delta\Delta B^2>$) of pure SL-WALP and dd-SL-WALP in DOPC and DPPC

sample	temperature (K)	correlation time τ_c (ns) [a]	line width ΔB (T) [b]	second moment $<\Delta B^2>$ (T^2) [c,d]	broadening $<\Delta\Delta B^2>$ (T^2)
dd-SL-WALP DPPC	120	---	---	$2.8*10^{-6}$	$4.5*10^{-6}$
SL-WALP DPPC	120	---	---	$7.3*10^{-6}$	
dd-SL-WALP DPPC	290	5.8	$4.2*10^{-4}$	$2.6*10^{-6}$	$2.0*10^{-6}$
SL-WALP DPPC	290	5.8	$8.1*10^{-4}$	$4.6*10^{-6}$	
dd-SL-WALP DPPC	308	2.3	$1.2*10^{-4}$	$2.1*10^{-6}$	$1.1*10^{-6}$
SL-WALP DPPC	308	2.3	$2.8*10^{-4}$	$3.2*10^{-6}$	
dd-SL-WALP DPPC	333	1.2	$1.1*10^{-4}$	$2.3*10^{-6}$	$0.1*10^{-6}$
SL-WALP DPPC	333	1.2	$1.3*10^{-4}$	$2.4*10^{-6}$	
dd-SL-WALP DOPC	120	---	---	$2.8*10^{-6}$	$2.6*10^{-6}$
SL-WALP DOPC	120	---	---	$5.4*10^{-6}$	
dd-SL-WALP DOPC	240	---	---	$2.5*10^{-6}$	$0.8*10^{-6}$
SL-WALP DOPC	240	---	---	$3.3*10^{-6}$	
dd-SL-WALP DOPC	260	---	---	$2.1*10^{-6}$	$-0.1*10^{-6}$
SL-WALP DOPC	260	---	---	$2.0*10^{-6}$	
dd-SL-WALP DOPC	290	2.2	$1.1*10^{-4}$	$2.2*10^{-6}$	$0.2*10^{-6}$
SL-WALP DOPC	290	2.2	$1.8*10^{-4}$	$2.4*10^{-6}$	

[a] The rotation correlation time (τ_c) error is ± 0.1 ns

[b] The intrinsic line width (ΔB) error is ± $0.1*10^{-4}$ T

[c] The subscript i indicates the second moment for the spectra with and without spin-spin interaction

[d] The second moment $<\Delta B^2>$ error is ± $0.2*10^{-6}$ T^2

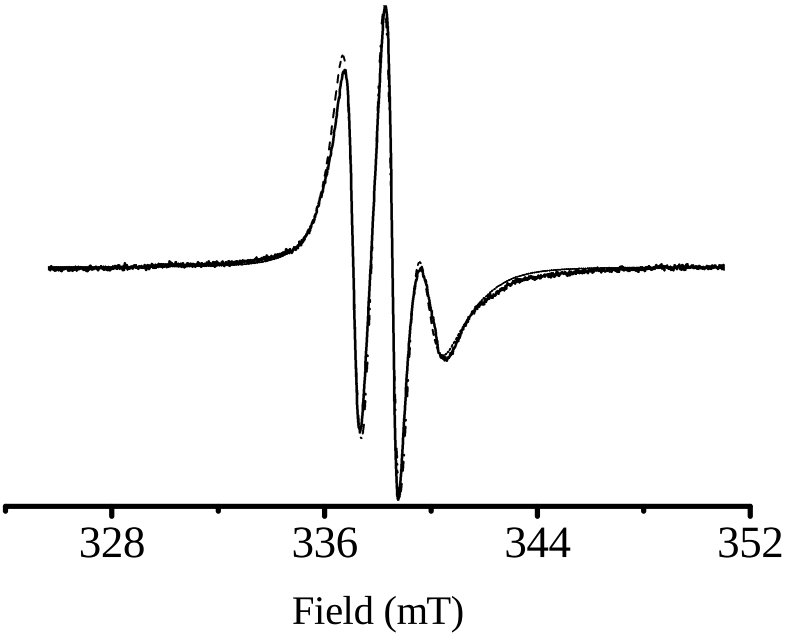

Fig. 2: The cw EPR spectrum of spin-labeled WALP at 308 K and its simulation. Pure SL-WALP in DPPC (solid line); simulation (dashed line). (For the simulation parameters see “Materials and methods” and Table 1).

EPR at 120 K. Fig. 3 shows EPR frozen solution spectra (T =120 K) of pure SL-WALP in DOPC and DPPC and of diamagnetically diluted (dd) SL-WALP in DPPC. The spectrum of dd-SL-WALP in DOPC, not shown in the picture, is identical to the one in DPPC. The phase-transition temperature (T_m) between the liquid-crystalline phase (higher temperature) and the gel phase (lower temperature), of DOPC and DPPC is 253 K and 314 K respectively, 18 so at the measurement temperature of 120 K both lipids are in the gel phase. Both the dd-SL-WALP and SL-WALP spectra can be well simulated as immobilized powder spectra. From the dd-SL-WALP spectra the hyperfine tensor (A) and the g-tensor (G) parameters are obtained. The spectra are normalized to the same number of spins, therefore, the smaller amplitude of the spectra of SL-WALP in DPPC and in DOPC relative to the spectrum of dd-SL-WALP reflects the broadening of the spectra of the SL-WALP samples.

For SL-WALP in DPPC, the spectra are more broadened than those of the SL-WALP in DOPC. To test the conditions for diamagnetic dilution, a sample composed of 10% SL-WALP and 90% WALP (10% dd-SL-WALP) was compared to a mixture of 20% SL-WALP with 80% WALP in DPPC, (20% dd-SL-WALP).

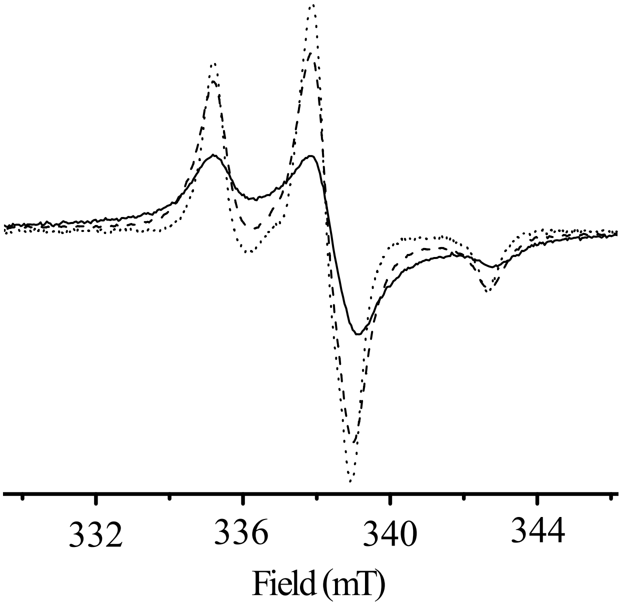

Fig. 3: The cw EPR spectra of spin-labeled WALP at 120 K. Pure SL-WALP in DOPC (dashed line); experimental conditions: microwave (mw) attenuation: 29 dB; total acquisition time: 14 min. Pure SL-WALP in DPPC (solid line); mw attenuation: 23 dB; total measurement time: 28 min; and dd-SL-WALP (10%) in DPPC (dotted line); mw attenuation: 38 dB; total measurement time: 56 min. All spectra, P/L: 1/100. Spectra are normalized to the same number of spins. (For the remaining experimental parameters see "Materials and methods").

The spectra of both samples were identical, showing that spin-spin interactions do not contribute to the lineshape for 10% and 20% dd-WALP. In the following, both 10% and 20% SL-WALP are referred to as dd-SL-WALP.

The width of the spectra is given by the second moment of the spectra ($<\Delta B_i^2>$), and the broadening is expressed by $<\Delta B_D^2> - <\Delta B_M^2> = <\Delta\Delta B^2>$, where $<\Delta B_D^2>$ is the second moment of the SL-WALP sample, $<\Delta B_M^2>$ is the second moment of the dd-SL-WALP sample and $<\Delta\Delta B^2>$ the difference in the second moment. The second moments of the EPR spectra are given in Table 2. Positive $<\Delta\Delta B^2>$ values reveal broadening, and in the following positive $<\Delta\Delta B^2>$ values will be referred as broadening. The $<\Delta\Delta B^2>$ value of SL-WALP in DPPC is bigger than the value found for the SL-WALP in DOPC. This indicates that at 120 K WALP has a higher degree of aggregation in DPPC than in DOPC (see Discussion). Different P/L ratios of SL-WALP in DOPC and DPPC were measured. For DPPC, the same line shape was observed for P/L ratios of 1/30 and 1/100, for DOPC the line was a little wider for the P/L ratio of 1/30, without, however, resulting in a significant increase in $<\Delta\Delta B^2>$. This indicates that the P/L ratios in that range do not significantly affect the spin-spin interaction.

To investigate whether there is a preferred arrangement, i.e. parallel or anti-parallel, of the WALP molecules in the membrane, a set of experiments was performed with WALP spin labeled at the N- or the C-terminal positions (SL-N-WALP and SL-C-WALP). The $<\Delta\Delta B^2>$ values for SL-N- and SL-C-WALP in DPPC are smaller than those for SL-WALP in the same membrane environment, due to increased motional freedom of the label, yet the broadening remains significant (Table 3). Spectra of SL-N-WALP and SL-C-WALP, mixed in the same sample were indistinguishable from the spectra of SL-N-WALP and SL-C-WALP measured separately, suggesting that there is no preferred alignment in DPPC at 120 K (see Discussion). For DOPC, the SL-N- and SL-C-WALP spectra have such small $<\Delta\Delta B^2>$ values that it was not possible to analyze the difference between pure SL-N-WALP resp. SL-C-WALP and the mixed sample.

Table 3
Parameters form second moment analysis ($<\Delta B^2>$, $<\Delta\Delta B^2>$) of pure SL-C-WALP and SL-C/N-WALP and dd-SL-C-WALP and dd-SL-C/N-WALP in DPPC.

sample	temperature (K)	second moment $<\Delta B^2>$ (T^2) [a b]	broadening $<\Delta\Delta B^2>$ (T^2)
dd-SL-C-WALP DPPC	120	$4.0*10^{-6}$	$1.1*10^{-6}$
SL-C-WALP DPPC	120	$5.1*10^{-6}$	
dd-SL-N/C-WALP DPPC	120	$4.0*10^{-6}$	$1.1*10^{-6}$
SL-N/C-WALP DPPC	120	$5.1*10^{-6}$	

[a] The subscript i indicates the second moment for the spectra with and without spin-spin interaction

[b] The second moment $<\Delta B^2>$ error is ± $0.2*10^{-6}$ T^2

EPR at temperatures higher than 120 K. Below 240 K, both DPPC and DOPC are in the gel phase, and at 120 K, the spectra of dd-SL-WALP revealed complete immobilization. At 240 K DOPC is still in the gel-phase, but the line-shape of dd-SL-WALP (Fig. 4a) deviates from that of the immobilized spin label towards a more mobile form. The line-narrowing expected for the higher mobility is also reflected in the trend towards smaller $<\Delta B^2>$ values (Table 2). Also, the $<\Delta\Delta B^2>$ value is reduced relative to the value at 120 K (for interpretation, see Discussion). At 260 K, above the T_m of DOPC, where the lipids are in the liquid-crystalline phase, the spectra of dd-SL-WALP and SL-WALP are indistinguishable (Fig. 4b). The second moment $<\Delta B^2>$ of dd-SL-WALP is again reduced relative to the value of 240 K, and it is identical within experimental error to the value of SL-WALP, i.e. $<\Delta\Delta B^2>$ vanishes (Table 2). Also, at room temperature (290 K), no significant broadening was observed (Table 2).

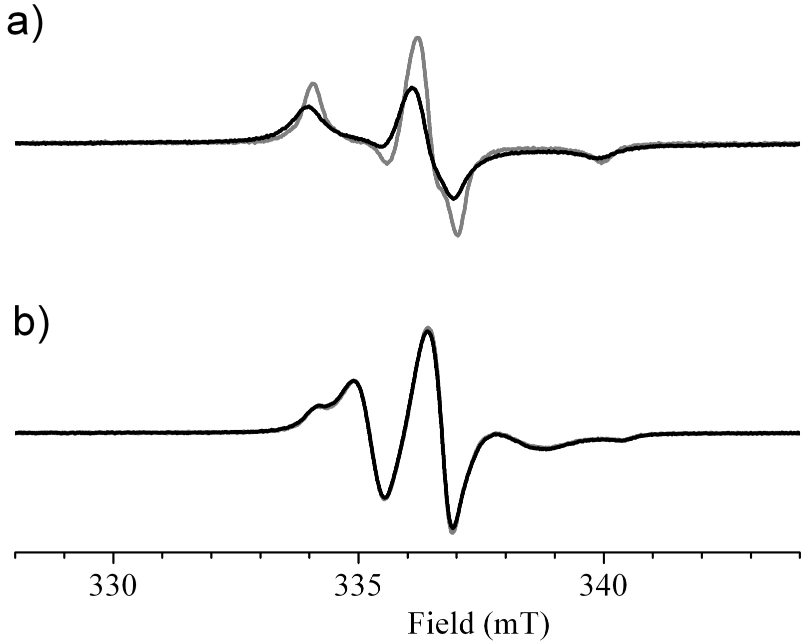

Fig. 4: The cw EPR spectra of spin-labeled WALP in DOPC, below and above T_m. (a) The pure SL-WALP spectrum at 240K (black), the dd-SL-WALP (20%) spectrum at 240 K (grey). (b) The SL-WALP spectrum at 260 K (black). The dd-SL-WALP (20%) spectrum at 260 K (grey). For all spectra, P/L ratio: 1/100. Spectra are normalized to the same number of spins. (For the remaining experimental parameters see "Materials and methods").

The T_m of DPPC is higher than that of DOPC, therefore, the respective experiments for DPPC are performed at a higher temperature. The Fig. 5a and 5b show EPR of pure and dd-SL-WALP in DPPC, at 290 K and at 308 K, i.e. below T_m. At both temperatures, the SL-WALP is significantly broadened with respect to the diamagnetically diluted one. The spectra were simulated using standard liquid solution parameters, resulting in rotation correlation times τ_R in the ns-time regime. Spectra of SL-WALP and dd-SL-WALP under identical membrane conditions could be simulated with identical values for τ_R but a larger ΔB for the pure SL-WALP (Table 2). Fig. 5c shows EPR liquid-solution spectra of pure and diamagnetically diluted SL-WALP in DPPC at 333 K. At this temperature, which is above the T_m, DPPC is in the liquid-crystalline phase. The spectrum of SL- WALP (Fig. 5c) has a lower intensity, suggesting that the spectrum is slightly broader than the one of dd-SL-WALP. However, this broadening is not sufficient to lead to a $<\Delta\Delta B^2>$ value that is significantly above zero (Table 2).

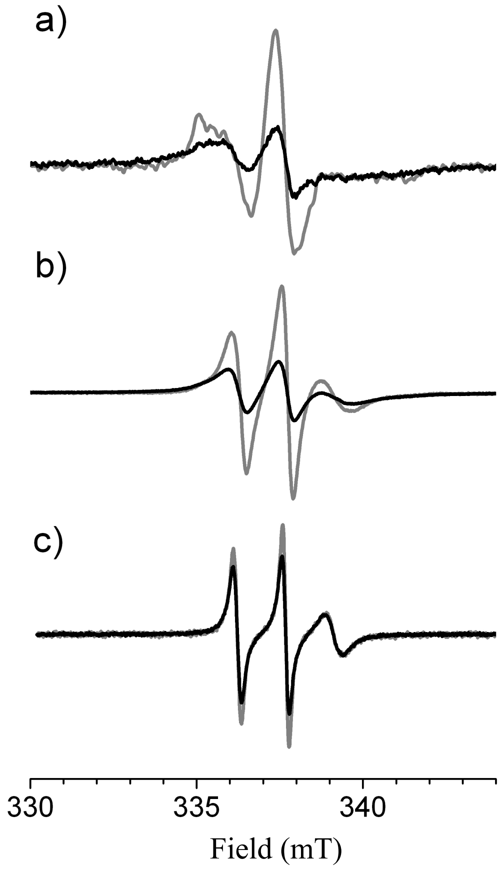

Fig. 5: The cw EPR spectra of spin-labeled WALP in DPPC below and above T_m. Pure SL-WALP (black) and dd-SL-WALP (20 %, grey) at a) T=290 K, b) T=308 K, and c) T=333 K. P/L ratio: 1/100. Spectra are normalized to the same number of spins. (For the remaining experimental parameters see "Materials and methods").

Model for the spin-spin interaction In order to interpret the measured $<\Delta\Delta B^2>$ values of the samples at 120 K, the dipolar interaction was calculated for model aggregates. For a spin pair, the $<\Delta\Delta B^2>$ value is related to the distance as

$$\left\langle \Delta\Delta B^2 \right\rangle = p\frac{1}{R^6} \tag{2}$$

where R is the spin-spin distance and $p \approx 1.56\cdot10^{-60}T^2m^6$. [17] Aggregates of more than two spins are modeled taking all pair interactions into account

$$\left\langle \Delta\Delta B^2 \right\rangle = \sum_i \left\langle \Delta\Delta B_i^2 \right\rangle = p\sum_i \frac{1}{R_i^6} \ , \tag{3}$$

where the second moments of each two-particle interaction are added. [19] The membrane is assumed to be two-dimensional, and the dipolar broadening due to line aggregates as well as two-dimensional cluster aggregates was calculated. The aggregates are modeled as having a fixed spin-spin distance R between nearest neighbors. To illustrate the procedure, a linear trimer is discussed. In this case, the central spin has two neighbors at a distance R and the spins at the ends of the aggregate have one neighbor at the distance R and one neighbor at the distance 2R, resulting in the second moment

$$\left\langle \Delta\Delta B^2 \right\rangle = p\left(\frac{1}{3}\frac{2}{R^6} + \frac{2}{3}\left(\frac{1}{R^6} + \frac{1}{(2R)^6} \right) \right). \tag{4}$$

Similarly, linear aggregates of any size up to the infinitely long line aggregate ($\left\langle \Delta\Delta B^2 \right\rangle = \frac{2\pi^6}{945}\frac{p}{R^6}$) as well as cluster aggregates can be calculated. The inter-spin distance R in the aggregates is estimated from a model in which the transmembrane helix of one WALP touches the surface of the adjacent WALP. Using a helix diameter of 1 nm, a distance between spin labels of 1 nm results, if the linker joining the spin label to the WALP-peptide backbone has the same orientation in both peptides. Since the linker length of MTSL in the extended conformation is 0.5 nm and there is no information on the rotational orientation of the WALP-helices in the membrane, we also investigated the effect of R on the broadening.

As a reference, also the second moment of non-aggregated, i.e., randomly distributed spins in the membrane is needed. The number of spins *N(r)dr* at a distance between *r* and *r* + *dr* from a spin is

$$N(r)dr = c2\pi r dr \,, \tag{5}$$

with c, the density of spins in the membrane. Introducing R_0, the distance of closest approach, a broadening of

$$\left\langle \Delta\Delta B^2 \right\rangle = p\int_{R_0}^{\infty} N(r)\frac{1}{r^6}dr = \frac{1}{2}\pi c p \frac{1}{R_0{}^4} \tag{6}$$

results. The distance of the closest approach corresponds to the helix diameter, i.e. R = R_0. To obtain an estimate of the magnitude of this broadening, the density c is calculated from the area of the headgroup of the lipids of 82 Å^2 and 52.3 Å^2 for DOPC and DPPC, respectively.[20,21] For a peptide/lipid ratio of 1/100, corresponding to an area of 50 lipid heads in the bilayer per spin, a density of c = (41 nm^2)$^{-1}$ for DOPC and (26 nm^2)$^{-1}$ for DPPC results. Only a rough estimate of this factor will be needed in the following discussion.

In Fig. 6, the results of the calculated <ΔΔB^2> values are plotted as a function of R. Broadening obtained from model calculations of linear clusters containing 2, 3, 4, 5, or an infinite number of spin-labeled peptides as well as clusters of 3, 4, and 7 peptides is shown. In order to calculate the broadening due to a random distribution for Fig. 6 an averaged density of (35 nm^2)$^{-1}$ was used. Linear aggregates yield smaller degrees of broadening than cluster aggregates, and, due to the r^{-6} dependence of the broadening, short distances dominate, such that, for example, the infinitely long line aggregate has a broadening that is close to the trimeric cluster aggregate.

In Fig. 6, also the experimental <ΔΔB^2> parameters are shown. Note that a direct comparison is only straightforward for the measurements at 120 K. For higher temperatures (partial) averaging can reduce the broadening, as discussed below. The slight deviation of the absolute values due to incomplete labeling has been neglected.

In the following, we will analyze the experimental results and compare them to the calculation to construct a picture of WALP interaction in DOPC and DPPC.

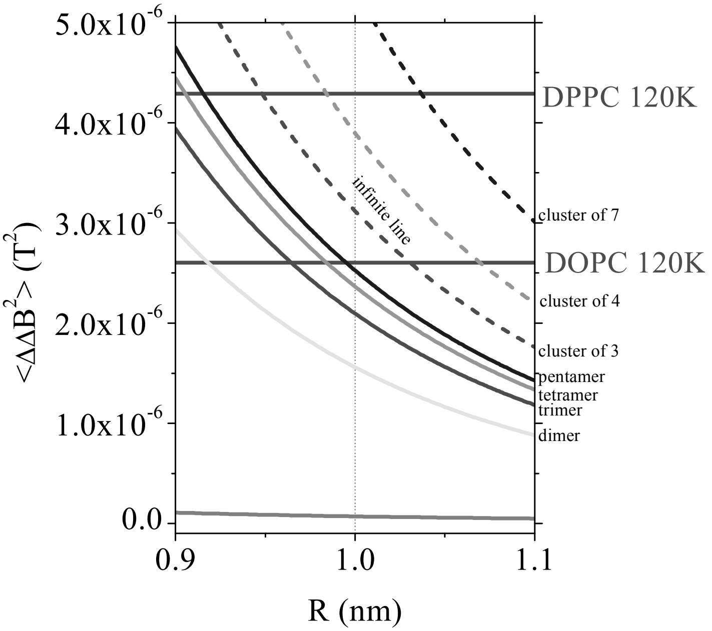

Fig. 6: The second moment (spectral broadening owing to dipolar interaction) as a function of the nearest neighbor spin distance R for different model geometries derived from calculations. Linear aggregates are shown as solid lines, in order of increasing broadening containing 2 (dimer), 3 (trimer), 4 (tetramer), 5 (pentamer), or an infinite number of spins (infinite line). Dashed lines correspond to 2D clusters containing (again in order of increasing broadening) 3, 4, or 7 molecules, respectively. The broadening for 2D randomly distributed spins as a function of closest approach (R_0) - see text - is visualized by the grey solid line. The experimentally obtained broadening values for spin labeled WALP in model membranes (P/L=1/100) at 120 K are depicted as horizontal lines: DPPC and DOPC.

4.4 Discussion

The goal of this study was to use EPR to investigate whether certain membrane conditions promote peptide-peptide aggregation. In the following we interpret the EPR spectra and develop a model for the arrangement of the peptides in the membrane.

In the gel phase of the lipids, at 120 K, the spin labels are immobilized, and the close approach of the spin labels in the pure SL-WALP causes line broadening due to the dipole-dipole interaction. The broadening is more pronounced for SL-WALP in DPPC than in DOPC, showing that the dipolar interaction is stronger for SL-WALP in DPPC than in DOPC. Model calculations (see Results) relate this broadening, expressed as the difference in second moments $<\Delta\Delta B^2>$, to the interaction of spin labels in different types of aggregates, namely cluster aggregates (Fig. 1b) and line aggregates (Fig. 1c). Given the disordered state of the membrane, such models can only be approximate, but we show that they can be used to classify the states of aggregates in a semi-quantitative way. Fig. 6 shows the results of the calculations together with the experimental values (olive and red horizontal lines). The broadening of the EPR spectra of SL-WALP in DOPC at 120 K is comparable to that of a linear aggregate containing five molecules for $R \geq 1$ nm. For SL-WALP in DPPC, $<\Delta\Delta B^2>$ is larger and at $R \geq 0.95$ nm it is in the cluster region of the diagram, close to the tetrameric cluster aggregate. This suggests that, in the gel phase of DPPC, WALP aggregates are likely of the cluster type, whereas in DOPC the aggregates are more likely to be line-type aggregates.

Line-type and cluster aggregates should also have distinct characteristics when C-and N-terminally labelled peptides are compared. For line aggregates with a strictly antiparallel (parallel) arrangement, the mixed sample should have a smaller (larger) interspin distance than the individual SL-C or SL-N-WALP samples, resulting in a larger (smaller) $<\Delta\Delta B^2>$. For cluster aggregates only very specific configurations can be envisaged that would have a strictly antiparallel arrangement of the peptides, making random orientations more likely.

For WALP in DPPC, no difference in broadening between SL-N and SL-C-WALP measured individually or combined in one sample was observed (see Results). This argues for either a line aggregate with random arrangements of the C- and N-termini of WALP, i.e., neither strictly parallel or antiparallel, or for a cluster type aggregate. The latter form would be favoured also from the amount of broadening. In DOPC, the broadening of the N- and C-terminal labelled WALP was too small to be detected. For the pure SL-C- or N-WALP samples we attribute this to the long distance between the spin labels in our constructs in the anti-parallel orientation. For the SL-C- and N-WALP mixed samples, the long distance and the overall smaller broadening in the line-aggregates, compared to the cluster aggregates, makes the broadening too small to be detected. Taking all into account, the simplest interpretation of the data so far would be cluster aggregates for WALP in the gel phase of DPPC and line aggregates for WALP in the gel phase of DOPC.

Before doing the same analysis for the liquid-crystalline phase of the lipids, first the effect of higher temperatures on the spectra has to be discussed. Above 120 K and particularly at 240 K and above, the mobility of SL-WALP in the membrane increases, and this could (partially) average the dipolar interaction. Such an averaging can only be excluded, if the correlation time of the interspin vector is long enough to fulfill the following condition: [19]

$$\tau_c\left(\left\langle\Delta\omega_0^2\right\rangle\right)^{\frac{1}{2}}=\tau_c\left(4\pi^2(2.8*10^{10}\frac{Hz}{T})^2\left\langle\Delta\Delta B_0^2\right\rangle\right)^{\frac{1}{2}}>>1 \qquad (7)$$

With the broadening $<\Delta\Delta\mathrm{B}^2>$ obtained from the frozen solution data (Table 2 and 3) this condition (Eq. 7) can be rewritten as

$$\tau_c >> \tau_c^* \ , \qquad (8)$$

with the critical correlation time τ_c^*. Assuming that the correlation time of the interspin vector corresponds to the spin-label rotational correlation time, for temperatures above 240 K one obtains the corresponding ratio to be in the range of $\frac{\tau_c}{\tau_c^*}\approx 0.4\ to\ 1.7$, i.e., far from the requirement stated in Eq. 8. Therefore the broadening could be reduced by motional narrowing.

For WALP at 290 K and 308 K in DPPC, the membrane is still in the gel phase but the spectra of dd-SL-WALP are narrowed relative to those at

120 K, revealing the increased mobility of the spin label under these conditions. Also, $<\Delta\Delta B^2>$ decreases, but it remains significantly larger than the $<\Delta\Delta B^2>$ expected for a random distribution of isolated spins in the membrane, a clear indication of aggregation. The reduction in $<\Delta\Delta B^2>$ could be caused by (partial) averaging of the dipolar interaction and/or a conversion of cluster aggregates into smaller aggregates or line-type aggregates. The difficulty to quantify the contribution of both factors to the reduction in $<\Delta\Delta B^2>$ makes it impossible to discriminate between both effects and to determine a possible change in aggregate size or shape.

In the liquid-crystalline state (T = 333 K), $<\Delta\Delta B^2>$ is much smaller than at 308 K, while the experimentally determined τ_c values are only slightly smaller than those at 308 K, where the membrane is in the gel state. The decreased broadening at temperatures above the phase transition is still significant even if one would assume a linear decrease of $(<\Delta\Delta B^2>)^{1/2}$ with τ_c. Hence, it is plausible that the dipolar interaction is not only averaged but indeed smaller, which would suggest less or no aggregation in the liquid-crystalline state of the membrane. This hypothesis is supported by the fact that the broadening increases proportionally to the peptide lipid ratio in a range between 1/100 to 1/30 (data not shown) as expected for randomly distributed spins (eq 6). For SL-WALP in DOPC $<\Delta\Delta B^2>$ follows a similar pattern as in DPPC, suggesting that also in DOPC there is aggregation below, but not above T_m. However, in DPPC the tendency to aggregate below T_m seems larger than for DOPC.

If aggregation occurs only in the gel phase, upon cooling the samples through T_m to create the gel-phase, the peptides, which are randomly distributed in the membrane in the liquid-crystalline phase, must diffuse towards each other when the membrane enters the gel phase. This requires that the peptide diffusion in the membrane must be faster than cooling through the phase transition, a condition obviously met in the cooling protocol used in the present study.

In summary, we conclude that, at 120 K, WALP aggregates in the gel phase of DPPC most likely as clusters and in DOPC as line aggregates, but not in the liquid crystalline phase of the lipids.

Previously, aggregation of WALP in the gel-phase of DPPC had been observed by atomic force microscopy (AFM). Line-type depressions were observed by AFM [1,7,8] and interpreted as linear aggregates of WALP. Striated domains are made up of parallel line depressions in which the lines are separated by 8 nm. These results suggest that the EPR parameters should only reveal linear aggregates, as the distance to an adjacent line in striated domains is too large to cause broadening according to the model used for the two-dimensional aggregates. The line aggregate model would allow for close contact of maximally four WALP peptides at the bifurcation points of line depressions, but such points should only represent a minority of the sites [1]. Fluorescence studies of the same system revealed antiparallel aggregates that, in the light of the AFM results, may also be interpreted as line aggregates. [1,9]

An obvious difference between AFM and fluorescence experiments on the one hand and the EPR experiments on the other hand is that the latter experiments are performed at significantly lower temperatures (120 K for EPR, AFM and fluorescence not below 297 K). If, upon lowering the temperature, lipid-lipid interactions become stronger, the lipids could force the peptides into cluster type aggregates as that would decrease the lipid-peptide interaction surface. This would require the peptides to give up the more favourable antiparallel arrangement possible only in the line aggregates. The smaller $<\Delta\Delta B^2>$ values at higher temperatures are consistent with a reduction in cluster size and conversion to line aggregates, but the increased mobility of the peptides at higher temperatures makes it impossible to determine that factor.

The AFM results also showed that aggregate signatures disappear upon heating the DPPC sample above the phase transition into the liquid crystalline phase [1]. Similarly, the yield of excimers decreases sharply upon heating above T_m, showing that aggregates that were present in the gel-phase, i.e. below T_m, break up in the liquid-crystalline phase.[1] The remaining excimer contribution at higher temperatures, in the order of 5 %, is likely to be too small to be detected by EPR, because in the liquid-crystalline phase partial averaging of the dipolar interaction interferes. To estimate the minimum amount of aggregated SL-WALP that could be detected in the liquid-crystalline phase under these conditions is difficult, but a minimum of 30 % seems likely. This would make it impossible to detect the amount of aggregation found in the fluorescence studies.

Our study provides the first experimental data about aggregation of WALP in the gel phase of DOPC, and our data suggests linear aggregates at 120 K. In the liquid-crystalline phase, excimer formation of WALP, suggesting dimers or higher aggregates, had been found for

P/L ratios above 1/50, [9] but also smaller amounts of aggregates were observed for P/L ratios 1/100. [1] But again, the yield of excimers found by optical methods was small (around 5 %) [1] and thus below the detection limit of EPR in the liquid crystalline phase of the membrane.

The emerging picture of aggregation of WALP in the two membranes is the following: Previously, aggregation of WALP in the gel phase of DPPC was found by AFM, optical spectroscopy and NMR [1,7]. Our observations of SL-WALP at 120 K agree with these results, although our interpretation suggests cluster rather than line aggregates. We propose that at the temperature of the EPR experiments cluster aggregates prevail, because lipid-lipid interactions become stronger at lower temperatures. Even though the peptide-peptide interaction seems to favour an antiparallel arrangement of the peptides, [9,14] this energy gain could be offset by the increasingly unfavourable lipid-peptide interaction. Under these circumstances, cluster aggregates that minimize the lipid-peptide interface could be the optimal solution.

Aggregation in the gel phase of DOPC had not been reported before. The aggregation of the peptides in DPPC was attributed to the balance of lipid-lipid and lipid-peptide interactions in the gel phase of the saturated lipid DPPC, particularly, by the increased ordering of the lipid chains in the vicinity of WALP found by NMR. [1] Aggregation in the gel phase of DOPC indicates that the lipid order in the gel phase is sufficient to induce aggregation of WALP, even though this ordering is expected to be compromised by the unsaturated lipid chains of DOPC, or, in other words that the gel phase is more important than the precise structure of the lipid in the vicinity of WALP.

4.5 Conclusion

The approach to combine EPR line broadening, diamagnetic dilution and model calculations provides information on aggregate shape and, in certain cases, also the size of the aggregates. This approach should be applicable to a wide range of membrane conditions.

The higher degree of order of the lipid chains in the gel phase seems to be a major factor in promoting aggregation because both the saturated lipid DPPC and the unsaturated lipid DOPC promote WALP aggregation in that phase. However, the degree of saturation of the lipids seems to affect the type of aggregation and our analysis suggests cluster aggregates in DPPC and line aggregates in DOPC. The strength of lipid-peptide interactions may also depend on temperature. In DPPC, EPR at 120 K indicates cluster aggregates, whereas AFM at 297 K reveals line aggregates.

The degree of aggregation must be significantly smaller in the liquid-crystalline phase of both lipids, but experimental limitations in the fluid, mobile regime of the membrane limit the sensitivity and uniqueness of the answers obtained. Such limitations can, in principle, be overcome by a quantitative analysis of the peptide mobility in the membrane.

The EPR approach presented is suitable to investigate the state of peptides in membrane. It should be applicable to a wide range of membrane conditions. We demonstrate it for the gel-phase of two lipids. In view of the occurrence of gel-phase like states in biological membranes, this presents a relevant step ahead in the study of lipid-peptide interaction.

Acknowledgments

I would like to thank dr. Malte Drescher for his active role in this project. He performed the EPR measurements of part of the samples and developed the aggregation model, dr. prof. Antoinette Killian, Andrea Holt for the help in the preparation of the lipid samples and the useful suggestions and Tania Meijneke who prepared the peptide samples.

Reference list

1. Sparr, E.; Ganchev, D. N.; Snel, M. M. E.; Ridder, A. N. J. A.; Kroon-Batenburg, L. M. J.; Chupin, V.; Rijkers, D. T. S.; Killian, J. A.; de Kruijff, B. *Biochemistry* **2005,** *44*, 2-10.
2. Killian, J. A.; Nyholm, T. K. M. *Current Opinion in Structural Biology* **2006,** *16*, 473-479.
3. Ozdirekcan, S.; Etchebest, C.; Killian, J. A.; Fuchs, P. F. J. *Journal of the American Chemical Society* **2007,** *129*, 15174-15181.
4. Lemaitre, V.; de Planque, M. R. R.; Howes, A. P.; Smith, M. E.; Dupree, R.; Watts, A. *Journal of the American Chemical Society* **2004,** *126*, 15320-15321.
5. Holt, A.; de Almeida, R. F. M.; Nyholm, T. K. M.; Loura, L. M. S.; Daily, A. E.; Staffhorst, R. W. H. M.; Rijkers, D. T. S.; Koeppe, R. E.; Prieto, M.; Killian, J. A. *Biochemistry* **2008,** *47*, 2638-2649.
6. Nielsen, R. D.; Che, K. P.; Gelb, M. H.; Robinson, B. H. *Journal of the American Chemical Society* **2005,** *127*, 6430-6442.
7. Rinia, H. A.; Kik, R. A.; Demel, R. A.; Snel, M. M. E.; Killian, J. A.; van der Eerden, J. P. J. M.; de Kruijff, B. *Biochemistry* **2000,** *39*, 5852-5858.
8. de Kruijff, B.; Killian, J. A.; Ganchev, D. N.; Rinia, H. A.; Sparr, E. *Biological Chemistry* **2006,** *387*, 235-241.
9. Sparr, E.; Ash, W. L.; Nazarov, P. V.; Rijkers, D. T. S.; Hemminga, M. A.; Tieleman, D. P.; Killian, J. A. *Journal of Biological Chemistry* **2005,** *280*, 39324-39331.
10. de Planque, M. R. R.; Greathouse, D. V.; Koeppe, R. E.; Schafer, H.; Marsh, D.; Killian, J. A. *Biochemistry* **1998,** *37*, 9333-9345.
11. Bashtovyy, D.; Marsh, D.; Hemminga, M. A.; Pali, T. *Protein Science* **2001,** *10*, 979-987.
12. Margittai, M.; Langen, R. *Amyloid, Prions, and Other Protein Aggregates, Pt C* **2006,** *413*, 122-139.
13. Der-Sarkissian, A.; Jao, C. C.; Chen, J.; Langen, R. *Journal of Biological Chemistry* **2003,** *278*, 37530-37535.
14. Yano, Y.; Matsuzaki, K. *Biochemistry* **2006,** *45*, 3370-3378.

15. Stoll, S.; Schweiger, A. *Journal of Magnetic Resonance* **2006,** *178*, 42-55.
16. Steigmiller, S.; Borsch, M.; Graber, P.; Huber, M. *Biochimica et Biophysica Acta-Bioenergetics* **2005,** *1708*, 143-153.
17. Steinhoff, H. J. *Frontiers in Bioscience* **2002,** *7*, C97-C110.
18. John Wiley & Sons *Lipid-Protein Interactions;* New York, 1982.
19. Abragam, A. *The Principles of Nuclear Magnetism;* Oxford University Press: Oxford, 1961.
20. Nagle, J. F.; Tristram-Nagle, S. *Biochimica et Biophysica Acta-Reviews on Biomembranes* **2000,** *1469*, 159-195.
21. Lis, L. J.; Mcalister, M.; Fuller, N.; Rand, R. P.; Parsegian, V. A. *Biophysical Journal* **1982,** *37*, 657-665.

Chapter 5. The RIDME pulse sequence as an effective tool for measurements of electron-electron distances involving paramagnetic centers with strong spectral anisotropy

5.1 Introduction

Pulsed EPR has taken a leap forward as a method for structure determination in disordered chemical and biological systems ever since pulsed EPR methods had been developed that directly and selectively probe the dipolar interaction between electron spins [1-3]. Amongst them are 2+1 methods and DEER [4-6], solid-echo type single-frequency techniques for refocusing dipolar couplings (SIFTER) [7], and double quantum coherence methods (DQM) [5,6,8]. These techniques are optimized for systems with low spectral anisotropy, such as nitroxide-type spin labels and organic radicals, and require the excitation of a significant part of the spectrum. The spectral widths of the EPR transitions of nitroxides and organic radicals are in the order of several mT at the conventional operating frequency of 9 GHz (X-band EPR), which compares well with presently available excitation bandwidths of a few mT (e.g. a pulse length of 24 ns results in 1.5 mT bandwidth). For even the most benign transition metal ion, Cu(II), the spectral width is already about 70 mT. The resulting fractional excitation of the spectrum either severely limits the sensitivity or makes the application of the method impossible. Therefore, novel approaches to address such paramagnetic centers are sought. The present account describes a method tailored to determine the interaction between a low g-anisotropy center and a center of large g-anisotropy and is ideally suited to address the distance between a nitroxide spin label and a paramagnetic transition-metal ion. For structure determination this combination is most relevant, because transition-metal centers are often present in proteins. Another advantage of such centers is that they are firmly anchored in the protein and therefore are not fraught with the problem of flexible linkers as the commonly used spin labels. Previously, most approaches to measure such distances made use of the change in relaxation properties of the small g-anisotropy center caused by the transition-metal ion, as discussed in several reviews [9-11]. The complexity of relaxation-based approaches from the point of view of experiment and interpretation has so far limited the applications.

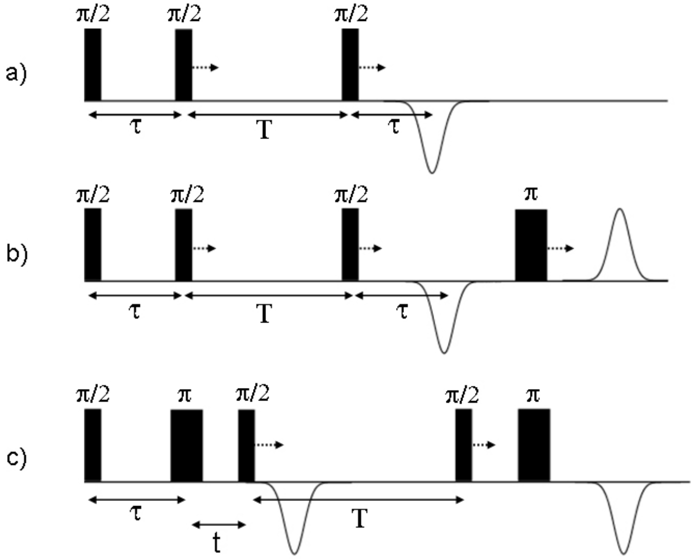

Fig. 1: Pulse sequences for RIDME experiment: (a) three-pulse RIDME and (b) four-pulse RIDME, time τ is incremented; (c) five-pulse RIDME, time t is incremented and echo is detected as a function of t- τ.

The method proposed directly probes the dipolar interaction between the metal center and the nitroxide. It is based on the relaxation induced dipolar modulation (RIDME) method suggested by Kulik et al [12], in which the change is detected in the resonance frequency of the observed spin, i.e. the nitroxide (A-spins), by the spontaneous flip of the electron spin on the partner paramagnetic center (B-spins). Here the flip of the B-spins is not induced by a pump-pulse as in traditional sequences, but is left to the longitudinal relaxation of the B-spins. As a consequence, there is no need to flip the B-spins by a pump pulse, avoiding the problem of the limited excitation bandwidth. The RIDME sequence as proposed originally [12] (Fig. 1 a) and the four-pulse version suggested subsequently [13], suffer from a dead-time problem that severely limits the usefulness of these methods for distance determination involving systems with high g-anisotropy, as we will demonstrate.

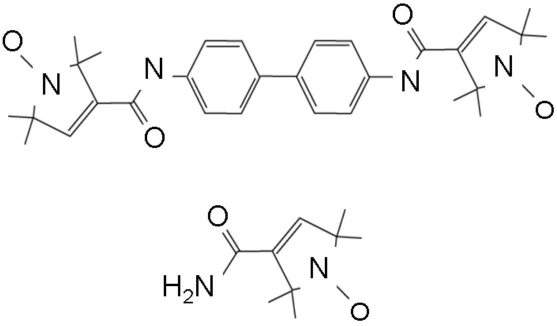

Fig. 2: Chemical structures of the biradical PH2 and the monoradical PH0

We propose a five-pulse version of the RIDME sequence that completely eliminates the dead-time. We demonstrate that the sequence works and that it yields the expected distances on a nitroxide biradical (PH2, see Fig. 2) by comparing the results of the new RIDME sequence and a conventional DEER experiment. Subsequently, we apply the new sequence to measure the distance between the low-spin iron(III) center, a paramagnetic center with large g-anisotropy, and a nitroxide spin label in cytochrome *f* (cyt *f*). This protein is part of the electron transfer chain in photosynthesis and contains an intrinsic low-spin Fe(III) center. By site-directed mutagenesis, a cystein was introduced and at position 104 and a spin label was attached. resulting in a system with a nitroxide-Fe(III) distance in the order of 1.43 nm. We show that in spite of the large g-anisotropy of the Fe(III) center, the distance between the two paramagnetic centers can be determined. A Gaussian distance distribution centered at 1.67 nm with a width of 0.22 nm is obtained. Presently, there is no other method to determine distances in such cases with similar accuracy.

5.2 Materials and Methods

5.2.1 Sample preparation

The pEAF-wt [14] expression plasmid containing the sequence encoding the soluble domain of cyt *f* from *Nostoc* sp. PCC7119 has been kindly provided by the group of Prof. Miguel De la Rosa, Instituto de Bioquímica Vegetal y Fotosíntesis, Universidad de Sevilla, Spain. In order to prepare the single-cysteine Cyt *f* variants Q104C and N71C, mutations were introduced by site-directed mutagenesis using the Quik Change^{TM} polymerase chain reaction protocol (Stragene, La Jolla, CA) with the plasmid pEAF-wt as a template. To introduce a cysteine instead of the asparagines at the position 71 the direct primer GGCTC**C**AAGGTCGGCTTA***TG***CGTCGGTGCTG (31 bases) was designed from the nucleotide sequence, inserting at the same time the Sty I restriction site next to the *5'* end of the leader of this primer. Analogously, to introduce a cysteine instead of the glutamine at the position 104 the direct primer CGGCGATGTTTACTTC***TGC***CCCTACGGCGAAG (32 bases) was designed, inserting an extra Bgl I restriction site with respect to the *wild type*. Both constructs were verified by DNA sequencing.

To improve the maturation and correct insertion of the heme group, *E. coli* strain MV1190 cells (Bio-Rad) were co-transformed with plasmids pEC86 [14] and the Cyt *f* expression plasmids. The cells were incubated on Luria-Bertani (LB) medium plates (added by 20 mg/L ampicillin, 20 mg/L chloramphenicol) at 37º C for 24 hours. Several pre-cultures were incubated in 100 mL flasks with 20 mL of LB medium supplemented with 20 mg/L ampicillin (amp) and 20 mg/L chloramphenicol (cam) at 37º C and 250 rpm for 5-6 hours. The pre-cultures with the best OD_{600} were used to inoculate 1.7 L (in 5 L Erlenmeyer flasks) in the same medium and incubated at 25º C and 150 rpm for >72 h under semianaerobic conditions and high antibiotics pressure by adding further amp and cam after 20 h and 40 h. Induction was achieved 20 h after the inoculation of the large culture using 1mM IPTG. More than 80 h from the induction the cultures appeared brown for the presence of the cyt; the cells were harvested by centrifugation and the periplasmic fraction was extracted by osmotic shock. The pink water fraction was dialyzed against 2 L of 5 mM Tris-HCl buffer, pH 8 and 3 mM dithiothreitol (DDT). The yield in the periplasmatic fraction was 10 mg/L of protein for N71C and 5 mg/L of Q104C. The resulting dialysate was cleared by centrifugation and loaded onto a DEAE column equilibrated with 5 mM Tris-HCl buffer, pH 8 and 3 mM DDT. Elution has been performed with a gradient of 20–500 mM NaCl and 3 mM DTT. The fractions containing the cyt *f* were concentrated and loaded onto a gel-filtration (G75 Superdex) column and eluted with 5 mM Tris-HCl buffer pH 8, 3mM DTT and 150 mM NaCl. The fractions containing the protein were pooled, concentrated, dialysed against 5 mM Mes pH 6 and 3 mM DTT and loaded onto a DEAE column equilibrate with 5 mM Mes pH 6 and 3 mM DTT. The protein was eluted with a gradient 0-500 mM NaCl and tested for its purity using the A_{280}/A_{556} ratio. The pure fractions show an A_{280}/A_{556} value of 1.3 under reducing conditions.

Before adding the spin label the excess of DTT has been removed from the purified cyt *f* cysteine mutant solution, by several concentration/redilution cycles with degassed 10 mM Na phosphate at pH 6. To avoid reduction of the disulfide by the Fe(II) and concomitant loss of the spin label, a 100 fold excess of $K_3[Fe(CN)_6]$ was added to the solution before adding a 10 fold excess of MTSL [(1-Oxyl-2,2,5,5,-tetramethyl-3-pyrroline-3-m3thyl)-methanethiosulfonate] (purchased from Toronto Research Chemicals, Ont., Canada). The solution was left for 2h at room temperature and overnight at 4° C; the excess of $K_3[Fe(CN)_6]$ and MTSL was removed by several concentration/redilution cycles with degassed 10 mM Na phosphate at pH 6.

5.2.2 EPR experiments

All measurements were done on a Bruker E680 ElexSys spectrometer equipped with an ER 4118X-MS3 split-ring resonator of the FlexLine series and an Oxford cryostat. Initial pulse positions for five-pulse RIDME sequence were 0, 500 ns, 960 ns, *T*+960 ns, *T*+X (for *T* values see text below), X was 2000 ns for nitroxide biradical and 1800 ns for spin labeled cyt *f*. Detector integration gate was 20 ns. Positions of the third and the fourth pulses were incremented with a step of 4 ns, while positions of the other pulses as well as the detection gate were not changed.

All experiments on nitroxide solutions were done at 40K with a repetition time of 10 ms. Pulse lengths for the RIDME experiments were 24 ns and 48 ns for $\frac{\pi}{2}$- and π-pulses, respectively, to compromise between broad excitation bandwidth required to cover spectrally dipolar doublets and sufficiently narrow bandwidth needed to escape simultaneous excitation of both spins in the radical couple. All RIDME measurements were done at magnetic field value of 332.75 mT and microwave frequency of 9.372 GHz.

DEER measurements were done using 9.332 GHz observer frequency with initial observer pulse positions 0, 500 ns, 1400 ns. Pump pulse of frequency 9.397 GHz was initially positioned at 400 ns and swept with a step of 4 ns. The RIDME traces of PH2 are obtained by dividing a trace with T = 400 μs by one with T = 10 μs. The value of the external magnetic field for DEER was 331.3 mT.

All experiments were done at 7 K with a repetition time of approximately 1 s and 2 shots per loop. Applied pulse lengths of 12 ns and 24 ns for $\frac{\pi}{2}$- and π-pulses respectively were shortest achievable on our spectrometer. The RIDME traces of both systems (Q104C and N71C) were obtained by dividing a trace with T = 200 μs by one with T = 5 μs. The microwave frequency and magnetic field value were 9.306 GHz and 330.45 mT respectively.

5.2.3 Numerical calculation

All numerical calculations were done using the R2006b version of the MATLAB software. To calculate Pake distributions and the corresponding dipolar traces, we assumed the orientation distributions for the g-tensor and the inter-radical vector to be isotropic and mutually independent. To avoid numerical singularities for the Pake distributions, we assumed an intrinsic Gaussian line width of 1 MHz.

5.3 Results and Discussion

In the following we first describe the background relevant to the method and introduce the new pulse sequence. Then we report measurements of the nitroxide-nitroxide distance in PH2 and of the distance between a nitroxide spin label and the low-spin Fe(III)-center in the cyt *f* mutant.

5.3.1 Background of the method, dipolar interaction between two electron spins

The dipole-dipole interaction between two unpaired electrons is described by the Hamiltonian [15]

$$H_{dd} = \frac{1}{r^3}\left[\left(\vec{\mu}_1 \cdot \vec{\mu}_2\right) - 3\frac{\left(\vec{\mu}_1 \cdot \vec{r}\right)\left(\vec{\mu}_2 \cdot \vec{r}\right)}{r^2}\right]$$

For two interacting S=1/2 spins in the point-dipole approximation, the strength of the interaction in frequency units is given by

$$\omega_{dd} = \frac{\mu_0 g_1 g_2 \beta_e^2}{4\pi\hbar}\frac{1}{r^3}\left(3\cos^2\theta - 1\right)$$

Here g_1 and g_2 are the g values of the two interacting spins, r is the distance between them, and θ is the angle between the external magnetic field and the vector connecting the radicals. Typically, for organic radicals such as nitroxides, the g anisotropy is very small and one simply assumes $g_1 = g_2 = g_e = 2$. In this case, from the angular dependence of ω_{dd} a Pake pattern results [16] with two symmetric sharp peaks at

$$\omega_{dd}^{\perp} = \pm\frac{\mu_0 \beta_e^2}{\pi\hbar}\frac{1}{r^3}$$

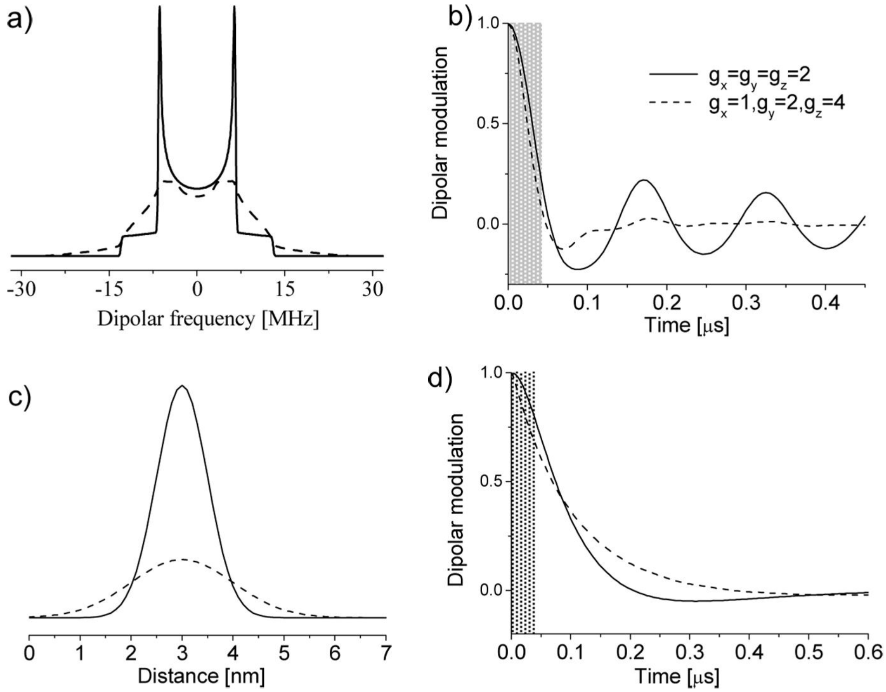

Fig. 3: (a) Pake patterns for isotropic g-tensor: solid line, and for rhombic g-tensor with $g_x = 1$ $g_y = 2$ $g_z = 4$: dashed line; (b) Corresponding dipolar modulations; (c) two Gaussian distance distribution functions with corresponding dipolar traces in case of g-tensor anisotropy with $g_x = 1$ $g_y = 2$ $g_z = 4$. Shadowed bars on figures (b) and (d) indicate the dead time areas of the four-pulse RIDME sequence.

The numerically calculated Pake pattern for an inter-radical distance of 2 nm is shown in Fig. 3 a (solid line). It has two sharp peaks at $\upsilon_{dd}^{\perp} = \pm$ 6.3 MHz. In the time domain, a slowly decaying modulation of the dipolar trace results (solid line, Fig.3 b). For the coupling between an isotropic spin with g = 2 and a spin with a large g anisotropy (principal values: $g_x = 1, g_y = 2, g_z = 4$), the dashed line in Fig. 3 a is obtained The larger g anisotropy causes a broadening of the Pake pattern. In the time domain (Fig. 3 b, dashed line) the initial part of the modulation up until approx. 60 ns is similar to the isotropic case, but all subsequent modulations are absent.

5.3.2 The standard RIDME sequence

The pulse sequence for the RIDME experiment is the stimulated echo sequence shown in Fig. 1 a. A full analytical description of the method is given in [12]. Here we illustrate the idea of the method with a vector model. The initial magnetization vector in the rotating frame is $\{0,0,-M_0\}$. After the first $\frac{\pi}{2}$-pulse, which as all following pulses is applied along the x-axis, the magnetization becomes $\{0,-M_0,0\}$. After a time τ of free evolution the vector is given by $\{-M_0 \sin \Omega\tau, -M_0 \cos \Omega\tau, 0\}$, where Ω is the off-resonance frequency of the spin packet. The second $\frac{\pi}{2}$-pulse transforms the magnetization vector into $\{-M_0 \sin \Omega\tau, 0, M_0 \cos \Omega\tau\}$. Under free evolution for a time T that is much larger than the transverse relaxation time T_2, only the z-component survives, resulting in $\{0,0,M_0 \cos \Omega\tau\}$. The immediate result of the third $\frac{\pi}{2}$-pulse is the magnetization vector $\{0,M_0 \cos \Omega\tau,0\}$, which can be presented as the sum of two vectors: $\left\{-\frac{M_0}{2} \sin \Omega\tau, \frac{M_0}{2} \cos \Omega\tau, 0\right\}$ and $\left\{\frac{M_0}{2} \sin \Omega\tau, \frac{M_0}{2} \cos \Omega\tau, 0\right\}$. The first vector is refocused after a time τ of free evolution resulting in a stimulated echo. The second vector continues defocusing, but it can be refocused by the application of an additional π-pulse resulting in a virtual echo [17]. If during the time T a B-spin, i.e. a spin that has a dipolar interaction with the observed A-spin, flips, the frequency of the A-spin shifts by ω_{dd}, resulting in a modulation of the amplitude for both the stimulated and the virtual echo. By incrementing the time τ in the sequence, this is detected as a cosine function of $\omega_{dd}\tau$. The probability of the flip of the B-spins during the time T is given by

$$\frac{1}{2}\left(1-exp\left\{-\frac{T}{T_1}\right\}\right) \tag{1}$$

where T_1 is the longitudinal relaxation time of the B-spin. Consequently, T has to be in the order of T_1 and the modulation depth, given by (1), is maximally 0.5 of the echo amplitude.

This simple three-pulse RIDME sequence, however, suffers from the dead time problem, i.e., τ cannot be made infinitely small. The experimental inaccessibility of the short τ values, in this case, has two origins. First, resonator ringing prevents echo detection immediately after the third pulse. Second, at τ values comparable with the pulse widths, partial or complete overlap of the first and the second pulse causes distortions of the RIDME trace in exactly the same way as in the basic, three-pulse version of the DEER sequence. The previously proposed four-pulse modification of RIDME with an additional refocusing π-pulse, as shown on Fig.1 b, removes the resonator ringing problem, and reduces the dead time to about 40 ns [13]. Still, the remaining dead time seriously limits the application of the RIDME method to systems where at least one of the coupled spins has a large spectral anisotropy, as discussed in the following.

5.3.3 Consequences of the dead time for systems with large g-anisotropy

In Fig. 3 b, the effect of a large g-anisotropy on the time trace is shown. Whereas for systems with small g-anisotropy the information about the distance between the coupled spins can be obtained even without taking into account the initial part of the trace, for systems with large g-anisotropy the shape of the function (Fig. 3 b, dashed line) cannot be reconstructed without measuring the initial part of the trace. This part of the trace is lost in the shaded area that shows the minimal dead time achievable by the traditional RIDME sequences. Fig. 3 c and d show the effect of a distribution of distances and the time domain data (Fig. 3 d). Distinct time domain traces are obtained, from which the distance distributions can be reconstructed provided that the full trace can be determined experimentally.

5.3.4 Pulse sequence for dead-time free, five-pulse RIDME

In order to remove the residual dead time an additional π-pulse is introduced into the four-pulse RIDME sequence [12] using a similar approach as was done to develop the four-pulse DEER sequence [18]. The resulting five-pulse RIDME sequence is shown in Fig. 1 c. For the detection, one can use either the refocused stimulated or the refocused virtual echo, since both of them are modulated in the same way. In our hands, detection on the refocused virtual echo worked best. The amplitude of this echo is measured as a function of the time delay between the third pulse and the primary echo created by the first two pulses. The positions of the third and the fourth pulse are simultaneously incremented by the same time steps, keeping the time T between them constant. The positions of the first, second and the fifth pulse are kept fixed in time. The total phase-evolution time is constant, avoiding unwanted contributions of T_2 relaxation to the trace.

Although the dead time is eliminated in the same way as in the DEER experiment there is one difference to be considered. At t values close to zero, three echoes, namely the refocused stimulated, the refocused virtual and the echo created by the last two pulses of the sequence overlap in time. This distorts the trace at initial times. To remove this problem, phase cycling is required. We use the 8-step phase cycle outlined in table 1. According to the vector model, the amplitudes of the three echoes depend on the phases of the third (φ_3) and fourth (φ_4) pulse. The refocused virtual echo depends on $e^{i(\varphi_4-\varphi_3)}$, the refocused stimulated echo on $e^{i(\varphi_3+\varphi_4)}$ and the two-pulse echo of the last two pulses in the sequence on $e^{i\varphi_4}$. In principle, the phase cycle $\left[(+x)+(-x)+(+y)+(-y)\right]$ on the third and the fourth pulse would be sufficient to eliminate the unwanted echoes. However, if the time T is long, the two refocused echoes can be much smaller in amplitude than the primary echo. In this case, imperfections in the microwave-channel phase adjustment may prevent complete cancellation of the unwanted two-pulse echo. Therefore, an additional two-step phase cycle $\left[(+x)-(-x)\right]$ is applied to the first pulse, to remove remaining distortions from the time trace.

Table 1
Phase cycle used for the 5 pulse RIDME sequence

φ_1	φ_3	φ_4	Detection
+x	+x	+x	+
+x	-x	-x	+
+x	+y	+y	+
+x	-y	-y	+
-x	+x	+x	-
-x	-x	-x	-
-x	+y	+y	-
-x	-y	-y	-

5.3.5 Suppression of unwanted contribution to the RIDME trace

Additionally to the dipolar modulations, nuclear modulations and spectral diffusion can contribute to the RIDME traces at temperatures below 70 K. The latter two contributions can be eliminated most reliably by dividing the measured trace by a reference trace of a sample containing only A spins. But even if such a sample is not available, the unwanted contributions can be largely suppressed. As was shown before [19], nuclear modulations can be suppressed by dividing two traces, one with sufficiently long T , where dipolar contribution is substantial, and the other with a much shorter T (T_S) that is still long compared with T_2 . In that case, the nuclear modulations should be similar to those in the first trace thus removing the major part of the nuclear modulations. In other words, terms independent of T would cancel each other and terms depending on T would decay owing to the loss of nuclear coherence. This procedure, however, does not remove the second unwanted contribution, the spectral diffusion in the time interval T . Spectral diffusion causes a monotonous decay of the RIDME trace, even though the total echo-refocusing path remains the same. The best experimental conditions for separation of the spectral diffusion component from the dipolar modulations would be to find a parameter T long enough to flip a large fraction of the partner spins but still short enough to avoid spectral diffusion. In practice, at least for the experiments discussed here, spectral diffusion components are sufficiently distinct from dipolar modulations that they can be empirically fitted and subtracted.

5.3.6 Results for the nitroxide biradical

To test the new pulse sequence we used the nitroxide biradical PH2 (Fig. 2), because in this system the distance is well-defined and regular DEER experiments can be performed to verify the RIDME results. In Fig. 4 b, the DEER result is shown, revealing the regular modulation pattern in the time trace. For RIDME, the system is not ideal, because the paramagnetic centers, and in particular their T_1 times, are identical. This is not desired, since significant modulation depths can only be obtained if the time T of the RIDME sequence is comparable to or longer than T_1 of the B-spins. Here, however, the A-spins have the same T_1, making it impossible to detect their signal after such a long T time. Nevertheless, RIDME traces can be obtained as shown in Fig. 4 c, solid line. Owing to the small modulation depth for RIDME, nuclear modulations of protons appear alongside the desired electron-electron dipolar modulations. To eliminate the nuclear modulations, the RIDME trace for the PH0 monoradical (dashed line on Fig.4 c) was measured, revealing only nuclear-modulation and spectral-diffusion components. Division of the trace for PH2 by the one for PH0 results in the trace shown in Fig. 4 d, in which nuclear modulations and the overall decay of the trace, which is due to spectral diffusion, are absent. The trace is in agreement with the DEER trace, Fig. 4 b, showing that the RIDME modulations obtained with the new sequence are indeed caused by the electron-electron spin interaction. The modulation depth is in the order of 15 %, i.e., significantly lower than the theoretical maximum of 50 %. Given that T is 400 μs and that the T_1 of nitroxides at this temperature is in the ms range, the conditions are far from ideal for efficient RIDME (Eq. 1), which explains the low modulation depth. The dashed line in Fig. 4 d shows the fit of the dipolar trace using DeerAnalysis2006 [20-22] with a Gaussian distance distribution at 1.89 nm and 0.14 nm standard deviation. Faithful reproduction of the experimental curves including the early times confirms that the new RIDME sequence abolishes the dead time and results in the proper shape of the early parts of the curve. The DEER trace, obtained with the same pulse lengths for the observer pulses as the RIDME trace (Fig. 4 b) was fitted with parameters of 1.89 nm, and a standard deviation of 0.08 nm. We attribute the smaller width of the distribution in the latter case to orientation selection in that combination of pump and observer pulses.

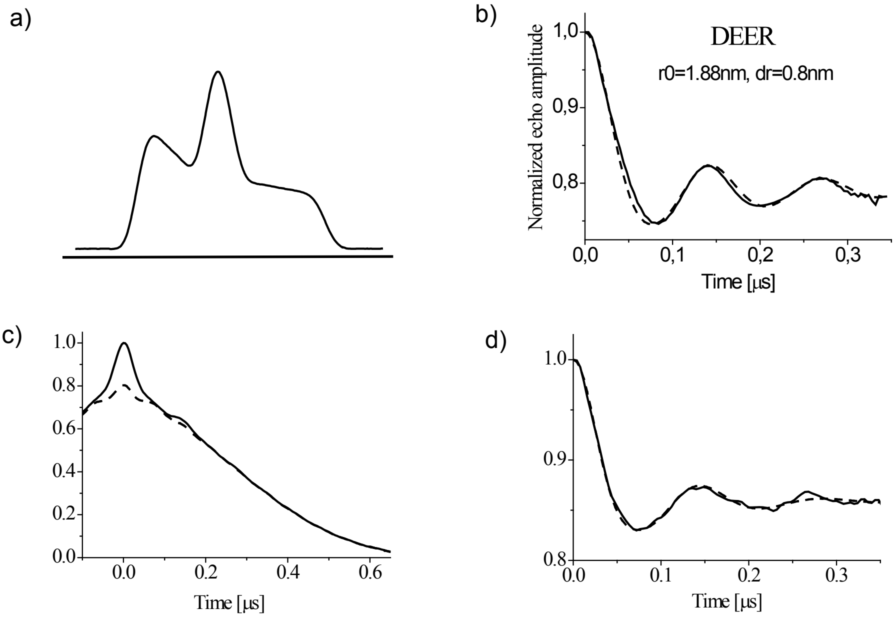

Fig. 4: Experimental data obtained for PH2 biradical. (a) Two-pulse echo detected spectrum with two arrows indicating observer spins excited in both DEER and RIDME; (b) DEER trace: solid line and best fit: dashed line; (c) five pulse RIDME trace for PH2 biradical: solid line, for PH0 monoradical: dashed line, obtained as described in text; (d) extracted from RIDME traces dipolar modulations: solid line, and its best fit: dashed line.

5.3.7 Results for spin labelled Cytochrome *f*

The new pulse sequence has been developed for the correlation of a transition metal ion and a spin label, which we demonstrate for the protein cyt *f* (Q104C), where the spin label interacts with a low-spin Fe(III) center. The RIDME trace for Q104C is shown in Fig. 5 a. At times longer than 70 ns, the trace is dominated by the background, which is fitted as a stretched exponential (see Fig. 5 a) and subtracted (Fig. 5 b). A fast initial decay is observed, but further modulations, as seen in the traces in Fig. 4 b at times larger than 100 ns, are absent. The dotted line in Fig. 5 b shows the fit to the data with low-spin Fe(III) g-values of $g_x = 0.9$, $g_y = 1.69$, $g_z = 3.51$ [23], and a Gaussian distance distribution centered at 1.67 nm with a standard deviation of 0.22 nm. The parameters of the distance distribution are only marginally affected by the uncertainty of the g_x value, resulting in variations of about 0.04 nm in the distance and the width for $g_x = 0.4$, 0.9 or 1.4.

In Fig. 5 c, the dependence of the modulation depth on T is shown. For data obtained by dividing a trace with a long T by one with a short T (T_S) (see above) the dependence can be described by a bi-exponential curve according to

$$A = A_0\left[P\left(e^{-\frac{T_S}{T_1^a}} - e^{-\frac{T}{T_1^a}}\right) + (1-P)\left(e^{-\frac{T_S}{T_1^b}} - e^{-\frac{T}{T_1^b}}\right)\right] \tag{2}$$

In the present case, $T_S = 5$ µs, and T_1^a and T_1^b are the relaxation times of the fast relaxing center. The fraction P refers to the amount of spins relaxing with a time T_1^a and A_0 is the modulation depth obtained for an optimal choice of T and T_S. For T_1^a and T_1^b we obtained 13 µs and 148 µs, respectively, which is in good agreement with the values for low-spin iron hemes at this temperature [24]. We attribute the presence of two T_1 times with approximately equal weight (P = 0.57) to the anisotropy of the low-spin Fe(III) relaxation times. There is no literature about the anisotropy of T_1 of the low-spin Fe(III), nevertheless a similar anisotropy of T_1 has been found for nitroxide-radical centers [25]. Also, preliminary measurements on a second mutant (cyt *f* N71C) yielded similar parameters in eq. 2, emphasizing that the low-spin Fe(III) center is the source of the modulation. The amplitude $A_0 = 0.24$ for Q104C is about half the maximal modulation depth for RIDME, which, according to eq. 1 is 0.5. The smaller depth found agrees with the fraction of oxidized iron in our samples, which is 56% as determined by optical spectroscopy. Taking this correction into account we conclude that A_0 is 86% of the theoretical maximum. This high value also shows that possible distortions due to limited bandwidth of the microwave pulses for such short distances are not significant.

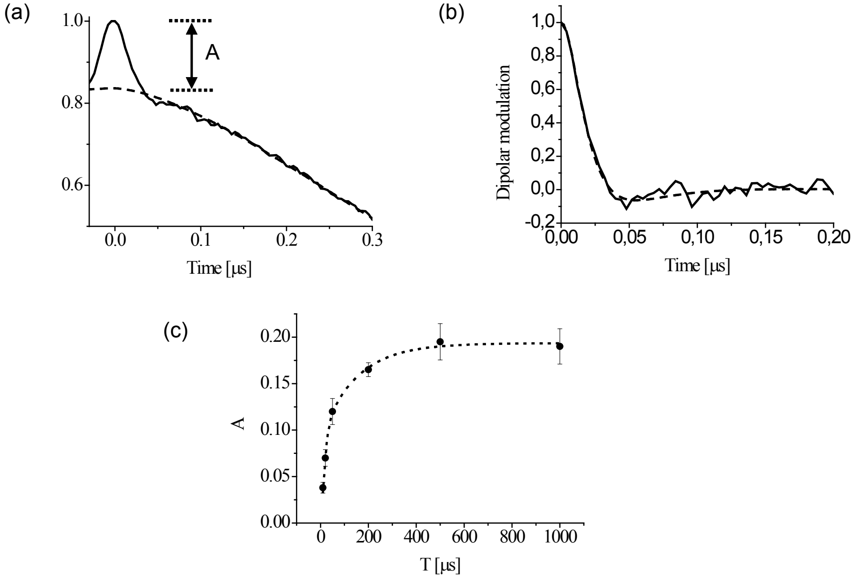

Fig. 5: Results for Q104 mutant of Cytochrome *f*. (a) Experimental five-pulse RIDME trace (solid line) obtained as described in the text and stretched exponential fit of the background (dashed line); (b) extracted dipolar modulation contribution (solid line) and its best fit (dashed line); (c) Modulation amplitude defined as shown on (a) versus time T (points) and the best fit (dashed line)

In Table 2, the parameters of the distance distribution are compared to the distance between the iron and the C_β atoms (Fe- C_β) derived from the X-ray structure of cyt *f*. Given the length of 0.5 - 0.6 nm [8] for the spin-label linker, between the C_β-atom and the center of spin density on the nitroxide, the distance found for Q104C agrees well with the C_β distance obtained from the crystallography. Additionally, the conformation of the spin-label linker was modeled [26,27], resulting in the distance distribution shown in Fig. 6.

The model collects all sterically allowed orientations of the spin label and neglects any attractive interactions between protein and spin label. Therefore model-derived distributions are expected to be broader than the real ones. Taking this into account, the distance distribution found by RIDME is in good agreement with the distance of the paramagnetic centers predicted from the model.

Table 2

Distance for cyt *f* mutant Q104 and crystal structure parameters

sample	**distance** nm	σ_r	**C-beta Fe** nm[a]
Q104C	1.67±0.03	0.22±0.08	1.43

[a]From X-ray crystallography, structure PDB-entry 1TU2

The width of the distance distribution of Q104C is 0.22 nm, which is smaller than the distance distributions found for the distances between two spin labels linked to a single protein (between 0.24 and 0.45 nm [27]). This is reasonable in view of the fact that the distribution is dominated by the spread in spin-label linker conformations and that in the present case only one such distribution is to be considered. An odd dichotomy arises. The distance determined between a spin label and a metal center should be more accurate because only one spin-label linker conformation affects the distance distribution. On the other hand the g-tensor anisotropy of the metal center abolishes the later time part of the modulation making it more difficult to extract distances and their distributions. Nevertheless, reliable distance information can be extracted, provided that a dead-time free method is used.

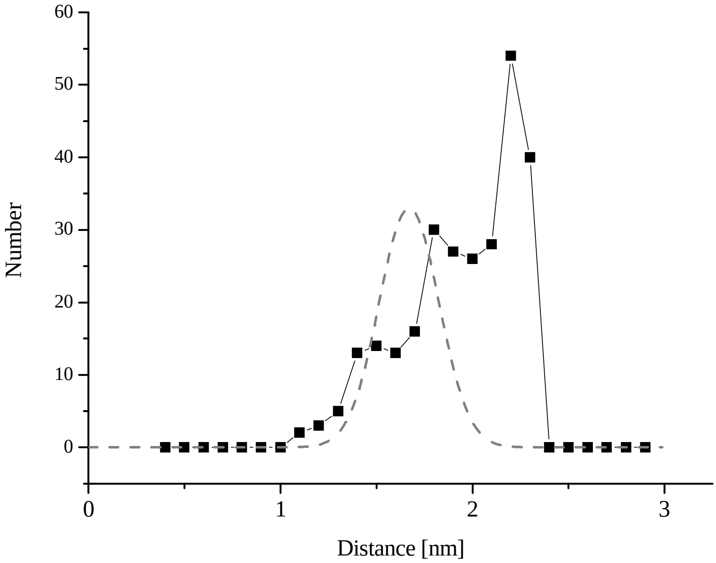

Fig. 6: Distance distribution of Q104C mutant (dashed) superimposed on distance distribution from the model to describe the spin label conformations (see text)

5.4 Conclusion

We demonstrate why for a reliable measurement of distances and distance distributions between transition-metal centers and radicals dead-time free dipolar modulation traces are required. Therefore, the dead-time free version of the RIDME method, as introduced here, will significantly enhance the existing sequence. Limitations of relaxation times and excitation bandwidths define the distance ranges accessible, which, similar to the DEER method should range from 1.5 nm to about 5 nm. Exclusive sensitivity to dipolar interaction makes the method selective to the distances of interest.

Acknowledgments

I would like to thank dr. Sergey Milikisyants who developed the 5-pulse RIDME sequence and the analysis program and Michela Finiguerra for the preparation of the cytochrome *f* samples.

Reference list

1. Schiemann, O.; Prisner, T. F. *Quarterly Reviews of Biophysics* **2007,** *40* (1), 1-53.
2. Borbat, P. P.; Freed, J. H. *Two-Component Signaling Systems, Pt B* **2007,** *423*, 52-62.
3. Jeschke, G.; Polyhach, Y. *Physical Chemistry Chemical Physics* **2007,** *9* (16), 1895-1910.
4. Milov, A. D.; Salikhov, K. M.; Shchirov, M. D. *Sov. Phys. Solid State (Fizika Tverdogo Tela)* **1981,** *23*, 565-569.
5. Saxena, S.; Freed, J. H. *Chemical Physics Letters* **1996,** *251* (1-2), 102-110.
6. Saxena, S.; Freed, J. H. *Journal Of Chemical Physics* **1997,** *107* (5), 1317-1340.
7. Jeschke, G.; Pannier, M.; Godt, A.; Spiess, H. W. *Chemical Physics Letters* **2000,** *331* (2-4), 243-252.
8. Borbat, P. P.; Freed, J. H. *Chemical Physics Letters* **1999,** *313* (1-2), 145-154.
9. Berliner, L. J.; Eaton, S. S.; Eaton, G. R. *Distance Measurements in Biological Systems by EPR;* Kluver Academic/Plenum Publishers: New York, 2000; Vol. 19.
10. Eaton, S. S.; Eaton, G. R. *Structures and Mechanisms: from Ashes to Enzymes* **2002,** *827*, 321-339.
11. Eaton, S. S.; Eaton, G. R. *Coordination Chemistry Reviews* **1988,** *83*, 29-72.
12. Kulik, L. V.; Dzuba, S. A.; Grigoryev, I. A.; Tsvetkov, Y. D. *Chemical Physics Letters* **2001,** *343* (3-4), 315-324.
13. Kulik, L. V.; Grishin, Y. A.; Dzuba, S. A.; Grigoryev, I. A.; Klyatskaya, S. V.; Vasilevsky, S. F.; Tsvetkov, Y. D. *Journal of Magnetic Resonance* **2002,** *157* (1), 61-68.
14. Albarran, C.; Navarro, J. A.; Molina-Heredia, F. P.; Murdoch, P. S.; De la Rosa, M. A.; Hervas, M. *Biochemistry* **2005,** *44* (34), 11601-11607.
15. Abragam, A.; Bleaney, B. I. *Electron paramagnetic resonance of transition ions;* 1970.
16. Pake, G. E. *Journal of Chemical Physics* **1948,** *16* (4), 327-336.
17. Bloom, A. L. *Physical Review* **1955,** *98* (4), 1105-1111.
18. Pannier, M.; Veit, S.; Godt, A.; Jeschke, G.; Spiess, H. W. *Journal of Magnetic Resonance* **2000,** *142* (2), 331-340.

19. Savitsky, A.; Dubinskii, A. A.; Flores, M.; Lubitz, W.; Mobius, K. *Journal of Physical Chemistry B* **2007,** *111* (22), 6245-6262.
20. Jeschke, G.; Koch, A.; Jonas, U.; Godt, A. *Journal Of Magnetic Resonance* **2002,** *155* (1), 72-82.
21. Jeschke, G.; Chechik, V.; Ionita, P.; Godt, A.; Zimmermann, H.; Banham, J.; Timmel, C. R.; Hilger, D.; Jung, H. *Appl. Magn. Reson.* **2006,** *30* (3-4), 473-498.
22. Jeschke, G. *Macromolecular Rapid Communications* **2002,** *23* (4), 227-246.
23. Schunemann, V.; Trautwein, A. X.; Illerhaus, J.; Haehnel, W. *Biochemistry* **1999,** *38* (28), 8981-8991.
24. Zhou, Y.; Bowler, B. E.; Eaton, G. R.; Eaton, S. S. *Journal of Magnetic Resonance* **1999,** *139* (1), 165-174.
25. Du, J. L.; Eaton, G. R.; Eaton, S. S. *Journal of magnetic resonance, Series A* **1994,** *115*, 213-221.
26. Volkov, A. N.; Worrall, J. A. R.; Holtzmann, E.; Ubbink, M. *Proceedings Of The National Academy Of Sciences Of The United States Of America* **2006,** *103* (50), 18945-18950.
27. Finiguerra, M. G.; Prudencio, M.; Ubbink, M.; Huber, M. *Magnetic Resonance In Chemistry* **2008,** in press.

Appendix A

Anti-parallel aggregation of WALP peptides in DOPC

The study of WALP spin labeled at the central position had suggested linear aggregates in DOPC and cluster aggregates in DPPC, both at 120 K (Chapter 4). An anti-parallel arrangement of the peptides within the linear aggregates was proposed from theoretical [1] and experimental studies [2]. In order to investigate whether the line aggregates in DOPC contain the WALP peptides in a parallel or anti-parallel arrangement, a set of cw-EPR experiments was performed on WALP spin labeled at the N- or the C-terminal positions (SL-N-WALP and SL-C-WALP) at 120 K. In the present appendix, we describe a model that can be used to interpret the broadening of the EPR spectra due to anti-parallel aggregates.

Results

In the following, the dipolar interaction was calculated for models of anti-parallel aggregates. For a pair of pure SL-N (or C) WALP in an anti-parallel arrangement (Fig.1a), the dipolar interaction of two electron spins will cause a broadening

$$\left\langle \Delta\Delta B^2 \right\rangle = p\frac{1}{\left(L\right)^6} = p\frac{1}{\left(\sqrt{D^2+R^2}\right)^6} \qquad (1)$$

Here L is the distance between the two spins, and D and R, defined in Fig. 1, are 3 nm and 1 nm respectively.

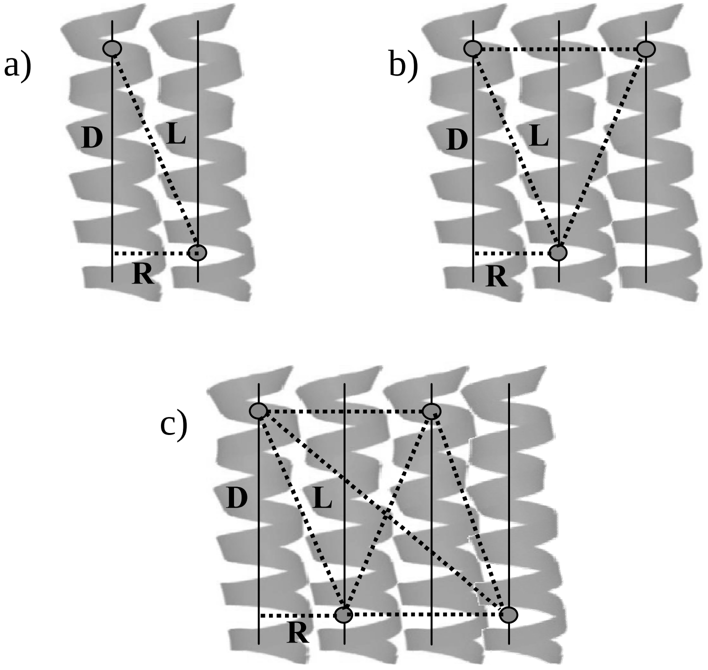

Fig. 1: Schematic representation of line aggregates with anti-parallel arrangements of the trans-membrane helices (WALP). The circle represents the spin label position. a) dimer; b) trimer; c) tetramer.

Assuming that the aggregates are modeled as having a fixed distance R between nearest neighbors, the $<\Delta\Delta B^2>$ value for a trimer and a tetramer anti-parallel aggregate, Fig.1 b and c, is

$$\left\langle \Delta\Delta B^2 \right\rangle_{Trimer} = {}^{p}\!\big/_{3}\left[\frac{2}{\left(2R\right)^6}+\frac{4}{\left(\sqrt{D^2+R^2}\right)^6}\right] \tag{2}$$

$$\left\langle \Delta\Delta B^2 \right\rangle_{Tetramer} = p/4 \left[\frac{4}{(2R)^6} + \frac{6}{\left(\sqrt{D^2+R^2}\right)^6} + \frac{2}{\left(\sqrt{D^2+(3R)^2}\right)^6} \right] \qquad (3)$$

The largest aggregate for which calculations are performed concerns a tetramer because the data analysis in Chapter 4 suggests a tetramer as the most likely aggregate size.

The <$\Delta\Delta B^2$> values for a dimer, a trimer and a tetramer, calculated using this model, are shown in Table 1.

Table 1
Anti-parallel and parallel aggregate model: Calculated broadening of pure SL-N (or C) WALP

Aggregate type	**Calculated Broadening Anti-parallel** <$\Delta\Delta B^2$> (T^2)	**Calculated Broadening Parallel** <$\Delta\Delta B^2$> (T^2)
Dimer	$1.56*10^{-9}$	$1.56*10^{-6}$
Trimer	$1.83*10^{-8}$	$2.09*10^{-6}$
Tetramer	$2.68*10^{-8}$	$2.36*10^{-6}$

For a mixed sample (50% SL-N-WALP and 50% SL-C-WALP) the previous model has to be modified. For an anti-parallel arrangement of the peptides the chances that the spins will be at a distance R to each other (SL-C and SL-N WALP as the closest neighbor, Fig. 2a) or at a distance L (SL-N and SL-N WALP (or SL-C and SL-C) as closest neighbor, Fig. 2b) are equal. Therefore, a model that takes into account all the possible combinations and the weight that each of them has on the broadening, has been made.

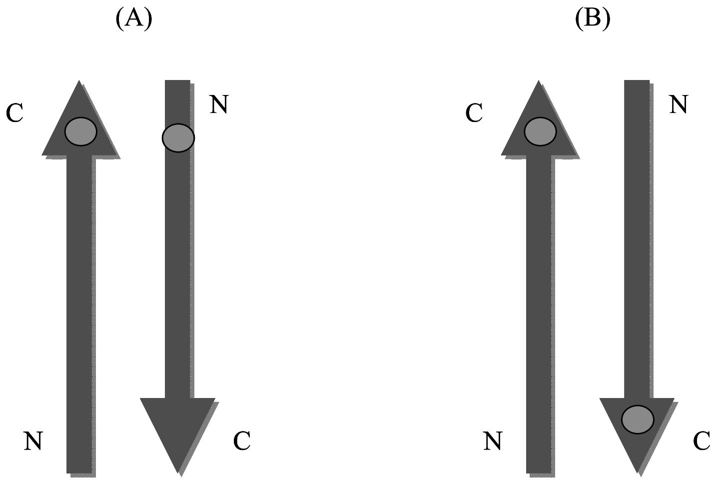

Fig. 2: Schematic representation of an anti-parallel dimer for mixed sample (50% SL-N-WALP and 50% SL-C-WALP). The circle represents the spin label position.(A) SL-C and SL-N as closest neighbor; (B) SL-C and SL-C as closest neighbour.

The calculated <$\Delta\Delta B^2$> for the mixed SL-N and SL-C WALP are shown in Table 2.

Table 2

Calculated broadening of mixed SL-N and SL-C WALP, anti-parallel arrangement

Aggregate type	**Calculated Broadening** <$\Delta\Delta B^2$> (T^2)
Dimer	$7.08*10^{-7}$
Trimer	$1.05*10^{-6}$
Tetramer	$1.19*10^{-6}$

Discussion

The distance among spins for the pure SL-N (or C) WALP in the anti-parallel aggregate is bigger than the one in the parallel arrangement and this results in a smaller dipolar broadening, see Table 1.
The small calculated $<\Delta\Delta B^2>$ for the anti-parallel arrangement is in agreement with the experimental data (see result Chapter 4). Indeed the comparison of the pure SL-N and SL-C-WALP spectra with the diamagnetically diluted ones has shown such a small broadening value, $<\Delta\Delta B^2>$, that it can not be discriminated within the experimental uncertainty. If the aggregates were composed of WALP in a parallel arrangement we would have had a bigger $<\Delta\Delta B^2>$ value from the broadening of the spectra. This suggests that the arrangement of the peptides is most likely anti-parallel or random, and, from the result obtained by E. Sparr and coworkers we conclude that anti-parallel arrangement is the most probable [2,3] .
To measure the broadening due to dipolar interaction for spins separated by a certain distance L (anti-parallel arrangement), the WALP has to be spin labeled positions other than the C- or N- terminus. For a pure SL-N (or C-) WALP, for which the spin labels are at a position that makes D = 0.6 nm the calculated broadening has a detectable value. In this case for a tetramer aggregate $<\Delta\Delta B^2>$ will be $1.0*10^{-6}$ T^2, and this dipolar broadening can be easily detected by EPR, see Fig. 6 in Chapter 4.

Reference List

1. Yano, Y.; Matsuzaki, K. *Biochemistry* **2006,** *45*, 3370-3378.
2. Sparr, E.; Ash, W. L.; Nazarov, P. V.; Rijkers, D. T. S.; Hemminga, M. A.; Tieleman, D. P.; Killian, J. A. *Journal of Biological Chemistry* **2005,** *280* (47), 39324-39331.
3. Sparr, E.; Ganchev, D. N.; Snel, M. M. E.; Ridder, A. N. J. A.; Kroon-Batenburg, L. M. J.; Chupin, V.; Rijkers, D. T. S.; Killian, J. A.; de Kruijff, B. *Biochemistry* **2005,** *44* (1), 2-10.

Appendix B

The longitudinal relaxation time (T_1) of Fe(III) in cytochrome *f*: power saturation

The applicability of the RIDME sequence (Chapter 5) depends on the longitudinal relaxation of the B spins. Here we show how the longitudinal relaxation time (T_1) of the Fe(III) center in the spin labeled cytochrome *f* protein mutant Q104C may be determined by the microwave power saturation method. In this method T_1 is measured from the effect of the microwave power on the intensity of the EPR line. For low microwave power, the rate of the induced transitions is small and the line intensity is proportional to that rate, which is given by the square root of the microwave power. For higher microwave powers such that the induced rate becomes comparable to the rate of T_1 relaxation, the line intensity increases less strongly than at low powers. At even higher microwave powers the line intensity becomes constant or even decreases.

The dependence of the line intensity on the power depends on whether the EPR signal is homogeneously or inhomogeneously broadened. The EPR signal of the Fe(III) center is inhomogeneously broadened, which means that we observe an envelop that consists of a distribution of individual resonant lines (Fig. 1). The shape of the envelop is Gaussian, while the individual lines have a Lorentzian line shape. The width of the whole Gaussian envelop is given by $\Delta\omega_G$. The width of the individual Lorentzian lines is given by [1]

$$\Delta\omega_L = \frac{1}{T_2} \quad , \tag{1}$$

where T_2 is the transversal relaxation time.

The procedure to obtain T_1 from the power dependence is described below.

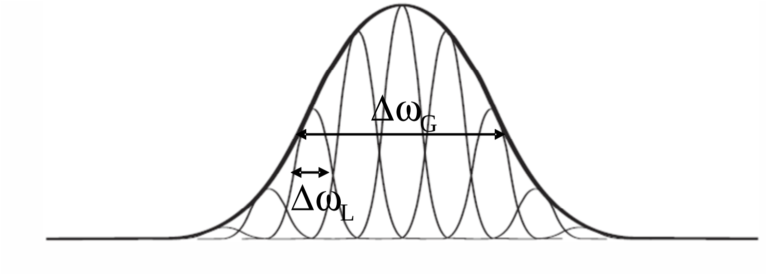

Fig. 1: Superposition of Lorentzian lines (thin lines) constituting an inhomogeneously broadened Gaussian line (thick line). The width of the envelop is indicated by the Gaussian width $\Delta\omega_G$. The width of the individual lines, which constitute the envelop, is indicated by the Lorentzian width $\Delta\omega_L$.

Experimental methods

The X-band cw EPR measurements have been performed using an ELEXSYS E 680 spectrometer (Bruker, Rheinstetten, GE) equipped with a helium gas-flow cryostat and a rectangular cavity. The EPR spectra were recorded at 7 K using a modulation amplitude of 1.5 mT. The intensity of the low-field EPR line was measured at different power levels in a range from 0.052 mW to 200 mW. The EPR spectra were baseline corrected using Xepr software (Bruker Biospin, Rheinstetten, Germany). Because of the baseline correction, the estimation of T_1 has an error of 20%. The fit was done using MatLab (MathWorks, MA, USA).

The amplitude of the microwave magnetic field (H_1) and the incident microwave power (P) are related by [1,2]

$$H_1 = g^I \sqrt{QP} \quad , \tag{2}$$

where g^I depends on the geometry of the cavity, Q is the quality factor of the cavity. For the rectangular cavity used in our measurements g^I = $0.0028\ mT/\sqrt{mW}$ [3] and Q = 4000.

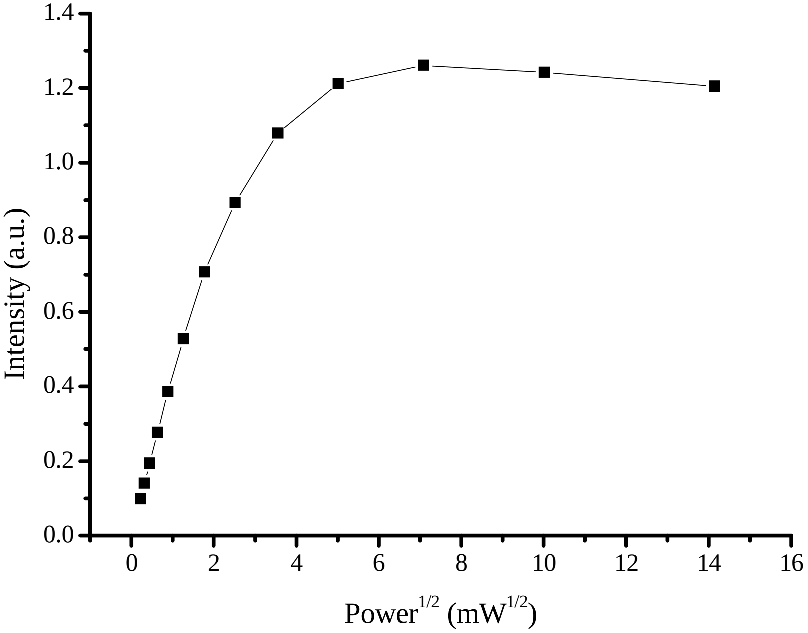

Fig. 2: The intensity of the low field EPR signal of Fe(III) as a function of the square root of the microwave power.

Results

In Fig. 2 a plot of the intensity of the low-field component of the EPR signal of the Fe(III) (Fig. 3) as a function of the square root of the microwave power is shown. The intensity of the EPR line became almost constant for high values of the microwave power [4] , between 50 mW and 200 mW, and the shape of the line can be fitted by a Gaussian function (Fig. 3b). These observations confirm the inhomogeneous broadening of the Fe(III) signal.

The longitudinal relaxation rate is related to the *saturation factor* [3] Z. The Z value is given by

$$Z = \frac{1}{1 + H_1^2 \gamma^2 T_1 T_2} \quad , \tag{3}$$

where γ is the magnetogyric ratio ($\gamma = 2.8 * 10^{10}\ s^{-1}\ T^{-1}$).
From the power P the value of H_1 can be calculated according to Eq. 2.

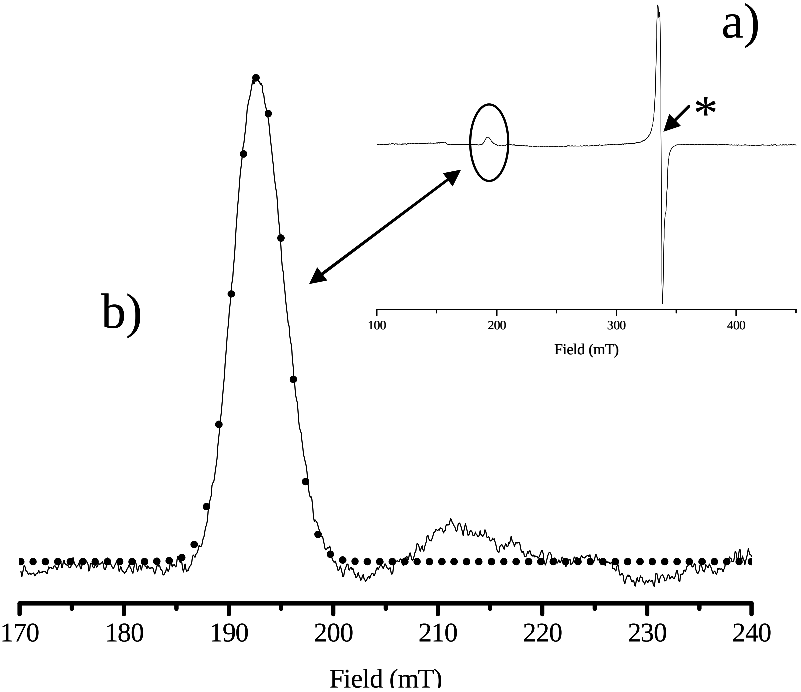

Fig. 3: a) The EPR spectrum of the spin-labeled cytochrome f mutant Q104C, recorded with a microwave power of 3.14 mW. The intense signal indicated by the asterisk is due to the nitroxide spin label. b) The low field line of the EPR signal shown in a), and the fit of this line to a Gaussian (black dots). The EPR spectrum has been baseline corrected.

For $H_1 = H_{1/2}$, corresponding to a value of $P = P_{1/2}$ such that the saturation factor Z becomes 0.5, we obtain

$$H_{1/2}^2 \gamma^2 T_1 T_2 = 1 \quad , \tag{4}$$

and consequently

$$T_1 = \frac{1}{H_{1/2}^2 \gamma^2 T_2} \quad . \tag{5}$$

To obtain $H_{1/2}$ we need $P_{1/2}$. Knowing $H_{1/2}$, only T_2 is needed to obtain T_1 from Eq. 5.
The $P_{1/2}$ value can be obtained by fitting the normalized intensity Y_n of the EPR signal with the following equation [3]

$$Y_n = \frac{Y / \sqrt{P}}{Y_0 / \sqrt{P_0}} = \frac{1}{\left[1 + \left(P / P_{1/2}\right)\right]^{b/2}} , \tag{6}$$

where Y_n is the normalized line intensity, Y is the line intensity obtained at the power P, and Y_0 is the line intensity obtained at a power P_0 of 0.399 mW, under nonsaturating conditions. Fitting this equation to the data points results in the plot shown in Fig. 4. The fit yields the parameters $P_{1/2}$ and b, where b is called the inhomogeneity parameter [3], which can be expressed as

$$\log b = \frac{\Delta\omega_L}{\Delta\omega_G} \tag{7}$$

where $\Delta\omega_G$ is measured from the experimental spectrum. In our case, the low-field EPR line has a $\Delta\omega_G$ of 6 mT. From the fit we have obtained the parameters: b = 1.048 and $P_{1/2}$ = 9 mW. As mentioned previously, $\Delta\omega_L$ is related to T_2. Therefore, knowing b and $\Delta\omega_G$, the $\Delta\omega_L$ value has been calculated from Eq. 7, which results in T_2 = 45 ns. Having calculated $H_{1/2}$ and knowing T_2, a value of 102 μs is obtained for T_1.

In Chapter 5, from the modulation depth of the RIDME trace, we have detected two components of T_1 (148 μs and 13 μs) and attributed this to the anisotropy of this relaxation time. In the present study, we were able to determine T_1 from the effect of the microwave power on the signal corresponding to one of the canonic orientations of the Fe(III) center. To measure the full extend of the anisotropy, a larger number of orientations would have to be measured. Given the spread of the EPR signal of Fe(III) over 300 mT, at many of these spectral positions the signal intensity is probably too small to do so. This precluded us to detect any orientation dependence of T_1. The T_1 value of 102 μs is closer to the larger T_1 component obtained from the RIDME traces.

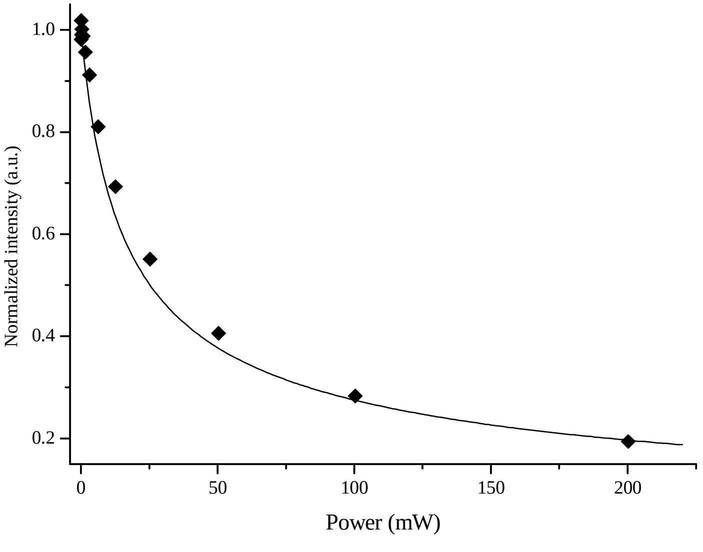

Fig. 4: The plot of the normalized line intensity Y_n (see text) of the low-field EPR signal of Fe(III) as a function of the microwave power. The black diamonds represent the data points. The black curve is the fit.

Reference List

1. Castner, T. G. *Physical Review* **1959,** *115* (6), 1506-1515.
2. Poole, C. P. J. *Electron Spin Resonance: A Comprehensive Treatise on Experimental Techniques;* Dover Publications: Mineola, New York, 1996.
3. Sahlin, M.; Graslund, A.; Ehrenberg, A. *Journal of Magnetic Resonance* **1986,** *67* (1), 135-137.
4. Portis, A. M. *Physical Review* **1953,** *91* (5), 1071-1078.

Summary

Proteins and enzymes play a key role in all biological systems. Understanding the mechanism of biological functions and reactions in which proteins and enzymes are involved requires a detailed characterization of protein structure and dynamics. Structure refers to geometrical structure, as a result of the local arrangement of amino-acid side chains, and electronic structure, in particular at the active site of proteins and enzymes. Dynamics refers to structural changes that proteins undergo to perform their function.

The work reported in this thesis concerns both methodological developments and the application of electron paramagnetic resonance (EPR) to study protein structure and dynamics. To this end, both continuous wave (cw) and pulsed microwave excitation have been applied. In the research described in this thesis transition-metal ions, such as Cu(II) and Fe(III), and nitroxide spin labels have been used as paramagnetic probes.

In Chapter 2, high frequency (95 GHz) EPR on the M150E mutant of the nitrite reductase (NiR) protein is reported. The wild type of NiR is a homotrimer in which each monomer contains a type-1 (blue) copper site and a type-2 (non blue) copper site. The NiR protein catalyses the reduction of nitrite to nitric oxide. In the catalytic cycle of the protein, the type-2 site, in which the copper is ligated to three histidines (His100, His135, and His306) and a water molecule, binds nitrite at the expense of water. Subsequently, the nitrite is reduced to nitric oxide by an electron transferred from the type-1 copper site.

Type-1 copper sites have been extensively studied, while less is known about the electronic structure of type-2 copper sites. In this study we investigated the mutant M150E of the NiR protein, for which the type-1 copper site is EPR silent. A single crystal was investigated and the complete g-tensor of the type-2 copper site was determined. The g-tensor was interpreted in terms of the copper orbitals that take part in the wavefunction of the unpaired electron.

Analysis of the single-crystal EPR data results in three possible orientations of the g-tensor with respect to the copper site. On the basis of an analysis of the copper coordination and of the copper d-orbitals

that are involved in the unpaired-electron wavefunction, the most plausible orientation of the g-tensor was chosen. The orientation of the g-tensor suggests that the unpaired electron is in a molecular orbital that contains a copper d_{xy} type orbital in σ-antibonding overlap with the lone-pair orbitals of the nitrogens of His135 and His306.

To interpret the rhombicity and the orientation of the g-tensor with respect to the site further, we used a model that describes how the spin-orbit contribution of the copper atom relates to the g-tensor by considering which d-orbitals are involved in the molecular orbital (MO) containing the unpaired electron. This model indicates that the rhombicity of the site is most probably due to the spin-orbit coupling from the oxygen of the water molecule.

In Chapter 3, an EPR study of ten spin-labeled surface sites of the cytochrome c peroxidase (CcP) protein is reported. The cw EPR was performed on the liquid solution of this protein to study the mobility of the spin labels.

In this study we compare the direct measure of the mobility obtained from the simulation of the EPR spectra, the rotation-correlation time (τ_c), with the mobility data obtained from the line-shape analysis proposed by the Hubbell group, the Hubbell plot. Furthermore, to investigate how well methods using the X-ray structure of a protein can predict mobile, exposed surface sites, we compare the mobility results to the prediction of solvent accessibility and conformational freedom.

The τ_c values provide a sound ranking of the mobility of surface residues. For surface sites, the mobility plot, obtained from the Hubbell model does not add much to the τ_c analysis. This derives from the small mobility differences and the errors in the parameters. The mobility plot is better suited to differentiate between spin labels that span the entire range from buried to surface residues and therefore have a larger spread of mobility parameters. Fractional solvent accessibility data are well suited to identify residues that are sufficiently exposed for surface labeling. They are less well suited to predict the ranking of mobility, owing to the absence of structural parameters defining the conformations of the linker between the cysteine and the spin label. The ranking obtained from a model that predicts the conformational freedom of the spin labels follows closely the trend in τ_c values obtained from the simulation, suggesting that this model reflects the essence of the mobility of the spin labels.

Chapter 4 concerns a cw EPR investigation of spin-labeled WALP peptides in membranes (lipid bilayers). The WALP is a peptide that forms a transmembrane α-helix and serves as a model to study the elementary aspects of protein-membrane interactions. One of the intriguing and biologically relevant responses of peptides to different membrane conditions is aggregation.
We have investigated spin-labeled WALP in different lipid systems, i.e., unsaturated lipid (DOPC) and saturated lipid (DPPC), over a wide range of temperatures, which has allowed us to study the effect of both gel and liquid-crystalline phases of the lipids on the aggregation of WALP.
Spin-label EPR has been used in different ways to investigate membrane-peptide systems, but the present approach is novel in that the peptide-peptide interaction is directly probed by spin-labeling the peptide and detecting aggregation by the spin-spin interaction of the labels. We developed a model that can qualitatively discriminate between different arrangements of peptides in the aggregate. We find that the higher degree of order of the lipid chains in the gel phase seems to be a major factor in promoting aggregation. We conclude this because both the saturated lipid DPPC and the unsaturated lipid DOPC promote WALP aggregation in the gel phase. However, the degree of saturation of the lipids seems to affect the type of aggregate and our analysis suggests cluster aggregates in DPPC and line aggregates in DOPC.

In Chapter 5 we describe a new *relaxation induced dipolar modulation* (RIDME) pulse sequence.
In the last decade several pulsed EPR methods have been developed and used to measure distances and to determine the structure of chemical and biological systems from the dipolar interaction between electron spins. These techniques require that the pulses excite a large part of the spectrum of the paramagnetic species. Due to instrumental factors, the excitation bandwidth of pulses is limited, which makes the investigations of systems with large spectral anisotropy difficult. Because of this limitation, the pulsed techniques are used predominantly to measure distances between nitroxide spin labels and organic radicals, which have low spectral anisotropy. To measure the distance between a nitroxide

spin label and a transition-metal ion that has a large spectral anisotropy, other methods are needed. One such method is the RIDME technique. This sequence makes use of spontaneous spin flips of the transition-metal ion. Thereby, it avoids the need for a pump pulse with a large excitation bandwidth to induce the spin flip of the transition-metal ion. The usefulness of the RIDME technique was limited because of a dead-time problem. For systems with large spectral anisotropy, most of the information about the dipolar interaction lays in the initial part of the dipolar-modulation time trace, and this initial part is lost in the dead-time.

In our research we developed a new 5-pulse RIDME sequence, which completely eliminates the dead time. We apply the new sequence in cytochrome *f* to measure the distance between the low-spin iron(III) center, a paramagnetic center with large spectral anisotropy, and a nitroxide spin label. The distance we found agrees well with the one obtained from crystallography. Presently, there is no other method to determine distances in such cases with similar accuracy.

Samenvatting

Eiwitten en enzymen spelen een sleutelrol in alle biologische systemen. Het begrijpen van het mechanisme achter de biologische functies en reacties waarbij eiwitten en enzymen een rol spelen vereist een gedetailleerde karakterisering van de eiwitstructuur en -dynamica. Het begrip eiwitstructuur verwijst hier naar de geometrische structuur, die wordt bepaald door de lokale ordening van de aminozuren, en naar de electronische structuur, in het bijzonder die van het actieve centrum van eiwitten en enzymen. Dynamica verwijst naar de structuurveranderingen die het eiwit ondergaat als het zijn functie vervult.

Het werk beschreven in dit proefschrift betreft de ontwikkeling van elektron-paramagnetische-resonantie (EPR) methoden en de toepassing daarvan op de studie van eiwitstructuur en -dynamica. Daartoe zijn zowel experimenten met continue microgolfexcitatie (cw) als experimenten met gepulste microgolfexcitatie uitgevoerd. In het onderzoek zijn overgangsmetaalionen, zoals Cu(II) en Fe(III), en nitroxide spin-labels gebruikt als paramagnetische sensoren.

In hoofdstuk 2 wordt een hoogfrequent (95 GHz) EPR experiment aan de M150E mutant van het eiwit nitrietreductase (NiR) beschreven. Het wild type van NiR is een homotrimeer waarvan elk monomeer een type-1 (blauw) kopercentrum en een type-2 (niet-blauw) kopercentrum bevat. Het NiR eiwit katalyseert de reductie van nitriet naar stikstofmonoxide. In de katalytische cyclus van het eiwit bindt het type-2 kopercentrum, waarin het koper is gebonden aan drie histidines (His100, His135 en His306) en een watermolecuul, het nitriet ten koste van water. Vervolgens wordt het nitriet gereduceerd tot stikstofmonoxide doordat een elektron wordt overgeheveld vanuit het type-1 kopercentrum.

Type-1 kopercentra zijn uitgebreid bestudeerd. Minder is bekend over de electronische structuur van type-2 kopercentra. In deze studie hebben we de mutant M150E van het NiR eiwit onderzocht, waarvan het type-1 kopercentrum geen EPR signaal geeft. Een eenkristal is onderzocht en de volledige g-tensor is bepaald. De g-tensor kon worden geïnterpreteerd in termen van de koperorbitalen die deel uitmaken van de golffunctie van het ongepaarde elektron.

Analyse van de EPR data afkomstig van het eenkristal leverde drie mogelijke oriëntaties op van de g-tensor ten opzichte van het kopercentrum. Op basis van een analyse van de coördinatie van het koper en van de koper d-orbitalen die deel uitmaken van de golffunctie van het ongepaarde elektron kon de meest waarschijnlijke oriëntatie van de g-tensor worden gekozen. Deze oriëntatie suggereert dat het ongepaarde elektron in een moleculaire orbitaal is die een koper d_{xy}-orbitaal bevat in σ-antibindende overlap met de orbitalen van de vrije elektronenparen van de stikstofatomen van His135 en His306.
Om de rhombiciteit van de g-tensor en de oriëntatie ten opzichte van het kopercentrum beter te kunnen begrijpen hebben we een model gebruikt dat beschrijft hoe de spin-baankoppeling van het koperatoom de g-tensor bepaalt door te kijken welke d-orbitalen deel uitmaken van de moleculaire orbitaal die het ongepaarde elektron bevat. Dit model geeft aan dat de rhombiciteit zeer waarschijnlijk een gevolg is van de spin-baankoppeling op het zuurstofatoom van het watermolecuul.

In hoofdstuk 3 wordt een EPR studie van tien spin-gelabelde oppervlakteplaatsen van het eiwit cytochrome c peroxidaxe (CcP) beschreven. Om de mobiliteit van de spin-labels te kunnen bestuderen is de cw EPR studie uitgevoerd aan een vloeibare oplossing van dit eiwit.
In deze studie vergelijken we de rotatie-correlatietijd, τ_c, welke een directe maat is voor de mobiliteit verkregen uit de simulatie van EPR spectra, met de data over de mobiliteit verkregen uit de door de Hubbell onderzoeksgroep voorgestelde analyse van de vorm van het spectrum, de zogenaamde Hubbell-plot. Verder hebben we onderzocht hoe goed methoden die gebruik maken van de kristalstructuur van een eiwit mobiele, toegankelijke oppervlakteplaatsen kunnen voorspellen. Hiertoe vergelijken we de mobiliteit met voorspellingen van de toegankelijkheid voor het oplosmiddel en een model voor de conformatievrijheid van het spin-label.
De τ_c waarden geven een betrouwbare volgorde voor de mobiliteit van oppervlakteresiduen. Voor oppervlakteplaatsen voegt de mobiliteitsplot verkregen uit het Hubbell-model niet erg veel toe aan de analyse van τ_c. Dit is een gevolg van de kleine mobiliteitsverschillen en de fouten in de parameters. De mobiliteitsplot is meer geschikt om onderscheid te kunnen maken tussen spin-labels, die in het ene uiterste geval volledig

ingebed liggen en in het andere uiterste geval oppervlakteresiduen zijn, en daarom een veel grotere spreiding hebben in hun mobiliteitsparameters. Data over de fractionele toegankelijkheid voor het oplosmiddel zijn zeer geschikt om residuen te identificeren die voldoende bereikbaar zijn voor oppervlakte labeling. Ze zijn minder geschikt om de mobiliteit te voorspellen, als gevolg van de afwezigheid van structuurparameters die de conformatie van de binding tussen het cysteïne en het spin-label bepalen. De mobiliteit verkregen uit een model dat de conformatievrijheid van het spin-label voorspelt volgt de trend in τ_c-waarden verkregen uit de simulatie, hetgeen suggereert dat dit model de essentie van de mobiliteit van spin-labels weergeeft.

Hoofdstuk 4 gaat over een cw EPR studie van spin-gelabelde WALP peptiden in membranen (lipide dubbellagen). Het WALP peptide vormt een transmembrane α-helix, en kan dienen als model om elementaire aspecten van eiwit-membraaninteracties te bestuderen. Een van de intrigerende en biologisch relevante reacties van peptiden op verschillende membraancondities is aggregatie.

We hebben spin-gelabeld WALP onderzocht in verschillende lipidesystemen, dat wil zeggen onverzadigde lipiden (DOPC) en verzadigde lipiden (DPPC), en bij verschillende temperaturen. Dit bood ons de mogelijkheid om het effect van zowel een gelfase als een vloeibaar-kristallijne fase van de lipiden op de aggregatie van het WALP te bestuderen.

Spin-label EPR is op verschillende manieren gebruikt om membraan-peptide systemen te onderzoeken. De hier beschreven aanpak is nieuw in de zin dat de peptide-peptideinteractie direct kan worden onderzocht door het peptide te voorzien van een spin-label waardoor met behulp van de spin–spin interactie de aggregatie kan worden waargenomen. We hebben een model ontwikkeld dat kwalitatief onderscheid kan maken tussen verschillende conformaties van de peptiden in het aggregaat. We vinden dat de hogere graad van ordening van de lipideketens in de gelfase een belangrijke factor ter promotie van aggregatie lijkt te zijn. We concluderen dit omdat de verzadigde lipide DPPC en de onverzadigde lipide DOPC beide de aggregatie van WALP in de gelfase bevorderen. Echter, de verzadigingsgraad van de lipiden lijkt van invloed te zijn op het type aggregaat dat gevormd wordt en onze analyse suggereert clusteraggregatie in DPPC en lijnaggregatie in DOPC.

In hoofdstuk 5 beschrijven we een nieuwe “relaxation induced dipolar modulation” ofwel “RIDME” pulssequentie.

In de laatste tien jaar zijn verschillende gepulste EPR methoden ontwikkeld en gebruikt om afstanden te meten en de structuur van chemische en biologische systemen te bepalen uit de dipolaire interactie tussen elektronspins. Deze technieken vereisen dat de pulsen een groot gedeelte van het spectrum van het paramagnetische molecuul exciteren. Door instrumentele beperkingen is de excitatiebandbreedte van pulsen beperkt en dit maakt het onderzoeken van systemen met grote spectrale anisotropie moeilijk. Vanwege deze beperking worden gepulste technieken voornamelijk gebruikt om afstanden te meten tussen radicalen die een kleine spectrale anisotropie hebben, zoals nitroxide spin-labels en organische radicalen. Om de afstand tussen een nitroxide spin-label en een overgangsmetaalion dat een grote spectrale anisotropie heeft te kunnen meten zijn andere methoden nodig. Een dergelijke methode is de RIDME-techniek. Deze pulssequentie maakt gebruik van spontane spin flips van het overgangsmetaalion. Er is daarom geen pomppuls met een grote excitatiebandbreedte nodig om de spin flip van het overgangsmetaalion te bewerkstelligen. De bruikbaarheid van de RIDME techniek was beperkt vanwege het probleem met de dode tijd. Voor systemen met een grote spectrale anisotropie bevindt de meeste informatie over de dipolaire interactie zich in het eerste stuk van de dipolaire modulatiecurve en dit eerste stuk gaat verloren in de dode tijd.

In ons onderzoek hebben we een nieuwe vijf-puls RIDME sequentie ontwikkeld, waarbij geen dode tijd optreedt. We passen deze nieuwe pulssequentie toe op cytochrome f om de afstand te bepalen tussen het laag-spin Fe(III) centrum, een paramagnetisch centrum met een grote spectrale anisotropie, en een nitroxide spin-label. De met behulp van deze nieuwe techniek gevonden afstand komt goed overeen met de afstand verkregen uit Röntgen-diffractie. Op dit moment is er geen andere methode die dergelijke afstanden zo nauwkeurig kan bepalen.

List of Publications

Scarpelli F., Guzzi R., Bartucci R., Sportelli L. – ***Pulsed EPR Study of Spin Labeled Hemoglobin*** – to be submitted.

Scarpelli F., Drescher M., Meijneke T., Holt A., Rijkers D., Killian J.A., Huber M. – ***Aggregation of Transmembrane Peptides Studied by Spin-Label EPR*** – Journal of Physical Chemistry B, submitted.

Milikisyants S., Scarpelli F., Finiguerra M., Ubbink M., Huber M.,– ***A pulsed EPR method to determine distances between paramagnetic centers with strong spectral anisotropy and radicals: The dead-time free RIDME sequence*** – Journal of Magnetic Resonance, submitted

Scarpelli F., Gast P., Milikisyants S., Murphy M.E.P., Arrieta A.L., Groenen E.J.J., Huber M. – ***A 95 GHz single crystal EPR study of the type 2 copper site of the M150E mutant of the nitrite reductase of Alcaligenes faecalis*** – in preparation

Scarpelli F., Volkov A., Bashir Q., Ubbink M., Huber M., – ***Dynamics of spin labels at surface sites of cytochrome c peroxidase by EPR***– in preparation

Curriculum Vitae

of Francesco Scarpelli, born in Cosenza (Italy), on April 3, 1976.

In 1996, after I received the diploma from Liceo Scientifico G. B. Scorza in Cosenza, I joined the Department of Physics at the Università degli studi della Calabria. I spent the last two and a half years of my studies working on my graduation thesis in the group of Prof. L. Sportelli at the Department of Molecular Biophysics. My thesis project concerned the study of a spin-labeled hemoglobin by pulsed EPR. In July 2004, I graduated in Physics, with a specialization in Molecular Biophysics, at the Università degli studi della Calabria.

In March 2005, I started a PhD project at the Department of Molecular Physics of Leiden University, under the supervision of dr. M. Huber and prof. dr. E.J.J. Groenen. In this research project, I was involved in methodological developments and the application of EPR in the study of dynamics and structure of systems that involve transition metal ions and nitroxide spin labels. During my PhD I assisted in the physics courses for 1st and 3rd year biology students. In July 2005, I attended the "Advanced EPR methods in Biophysics" school in Wiesbaden (Germany). In March 2006, I followed the "EasySpin, spectral simulation and data analysis in EPR spectroscopy" school at the ETH in Zurich. I have presented the results of my research at the 16th Benelux EPR society meeting (May 2008, Gent) and the "Advanced Paramagnetic Resonance in Molecular Biophysics" meeting (September 2008, Siena).

Nawoord

The last four years have been a great experience on both professional and personal level. During my PhD I had the opportunity to meet a lot of interesting people without whom this thesis would not be written now.

First of all I would like to thank dr. Sergey Milikisyants, he has been a guide during this “journey” and also a good friend. Almost all I know about EPR is thank to him.

I am also grateful to dr. Martina Huber for the patience and the precious help in the realization of this thesis and dr. prof. Edgar Groenen for the useful and interesting discussions and suggestions.

A special thanks to Peter Gast, for his help and patience during long and frustrating measurements and Malte Drescher for the useful discussions and collaboration in one of my project.

Thank to Alex Volkov and Qamar Bashir for the spin labelled cytocrhome and Marcellus Hubbink for the useful help.

I owe Michael Murphy and Angela Arrieta my gratitude for the NiR proteins and crystals.

A big thank to the whole MoNOS group, I can not image a better and more friendly environment where I could do my PhD. A particular thanks to Jennifer Mathies for the help in the final step of the thesis and the funny discussions and Michael Galouzis, the best office mate I could have; I have had a very nice time with him and shared a lot of common interests.

A very special thanks to Anna Pezzarossa for the fantastic time we spent, for the always interesting discussions and for being there always when I needed help and support.

I want to mention also some important people that have been and always will be part of my life, my appreciation goes to Francesco, Carmine, Emilio and Loredana.